ADVANCED MODULATION AND DETECTION TECHNIQUES FOR INDOOR VISIBLE LIGHT COMMUNICATION SYSTEMS

CHEN CHEN

School of Electrical and Electronic Engineering

A thesis submitted to the Nanyang Technological University

in partial fulfillment of the requirement for the degree of

Doctor of Philosophy

2017

Acknowledgments

First of all, I would like to take this opportunity to express my deep and sincere gratitude to my supervisor, Professor ZHONG Wen-De from Nanyang Technological University, for his guidance and continuous support during my PhD study. In particular, his academic excellence and enthusiasm for research have lighted me the way for pursuing the research areas I am interested in. I also want to thank him for his patience and tireless advice which have been essential for the completion of my PhD thesis.

I would also like to thank the staff and students in Nanyang Technological University, who have greatly helped me in both my study and life, including Dr. Wu Dehao, Dr. Liu Zhansheng, Dr. Du Pengfei, Dr. Xiong Fei, Dr. Li Xiang, Dr. Zhao Lifan, Dr. Zhang Ting, Dr. Gu Jun, Dr. Ding Sun, Mr. Zhang Sheng, Ms. Zhang Ran, Mr. Yang Helin, Mr. Wang Yuan, Mr. Hu Wenchao, Ms. Cui Dongyao, Ms. Luo Yuemei, Dr. Chen Zhenghua, Ms. Zhang Jing, Ms. Zhang Nan and many other dear friends. Without their presence, I could not have such a wonderful time in Singapore.

Last but not least, I am grateful to all my family members in China for their unconditional love, upbringing encouragement and constant confidence. Most importantly, I would like to show my endless love and thanks to my dearest wife Ms. Qian Min, who has always been there for me and every setback turns from a stone to a piece of feather owing to her wholeheartedly encouragement and support.

~ This thesis is dedicated to my beloved wife ~

Table of Contents

Acknowledgments....................i
Table of Contents....................iii
Abstract....................vii
List of Abbreviations....................ix
List of Figures....................xi
List of Tables....................xv
Chapter 1 Introduction....................1
  1.1 Background and motivations....................1
    1.1.1 Background....................1
    1.1.2 Motivations....................5
  1.2 Major contributions....................6
  1.3 Thesis organization....................8
Chapter 2 Literature Review....................10
  2.1 Introduction of VLC....................10
    2.1.1 System model....................10
    2.1.2 Modulation techniques....................14
    2.1.3 Detection techniques....................17
  2.2 MIMO-VLC....................18
    2.2.1 Transmission schemes....................18
    2.2.2 MIMO receivers....................19
  2.3 Applications of VLC....................20
  2.4 Summary....................24
Chapter 3 Non-Hermitian Symmetry OFDM for MIMO-VLC....................25
  3.1 Introduction....................25
  3.2 Principle of NHS-OFDM based MIMO-VLC....................26
  3.3 BER analysis....................29

3.3.1 BER of MIMO-VLC using HS-OFDM 29

3.3.2 BER of MIMO-VLC using NHS-OFDM 31

3.4 Performance evaluation 32

3.4.1 BER performance 32

3.4.2 Transceiver complexity 36

3.4.3 Experimental demonstration 37

3.5 Impact of LED pairing 41

3.5.1 NHS-OFDM with LED pairing 41

3.5.2 BER analysis 42

3.5.3 Comparison of different LED pairing schemes 45

3.6 Conclusion 53

Chapter 4 Imaging Receiver Using Angle Diversity Detectors for MIMO-VLC 54

4.1 Introduction 54

4.2 Principle of ImADR 55

4.3 Performance comparison between ImR and ImADR 57

4.3.1 Field of view 57

4.3.2 Area of detector array 58

4.3.3 Optical channel gain 59

4.4 BER performance 61

4.4.1 BER analysis 61

4.4.2 System setup and results 62

4.5 Conclusion 65

Chapter 5 Angle Diversity Multi-Element Receiver for ICI Mitigation in Multi-Cell VLC 66

5.1 Introduction 66

5.2 Principle of ADMER 67

5.3 Experimental demonstration of a two-cell VLC system 69

5.3.1 Experimental setup 69

5.3.2 Experimental results ... 71
5.4 Numerical analysis of a four-cell VLC system ... 74
5.4.1 System setup ... 74
5.4.2 Results and discussions ... 78
5.5 Conclusion ... 85
Chapter 6 Integration of VLC and OFDM-PON Based on Adaptive Envelope Modulation ... 87
6.1 Introduction ... 87
6.2 System integration ... 88
6.2.1 System architecture ... 88
6.2.2 Constant envelope OFDM ... 90
6.2.3 Adaptive envelope modulation ... 91
6.3 Performance analysis of wired access ... 93
6.3.1 BER of CE-OFDM signal with *M*-PAM overlay ... 94
6.3.2 BER of overlaid *M*-PAM signal without VLC wireless transmission ... 97
6.3.3 Performance trade-off ... 99
6.4 Performance analysis of VLC wireless access ... 101
6.5 Conclusion ... 103
Chapter 7 Conclusions and Future Work ... 104
7.1 Conclusions ... 104
7.2 Future work ... 105
Author's Publications ... 107
References ... 110

Abstract

Illuminating light-emitting diodes (LEDs) enabled visible light communication (VLC) has attracted ever-increasing attention in recent years, due to the rapid development of solid-state lighting technology. The LEDs in general VLC systems play a dual role of providing simultaneous illumination and high-speed wireless data communication in typical indoor environments. Compared with traditional radio-frequency (RF) systems, VLC has many inherent advantages including license-free spectrum, high data rate, cost-effective front-ends, high security, electro-magnetic interference (EMI)-free operation, etc. By exploiting high-speed, bidirectional and fully networked VLC in indoor environments, light-fidelity (Li-Fi) can be realized which is envisioned as a promising complementary technology to the widely used wireless-fidelity (Wi-Fi). Nevertheless, the development and deployment of high-speed and large-coverage indoor VLC systems face many critical issues, such as the small 3-dB modulation bandwidth of commercially available off-the-shelf white LEDs, the limited coverage of each LED access point (i.e., optical attocell) due to the constraints of both illumination and communication, the inter-cell interference (ICI) in indoor multi-cell VLC systems, and the seamless integration of VLC with the last-mile optical access networks for hybrid wired and wireless indoor optical access. The main objectives of this thesis are to address the above issues, and propose and develop advanced transmission, modulation and detection techniques to improve the performance of VLC systems.

Multiple-input multiple-output (MIMO) transmission and orthogonal frequency division multiplexing (OFDM) are two effective technologies to improve the capacity of indoor VLC systems. Due to the intensity modulation and direct detection (IM/DD) nature of LEDs based VLC systems, Hermitian symmetry (HS) is usually imposed before performing the inverse fast Fourier transform (IFFT), so as to obtain LED-compatible real-valued OFDM signals. However, imposing HS doubles the size of IFFT/FFT and hence the complexity of OFDM transmitters/receivers. To address this problem, firstly, this thesis proposes a non-HS OFDM (NHS-OFDM) scheme for indoor MIMO-VLC systems. By transmitting the real and imaginary parts of a complex-valued OFDM signal via a pair of white LEDs, NHS-OFDM circumvents the HS constraint. Analytical and experimental results show that an indoor MIMO-VLC system using NHS-OFDM achieves superior bit error rate (BER) performance than the same system using conventional HS based OFDM (HS-OFDM), resulting in improved communication coverage. Moreover, the impact of LED pairing on the performance of NHS-OFDM based indoor MIMO-VLC systems is also analyzed.

In indoor MIMO-VLC systems, line-of-sight (LOS) transmission is usually dominant and the optical channel gains between one LED and two closely placed photo-detectors (PDs) could be very similar, leading to high spatial correlation that might severely degrade the performance of MIMO-VLC systems. In order to reduce channel correlation and improve multiplexing gain, imaging receivers (ImRs) have been applied in MIMO-VLC systems to replace widely used non-imaging receivers (NImRs). However, the field-of-view (FOV) of conventional ImRs is relatively small which limits the coverage of an indoor MIMO-VLC system. Therefore, an imaging angle diversity receiver (ImADR) is further proposed and investigated for indoor MIMO-VLC systems. By using angle diversity PDs instead of vertically oriented PDs, the proposed ImADR has a much wider FOV and achieves higher optical channel gain than the conventional ImR. Analytical and simulation results reveal that an indoor MIMO-VLC system using the proposed ImADR can achieve significantly improved communication coverage than the same system employing a conventional ImR.

In practical scenarios, an indoor VLC system usually consists of multiple cells, i.e., optical attocells, so as to achieve full coverage of a typical indoor environment. However, ICI is a major issue that could greatly degrade the performance of indoor multi-cell VLC systems. So far, many frequency division based ICI mitigation techniques have been proposed such as the RF subcarrier allocation technique, OFDM or discrete multi-tone (DMT) enabled dynamic subcarrier allocation technique, etc. Although ICI can be mitigated by using these schemes, spectrum partitioning is required which could substantially reduce the achievable capacity of each cell. In order to efficiently mitigate ICI without losing the achievable cell capacity, this thesis also proposes an angle diversity multi-element receiver (ADMER) based ICI mitigation technique for indoor multi-cell VLC systems. Compared with the conventional frequency division based ICI mitigation techniques, the proposed ADMER enabled ICI mitigation technique enjoys three main advantages including improved signal-to-interference-and-noise ratio (SINR), reduced SINR fluctuation and higher cell capacity.

Next generation access networks are expected to provide high-speed hybrid wired and wireless services for end users. OFDM based passive optical network (OFDM-PON) has been considered as a promising candidate for high-speed wired access due to its low cost, high spectral efficiency, robustness to chromatic dispersion, and flexibility of bandwidth allocation. As an alternative and complementary technology to RF based indoor wireless communication, VLC can provide high-speed and EMI-free indoor optical wireless access. Therefore, in order to integrate VLC with OFDM-PON systems for indoor hybrid wired and wireless optical access, an integrated VLC and OFDM-PON system is proposed and investigated, by using an adaptive envelope modulation technique.

List of Abbreviations

ADMER	Angle Diversity Multi-Element Receiver
APD	Avalanche Photo-Diode
ASE	Area Spectral Efficiency
AWGN	Additive White Gaussian Noise
BER	Bit Error Rate
BF	Blue Filter
CP	Cyclic Prefix
CSK	Color Shift Keying
DD	Direct Detection
De-MUX	De-Multiplexing
DMT	Discrete Multi-Tone
DSP	Digital Signal Processing
EGC	Equal-Gain Combining
EMI	Electro-Magnetic Interference
EVM	Error Vector Magnitude
FBMC	Filter Bank Multi-Carrier
FDE	Frequency Domain Equalization
FDM	Frequency Division Multiplexing
FEC	Forward Error Correction
FFT	Fast Fourier Transform
FHT	Fast Hartley Transform
FOV	Field-of-View
FSO	Free-Space Optical
ICI	Inter-Cell Interference
IFFT	Inverse Fast Fourier Transform
IM	Intensity Modulation
ImADR	Imaging Angle Diversity Receiver
ImR	Imaging Receiver
ISI	Inter-Symbol Interference
LED	Light-Emitting Diode
Li-Fi	Light-Fidelity
LOS	Line-of-Sight
LPF	Low-Pass Filter
MIMO	Multiple-Input Multiple-Output

MRC	Maximal-Ratio Combining
NImADR	Non-Imaging Angle Diversity Receiver
NImR	Non-Imaging Receiver
OCC	Optical Camera Communication
OFDM	Orthogonal Frequency Division Multiplexing
OFDMA	Orthogonal Frequency Division Multiple Access
OLT	Optical Line Terminal
ONU	Optical Network Unit
OOK	On-Off Keying
OPC	Optimum Combining
PAM	Pulse Amplitude Modulation
PAPR	Peak-to-Average Power Ratio
PD	Photo-Detector
PIN	Positive-Intrinsic-Negative
PON	Passive Optical Network
PRBS	Pseudo Random Binary Sequence
PSK	Phase Shift Keying
QAM	Quadrature Amplitude Modulation
QoS	Quality-of-Service
RC	Repetition Coding
RF	Radio Frequency
RIC	Real-and-Imaginary Combiner
RIS	Real-and-Imaginary Separator
RoF	Radio-over-Fiber
SBC	Select-Best Combining
SC-FDE	Single-Carrier Frequency Domain Equalization
SINR	Signal-to-Interference-and-Noise Ratio
SISO	Single-Input Single-Output
SM	Spatial Modulation
SMP	Spatial Multiplexing
SNR	Signal-to-Noise Ratio
SPAD	Single-Photon Avalanche Diode
TS	Training Sequence
VLC	Visible Light Communication
VLP	Visible Light Positioning
Wi-Fi	Wireless-Fidelity
ZF	Zero-Forcing

List of Figures

Figure 1.1. Data rate versus distance for short-range wireless technologies and standards [15]. 2

Figure 1.2. The big picture of VLC research and our contributions. 4

Figure 2.1. Block diagram of a general VLC system. 10

Figure 2.2. Illustration of the geometric setup of a VLC system 12

Figure 2.3. Block diagrams of (a) OFDM and (b) SC-FDE [71] 16

Figure 2.4. Illustration of three MIMO transmission schemes (a) RC, (b) SMP and (c) SM in a 2×2 MIMO-VLC system [33]. 19

Figure 2.5. Illustration of VLC based V2I and V2V systems [86]. 21

Figure 2.6. Illustration of VLC based underwater communication [116] 21

Figure 2.7. Illustration of VLC based in-flight communication [121]. 22

Figure 2.8. Illustration of VLC based indoor positioning [8] 23

Figure 2.9. Illustration of VLC based human sensing [130]. 23

Figure 3.1. Block diagrams of a 2×2 MIMO-VLC system using (a) conventional HS-OFDM and (b) the proposed NHS-OFDM 27

Figure 3.2. Schematic diagrams of a NHS-OFDM based 2×2 MIMO-VLC system using (a) a NImR and (b) an ImR 29

Figure 3.3. (a) SNR along the X direction with Y = 0 m employing an ImR and (b) BER versus SNR for 16QAM-OFDM over an AWGN channel. 33

Figure 3.4. BER versus receiver position offset along the X direction with Y = 0 m for the 2×2 MIMO-VLC system employing (a) a NImR and (b) an ImR 34

Figure 3.5. Communication coverage area of the 2×2 MIMO-VLC system for a target BER of 3.8×10^{-3} employing (a) NImR and (b) ImR 35

Figure 3.6. Experimental setup of the 2×2 MIMO-VLC system using ImR 37

Figure 3.7. Measured electrical spectra of the received real (Re) and imaginary (Im) parts of the NHS-OFDM signal (a) without pre-FDE and (b) with pre-FDE 39

Figure 3.8. Measured BER versus receiver position offset with a distance of 100 cm. 40

Figure 3.9. Cluster formation in (a) square and (b) hexagonal LED layout where red “×” indicates an LED 41

Figure 3.10. LED pairing: (a) parallel pairing in a square cluster, (b) cross pairing in a square cluster, (c) parallel pairing in a rhombic cluster, and (d) cross pairing in a rhombic cluster........ 42

Figure 3.11. Schematic diagram of a 2N-channel imaging MIMO-VLC system with N pairs of LEDs using NHS-OFDM. 43

Figure 3.12. Two LED placements (a) square and (b) rhombus 46

Figure 3.13. (a) BER versus X with Y = 2.5 m for a square LED placement, (b) BER versus Y with X = 2.5 m for a square LED placement, (c) BER versus X with Y = 2.5 m for a rhombic LED placement, and (d) BER versus Y with X = 2.5 m for a rhombic LED placement 48

Figure 3.14. Communication coverage of the four-channel imaging MIMO-VLC system at a target BER of 3.8×10^{-3} for (a) a square LED placement and (b) a rhombic LED placement. The average transmitted optical power per LED is 8 W........ 50

Figure 3.15. Communication coverage area versus average transmitted optical power per LED at a target BER of 3.8×10^{-3} for (a) a square LED placement and (b) a rhombic LED placement 52

Figure 4.1. Schematic diagram of the proposed ImADR........ 56

Figure 4.2. Side views of (a) a conventional ImR using vertically oriented PDs and (b) the proposed ImADR using angle diversity PDs, both with the same horizontal size 56

Figure 4.3. Half-angle FOV versus a/f for ImR and ImADR 57

Figure 4.4. Area of detector array versus half-angle FOV........ 59

Figure 4.5. Optical channel gain improvement in dB versus a/f for a range of b. 61

Figure 4.6. Geometric setup of the four-channel imaging MIMO-VLC system. 63

Figure 4.7. BER versus average transmitted optical power. Markers and lines show the simulation and analytical results, respectively........ 64

Figure 4.8. Communication coverage comparison for a target BER of 10^{-3} with an average transmitted optical power of 8 W. 65

Figure 5.1. (a) Top view and (b) side view of the proposed ADMER. Only the top detector and the n-th side detector are shown for illustration 67

Figure 5.2. Experimental setup of a two-cell OFDM-VLC system. 70

Figure 5.3. Top view of an ADMER with $N_r = 3$.. 70

Figure 5.4. Measured SINR versus receiver position offset using an SER........................ 72

Figure 5.5. Measured SINR versus inclination angle of side detectors in the ADMER. 72

Figure 5.6. Measured SINR versus receiver position offset using NADMER and ADMER. 73

Figure 5.7. Top view of the ADMER with (a) $N_r = 5$, (b) $N_r = 6$, (c) $N_r = 7$ and (d) $N_r = 9$.. 75

Figure 5.8. (a) Geometry for optical channel gain calculation of the side detectors and (b) LED projection on the detector plane.. 75

Figure 5.9. Geometric setup of the four-cell VLC system in a 5m×5m×3m room............ 78

Figure 5.10. Horizontal illumination distribution around the receiving plane.................. 80

Figure 5.11. SINR distribution around the receiving plane using an SER......................... 81

Figure 5.12. Contour plots of average SINR (dB) at the central position of the receiving plane for (a) $N_r = 5$, (b) $N_r = 6$, (c) $N_r = 7$ and (d) $N_r = 9$.................................. 82

Figure 5.13. SINR versus rotation angle of the ADMER for (a) $N_r = 5$, (b) $N_r = 6$, (c) $N_r = 7$ and (d) $N_r = 9$ 83

Figure 5.14. Average SINR distribution using an ADMER with $N_r = 5$. 84

Figure 5.15. Average SINR distribution using an ADMER with $N_r = 6$. 85

Figure 6.1. Conceptual diagram of the integrated VLC and OFDM-PON system. 89

Figure 6.2. Architecture of the integrated VLC and OFDM-PON system......................... 90

Figure 6.3. Principle of adaptive envelope modulation. 91

Figure 6.4. Time traces of (a) M-PAM overlaid CE-OFDM signal after adaptive envelope modulation and (b) the obtained M-PAM signal after envelope detection in a slow PD. 92

Figure 6.5. BER versus electrical SNR of the unipolar CE-OFDM signal for 64QAM based CE-OFDM signal with 4PAM overlay. Markers and lines show the simulation and theoretical results, respectively. 96

Figure 6.6. BER versus electrical SNR of the unipolar CE-OFDM signal for the overlaid 4PAM signal without VLC wireless transmission. Markers and lines show the simulation and theoretical results, respectively.. 99

Figure 6.7. Optimal peak amplitude ratio versus electrical SNR of the unipolar CE-OFDM signal for 64QAM based CE-OFDM signal with *M*-PAM overlay..................... 100

Figure 6.8. BER versus average received SNR for *M*-PAM based indoor VLC wireless access 101

Figure 6.9. Achievable bit rate of indoor VLC wireless access versus the number of CE-OFDM symbols in one PAM symbol. 102

List of Tables

Table 2.1. Comparison of different modulation techniques in VLC................................. 15

Table 3.1. Key parameters of the 2×2 MIMO-VLC system 32

Table 3.2. Key parameters of the four-channel MIMO-VLC system 46

Table 4.1. Simulation parameters... 63

Table 5.1. Experimental SINR performance comparison 74

Table 5.2. Key parameters of system setup... 79

Table 5.3. SINR fluctuation comparison... 83

Table 5.4. Average SINR fluctuation comparison 85

Chapter 1 Introduction

1.1 Background and motivations

1.1.1 Background

In the last two decades, we have witnessed an exponential growth of mobile data traffic in both indoor and outdoor environments, due to the ever-increasing demand for broadband wireless services such as high-definition television (HDTV), computer network applications, mobile videophones, video conferencing, high-speed Internet access, and so on [1]. From Shannon's initial work in information theory, it is well known that the capacity of a wireless communication system or network is directly proportional to the available bandwidth. Due to the fast growth of data traffic, the current radio-frequency (RF) spectrum is proving to be scarce to meet the ever-increasing demand for bandwidth [2].

Recently, the rapid development of solid-state lighting technology, especially high-brightness light-emitting diodes (LEDs), has attracted tremendous attention [3]. According to the energy savings forecast from United States Department of Energy, the average luminous efficacy of best-in-class commercial off-the-shelf LEDs is as high as 113 lumens/watt in 2015 and it will reach 200 lumens/watt by the year 2020 [4]. Compared with conventional incandescent and fluorescent lamps which respectively provide an average luminous efficacy of about 15 and 60 lumens/watt, it is a many-fold increase in average luminous efficacy by employing high-brightness LEDs. Moreover, the life-span of LEDs ranges from 25 000 to 50 000 hours which is significantly higher than compact fluorescent lamps which is only about 10 000 hours [4]. Owing to the many advantages of LEDs, such as high radiative efficiency, long lifetime, high tolerance to humidity, limited heat generation and cost-effectiveness, visible light LEDs are anticipated to gradually replace conventional incandescent and fluorescent lamps for indoor illumination in the near future [5, 6].

Besides energy-efficient illumination, the intensity levels of LEDs can also be switched at a very fast speed, which is fast enough that human eyes cannot perceive. Therefore, visible light LEDs can serve a dual-function of simultaneous illumination and communication. Compared with the limited RF spectrum, visible light spectrum includes hundreds of terahertz of license-free bandwidth, which can be exploited for high-speed wireless data communications [7]. As a promising complementary technology to traditional RF-based communication systems, visible light communication (VLC) employing existing illuminating LEDs has been triggering ever-increasing interest in recent years [8–10]. The first work on VLC was reported by

Japanese researchers from Keio University in year 2000, where white LEDs were used to build wireless home links [11]. A fundamental analysis on VLC was further reported in year 2004, where the basic system model of an indoor VLC system using white LEDs was described [12]. After that, worldwide attention has been attracted on the development of high-speed VLC systems using white LEDs. In 2003, Visible Light Communications Consortium (VLCC) was formed in Japan, which proposed two standards, i.e., Visible Light Communication System Standard and Visible Light ID System Standard, by 2007 [13]. In 2011, the first IEEE standard (IEEE 802.15.7) for visible light communication was proposed, which included the link layer and physical layer design specifications [14].

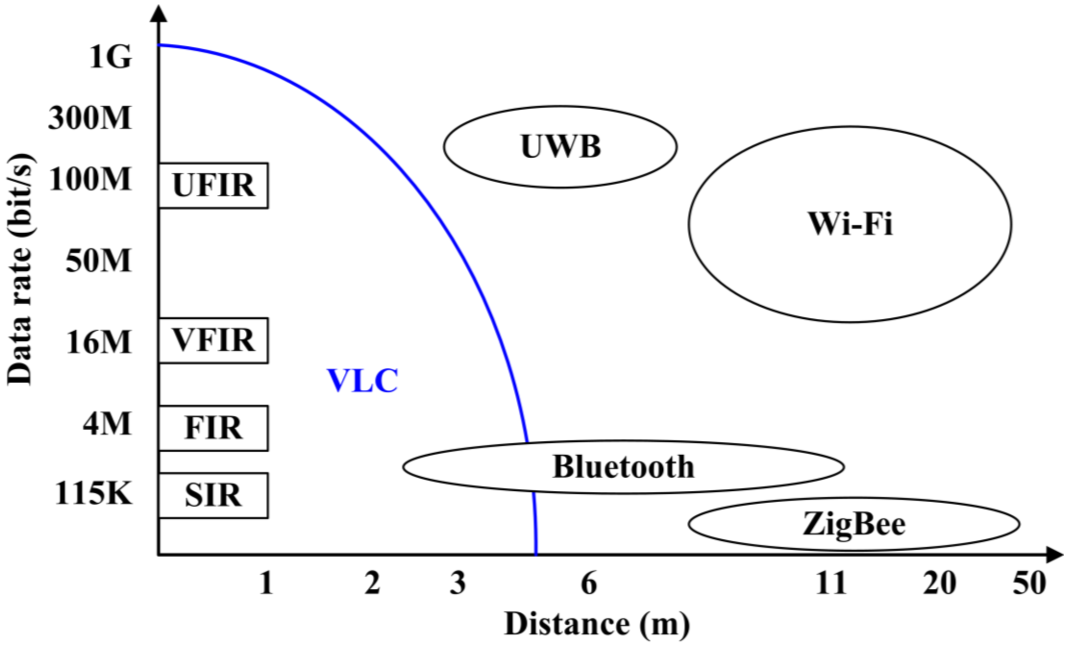

Figure 1.1. Data rate versus distance for short-range wireless technologies and standards [15].

Fig. 1.1 shows the relationship between data rate and transmission distance for various short-range wireless technologies and standards [15]. It can be seen that VLC is suitable for indoor applications where the transmission distance is about a few meters and the data rate is around or above 100 Mbit/s. Although the transmission distance of VLC is shorter than the widely used wireless-fidelity (Wi-Fi), VLC can achieve much higher data rate (up to a few Gbit/s) than the latest Wi-Fi (about 300 Mbit/s for IEEE 802.11n) [8]. Compared with traditional RF based indoor wireless communication systems, white LEDs enabled VLC systems have many inherent advantages such as unlimited license-free bandwidth (400–700 nm), potentially high data rate, no RF interference (RFI)/electromagnetic interference (EMI) radiation, low-cost front ends, high security, and relatively low power consumption [7].

Despite the above-mentioned advantages, the development and deployment of high-speed and large-coverage VLC systems face several challenges, which are summarized as follows

- *Small modulation bandwidth of white LEDs.* Due to long photoluminescence lifetime of the phosphor, the 3-dB modulation bandwidth of commercially off-the-shelf white LEDs is only about a few MHz [16]. Since the capacity of a wireless communication system is directly proportional to the available modulation bandwidth, the capacity of indoor VLC systems is greatly limited by the small 3-dB modulation bandwidth of the white LEDs.
- *Limited communication coverage.* Because of the strong multipath effects, RF based communication systems can easily achieve full coverage of an indoor environment with only a few signal transmitters. However, it is a big challenge for a VLC system to achieve full coverage of an indoor environment considering that line-of-sight (LOS) transmission is dominant in general white LEDs based VLC systems [17].
- *Significant inter-cell-interference (ICI).* Since the coverage area of one VLC cell, i.e., an optical attocell, is relatively small, a VLC system or network usually consists of multiple optical attocells in a relatively large indoor environment, so as to meet the requirements of both indoor illumination and communication [18]. In order to fully cover an indoor environment, the coverage areas of adjacent cells inevitably overlap and users located in the overlapping areas receive strong ICI, which could severely degrade the communication quality [18].
- *System integration.* Next-generation access networks should provide simultaneous high-speed wired and wireless services for indoor users [19]. Passive optical network (PON) is a promising candidate for last-mile high-speed wired access, due to its cost-effectiveness, high capacity and easy upgradability [20]. As a potential high-speed indoor wireless access technology, VLC needs to be seamlessly integrated with PON systems. Due to different quality-of-service (QoS) requirements of different indoor users, variable-rate VLC wireless access should be supported [21].

So far, extensive research has been done to address the above challenges of VLC and a sketch of the big VLC picture is presented in Fig. 1.2.

In recent years, great attention has been drawn on capacity improvement of white LEDs based VLC systems. A lot of techniques have been proposed in literature, which can be mainly divided into four categories: (1) the application of AlInGaN, InGaN or GaN based micro LED (μLED) which naturally has a large 3-dB modulation bandwidth of more than 100 MHz [22–25]; (2) frequency domain equalization (FDE) techniques to increase the 3-dB modulation bandwidth of commercially off-the-shelf white LEDs, which can be performed either at the transmitter side (i.e., pre-FDE) or at the receiver side (i.e., post-FDE), either by software through digital signal processing (DSP) or by hardware circuits [26–29]; (3) spectral-efficient modulation schemes such as orthogonal frequency division multiplexing (OFDM) and single-carrier frequency domain equalization (SC-FDE), employing high-order quadrature amplitude modulation (QAM) constellations [30, 31]; (4) various multiple-input multiple-output (MIMO) transmission schemes by exploiting the existing LEDs, including spatial multiplexing, spatial modulation, etc. [32, 33].

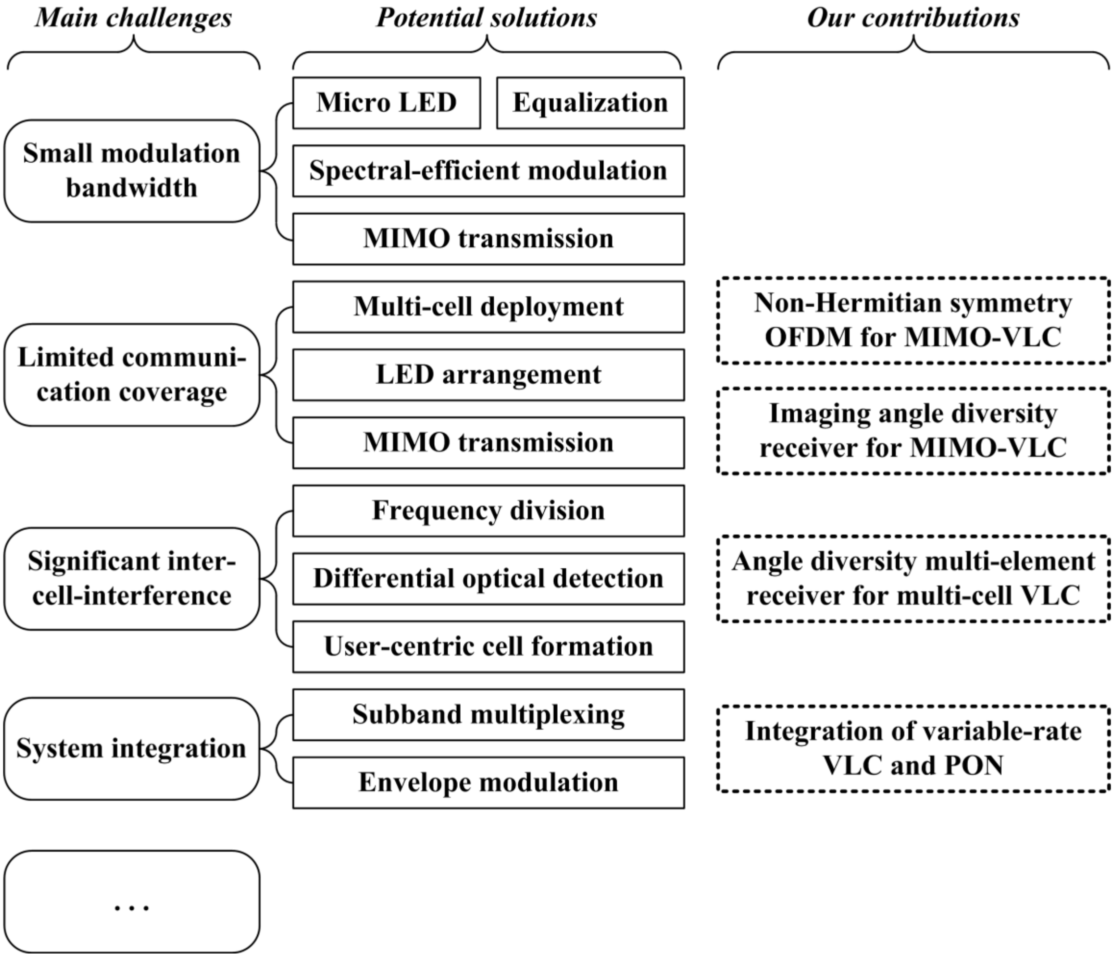

Figure 1.2. The big picture of VLC research and our contributions.

As can be seen, a lot of work has been carried out on the development of indoor white LEDs based VLC systems. However, most of the work mainly focused on the improvement of data rate and/or the extension of transmission distance, while the communication coverage of an indoor VLC system has not been fully investigated in literature. Since the communication coverage area of one cell is very limited, the easiest way to achieve a large communication coverage area is to deploy multiple cells in an indoor environment [18]. Besides multi-cell deployment, increasing the coverage area per cell is another way to substantially increase the overall communication coverage of an indoor multi-cell VLC system. Two techniques have been reported to for coverage improvement per cell, including LED arrangement which aims to maximize the achievable area spectral efficiency (ASE) [34] or to reduce the signal-to-noise ratio (SNR) fluctuation with in the cell [35], and MIMO transmission which exploits multiple spatially separated LEDs to increase the coverage per cell [32].

The overall performance of an indoor multi-cell VLC system could be significantly degraded by ICI. A few techniques have been proposed for ICI mitigation in indoor multi-cell VLC systems, including frequency division techniques based on frequency division multiplexing (FDM), OFDM, or filter bank multicarrier (FBMC) [36–38], differential optical detection based on polarization division [39], and user-centric cell formation approach [40].

How to integrate VLC with PON systems is a critical issue for the practical implementation of VLC in indoor environments. Several integration schemes have been proposed in literature, including subband multiplexing using OFDM or SC-FDE [41–44], and envelope modulation using on-off keying (OOK) overlaid OFDM [45].

1.1.2 Motivations

Although many potential solutions have been reported to address the challenges of VLC, as can be seen from Fig. 1.2, there still exist many problems in developing high-speed and large-coverage indoor VLC systems with enhanced tolerance against ICI and easy integration with last-mile optical access networks. Due to the rapid development of DSP technologies, this thesis is motivated to solve the existing problems of VLC by using advanced modulation and detection techniques. More specifically, the main motivations are listed as follows

- MIMO is a very natural and effective way to increase the capacity of white LEDs based bandwidth-limited VLC systems [32]. Moreover, by utilizing multiple spatially separated LEDs, MIMO-VLC systems also have increased communication coverage than single-input single-output (SISO) based VLC systems. However, due to the LOS transmission characteristic and small spatial separation of detectors in MIMO-VLC receivers, conventional MIMO-VLC systems suffer from high channel correlation, which not only reduces the achievable capacity, but also limits the communication coverage [7]. Therefore, it is of great significance to develop advanced modulation and detection techniques for performance improvement of MIMO-VLC systems.

- Conventional frequency division based ICI mitigation techniques can eliminate the interference efficiently, but the achievable capacity within each cell of the multi-cell VLC system would be substantially reduced due to spectrum partitioning and the use of a large guard band [36]. Although the guard band becomes negligible when FBMC is used which greatly suppressed spectrum sidelobes [37], the capacity improvement achieved by reducing the guard band is very limited since spectrum partitioning is still performed. Hence, it would be particularly interesting if the ICI can be mitigated without spectrum partitioning. By adopting in-band ICI mitigation based on advanced detection techniques, the achievable capacity within each cell of the indoor multi-cell VLC system could be significantly increased.

- Subband multiplexing is the most straightforward way to integrate VLC with PON based last-mile optical access networks. Nevertheless, electrical filtering is always used in each optical network unit (ONU) to filter out the subband for VLC wireless access [41–44]. In order to support different QoS requirements of indoor users [21], the data rate of VLC wireless access should be adjustable. Hence, tunable electrical filters should be used to guarantee the reconfigurability of each ONU, which are cost-sensitive and adaptive control is also required. By encoding a low-speed OOK signal (for VLC wireless access) on the envelope of a high-speed OFDM signal (for fiber based wired access), the electrical filters are no longer required [45]. However, the envelope of a conventional OFDM signal fluctuates significantly, which results in inherent distortion that would degrade the performance of the overlaid OOK signal. As a result, it is of practical meaning to explore advanced modulation techniques for seamless integration of variable-rate VLC with PON systems.

1.2 Major contributions

In order to solve the above-mentioned problems, novel advanced modulation and detection techniques are explored and developed in this thesis. The main contributions of this thesis, as highlighted in Fig. 1.2, are summarized as follows:

- Due to high channel correlation caused by the LOS transmission characteristic and the small spatial separation of detectors in MIMO-VLC receivers, the performance of an indoor MIMO-VLC system is limited, resulting in relatively small communication coverage. This thesis first proposes a non-Hermitian symmetry OFDM (NHS-OFDM) modulation technique to improve the performance of indoor MIMO-VLC systems. The proposed NHS-OFDM modulation technique removes the Hermitian symmetry constraint, by transmitting the real and imaginary parts of a complex-valued OFDM signal via a pair of LEDs. Analytical and experimental results show that an MIMO-VLC system employing NHS-OFDM exhibits lower or comparable computational complexity as the system utilizing conventional Hermitian symmetry based OFDM (HS-OFDM), but achieves much better bit error rate (BER) performance, leading to improved communication coverage. (Chapter 3)

- Imaging based receivers (ImRs) have been widely applied in MIMO-VLC systems to replace the widely used non-imaging receivers (NImRs), due to their ability to reduce channel correlation and improve multiplexing gain [32]. Nevertheless, the field-of-view (FOV) of conventional ImRs is relatively small which limits the communication coverage of indoor MIMO-VLC systems [46]. In this thesis, a novel imaging angle diversity receiver (ImADR) is proposed for indoor MIMO-VLC systems. In the proposed ImADR, angle diversity detectors are utilized instead of vertically oriented detectors. As a result, ImADR has a much wider FOV and achieves higher optical channel gains than the conventional ImR. Analytical and simulation results verify that an indoor MIMO-VLC system using the proposed ImADR can achieve significantly improved communication coverage than the system using an ImR. (Chapter 4)

- The ICI in multi-cell VLC systems can be mitigated by using conventional frequency division based techniques, but the achievable capacity of each cell in the multi-cell VLC system is inevitably sacrificed. Differential optical detection using polarization division [39] and user-centric cell formation techniques [40] have been reported for in-band ICI mitigation without sacrificing cell capacity. However, complicated cell planning and accurate system control are usually required, which greatly increases the implementation complexity of indoor multi-cell VLC systems. In order to efficiently mitigate ICI without losing cell capacity and increasing implementation complexity, an angle diversity multi-element receiver (ADMER) based ICI mitigation technique is proposed and examined for indoor multi-cell VLC systems. Experimental and analytical results demonstrate that the proposed ADMER can effectively mitigate ICI and significantly reduce signal-to-interference-and-noise ratio (SINR) fluctuation in indoor multi-cell VLC systems, while achieving a high cell capacity and relatively low implementation complexity. (Chapter 5)

- Variable-rate VLC wireless access should be integrated with last-mile PON systems to support high-speed hybrid wired and wireless services for users in typical indoor environments [21]. OFDM based passive optical network (OFDM-PON) is promising for high-speed wired access [47]. In this thesis, an integrated VLC and OFDM-PON system based on adaptive envelope modulation is proposed and analyzed for indoor hybrid wired and wireless optical access. The data for wired access is carried by a conventional OFDM signal and the data for VLC wireless access is carried by an *M*-

ary pulse amplitude modulation (*M*-PAM) signal modulated onto the envelope of the OFDM signal. In order to achieve a constant envelope and thus eliminate the inherent amplitude distortions, discrete phase modulation after OFDM encoding is performed to obtain a constant envelope OFDM (CE-OFDM) [48]. By using adaptive envelope modulation in the optical line terminal (OLT), variable-rate VLC wireless access can be achieved in the integrated VLC and OFDM-PON system. (Chapter 6)

1.3 Thesis organization

This thesis consists of seven chapters, which is organized as follows

Chapter 1 briefly introduces the background and the motivations of indoor VLC systems, and summarizes the major contributions of the work in this thesis.

Chapter 2 presents a comprehensive literature review on the system model and the state-of-the-art modulation and detection techniques of VLC. Moreover, a review on MIMO-VLC is particularly conducted, including both non-imaging and imaging MIMO-VLC systems. After that, various potential applications of VLC are also introduced.

Chapter 3 proposes a NHS-OFDM modulation technique for indoor MIMO-VLC systems, which can enhance the BER performance and hence improve the communication coverage of the system. The principle of NHS-OFDM is first introduced and then the analytical BER expression of an MIMO-VLC system using NHS-OFDM is derived. The performance of a 2×2 MIMO-VLC system using conventional HS-OFDM and the proposed NHS-OFDM is investigated and compared by both experiments and numerical analysis. Furthermore, the impact of LED pairing in a general MIMO-VLC system using NHS-OFDM is also analyzed.

In Chapter 4, an ImADR is proposed for communication coverage improvement of indoor MIMO-VLC systems. The principle of ImADR is first presented and a detailed comparison between conventional ImR and the proposed ImADR is then conducted in terms of FOV, area of detector array and optical channel gain. After that, the BER performance of an indoor four-channel MIMO-VLC system employing the proposed ImADR is investigated.

Chapter 5 analyzes an ADMER for ICI mitigation and SINR fluctuation reduction in indoor multi-cell VLC systems. The principle of ADMER is discussed. After that, a two-cell VLC system using an ADMER with three detectors is first experimentally demonstrated. Then, a four-cell VLC system using an ADMER with five, six, seven or nine detectors is numerically evaluated, with the consideration of receiver random rotation.

Chapter 6 investigates an integrated variable-rate VLC and OFDM-PON system for hybrid indoor wired and wireless optical access, by using an adaptive envelope modulation technique. The system architecture is first presented and then two key techniques (i.e., constant envelope OFDM and adaptive envelope modulation) for system integration are discussed. The BER performances of both fiber-based wired access and VLC wireless access are analyzed.

Chapter 7 gives the conclusions of the work and some recommendations on the future work are also provided.

Chapter 2 Literature Review

2.1 Introduction of VLC

VLC is the name given to an optical wireless communication system where the information is carried by visible light in the spectrum from about 400 to 700 nm [7]. Owing to the rapid development of LED technology, LEDs have been widely used as optical transmitters in VLC systems [8]. In white LEDs based indoor VLC systems, LEDs are employed for simultaneous illumination and communication [9]. Since the light emitted by LEDs is naturally incoherent, only intensity modulation/direct detection (IM/DD) can be used in VLC systems and hence only real-valued and non-negative signals can be transmitted by LEDs [10]. In this section, the fundamental of white LEDs based VLC systems is briefly reviewed. The system model is first introduced and then two key techniques of VLC systems, i.e., modulation and detection, are further discussed.

2.1.1 System model

Fig. 2.1 illustrates the block diagram of a general VLC system. The binary input data are first modulated to obtain a real-valued signal and then a DC bias is added to the modulated signal such that the generated signal is both real-valued and non-negative. After that, the resultant electrical signal is used to drive the LED that emits light into the free-space channel. At the receiver side, an optical concentrator or lens can be employed to concentrate the radiated light onto the photodetector (PD) and an optical filter can also be utilized to attenuate the unwanted ambient light [11, 12]. Subsequently, the received electrical signal is amplified and further demodulated to generate the output data.

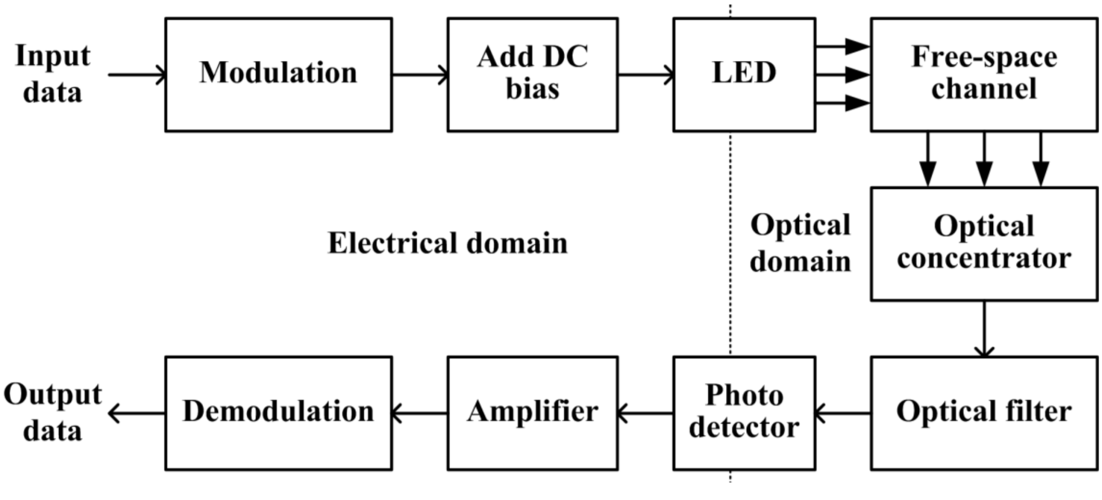

Figure 2.1. Block diagram of a general VLC system.

Considering that white LEDs are used for a dual function of simultaneous illumination and communication, LED lights have two basic properties, i.e., luminous intensity and transmitted optical power. The luminous intensity is used for expressing the brightness of an LED, while the transmitted optical power indicates the total energy radiated from an LED, which is a parameter from the point of view of optical communication [12].

Luminous intensity is the unit that indicates the energy flux per solid angle and it is related to the illuminance at an illuminated surface, where the energy flux is normalized with visibility. The luminous intensity is defined as

$$I = \frac{\mathrm{d}\Phi}{\mathrm{d}\Omega}, \tag{2.1}$$

where Φ is the luminous flux and Ω is the spatial angle. The luminous flux Φ can be obtained from the energy flux Φ_e as

$$\Phi = K_\mathrm{m} \int_{380}^{780} V(\lambda)\, \Phi_\mathrm{e}(\lambda) \mathrm{d}\lambda, \tag{2.2}$$

where K_m is the maximum visibility which is about 683 lm/W at the wavelength $\lambda = 555$ nm and $V(\lambda)$ is the standard luminosity curve.

The transmitted optical power P_t is the integral of the energy flux Φ_e in all directions, which is given by

$$P_t = K_\mathrm{m} \int_{\Lambda_\mathrm{min}}^{\Lambda_\mathrm{max}} \int_0^{2\pi} \Phi_\mathrm{e} \mathrm{d}\theta \mathrm{d}\lambda, \tag{2.3}$$

where Λ_min and Λ_max are determined by the sensitivity curve of the PD [7].

Fig. 2.2 illustrates the geometric setup of a VLC system. Without loss of generality, the LED can be assumed to have a Lambertian radiation pattern and hence the radiation intensity at a receiver surface is given by [12]

$$I(\phi) = I(0)\cos^m(\phi), \tag{2.4}$$

where ϕ is the angle of irradiance with respect to the axis normal to the transmitter surface, $I(0)$ is the central luminous intensity of the LED and m is the order of Lambertian emission which is defined by

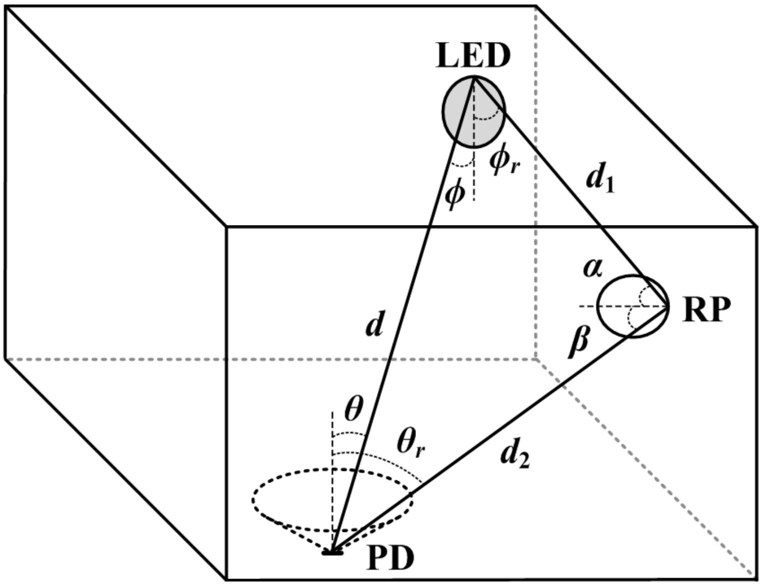

Figure 2.2. Illustration of the geometric setup of a VLC system.

$$m = \frac{\ln(2)}{\ln(\cos\Phi_{1/2})}, \tag{2.5}$$

where $\Phi_{1/2}$ is the semi-angle at half illuminance of the LED.

The horizontal illuminance at the receiver surface is expressed by

$$E_h = \frac{I(0)\cos^m(\phi)\cos(\theta)}{d^2}, \tag{2.6}$$

where θ is the angle of incidence with respect to the axis normal to the receiver surface and d is the distance between the LED and the receiver surface [7].

In typical indoor VLC systems, due to the LOS transmission and reflections from the surfaces within the room, a receiver can usually detect both LOS and diffuse components of the light emitted by the LED. The LOS optical channel DC gain h is calculated by [12]

$$h = \frac{(m+1)A_d}{2\pi d^2}\cos^m(\phi)T_s(\theta)g(\theta)\cos(\theta), \quad 0 \le \theta \le \Theta_{1/2}, \tag{2.7}$$

where A_d is the active area of the PD, $T_s(\theta)$ is the gain of the optical filter, $g(\theta)$ is the gain of the optical concentrator or lens, and $\Theta_{1/2}$ is half-angle FOV of the receiver. It should be noted that the LOS optical channel DC gain h becomes zero when the incident angle θ is outside the FOV of the receiver.

The optical concentrator gain $g(\theta)$ is given by

$$g(\theta)=\frac{n^2}{\sin^2\Theta_{1/2}}, \quad 0\le\theta\le\Theta_{1/2}, \tag{2.8}$$

where n is the refractive index of the optical concentrator.

Moreover, as illustrated in Fig. 2.2, the optical channel DC gain of the first reflection is calculated by [12, 49]

$$\mathrm{d}h_{ref}=\frac{(m+1)A_d}{2\pi^2 d_1^2 d_2^2}\rho\,\mathrm{d}A_{wall}\cos^m(\phi_r)\cos(\alpha)\cos(\beta)T_s(\theta_r)g(\theta_r)\cos(\theta_r), \quad 0\le\theta_r\le\Theta_{1/2}, \tag{2.9}$$

where d_1 is the distance between the LED and the reflective point (RP), d_2 is the distance between the RP and the receiver, ρ is the reflectance factor, $\mathrm{d}A_{wall}$ is the reflective area of a small region, ϕ_r is the angle of irradiance from the LED, α and β are the angle of incidence to the RP and the angle of irradiance from the RP, respectively, and θ_r is the angle of incidence to the receiving plane.

Therefore, the total received optical power of the receiver from the LED is given by

$$P_r=P_t h+\int_{walls} P_t\,\mathrm{d}h_{ref}. \tag{2.10}$$

It has been verified in [32] that the weakest LOS component is at least 7-dB higher in electrical power than the strongest diffuse component in typical indoor environments. For this reason, we can assume that the diffuse components are negligible and only consider the LOS component in the analysis of an indoor VLC system. Note that this assumption has been widely adopted in the literature [17, 23, 32, 34, 35].

Moreover, the wavelength used in VLC systems is around 400 to 700 nm, which is much smaller than the typical active area of a PD. As a result, multipath fading can be generally neglected in indoor VLC systems because of high spatial diversity [12, 52]. Nevertheless, performance degradation is still possible in the presence of multipath-induced inter-symbol interference (ISI) in certain scenarios and ISI mitigation techniques can be applied to improve the system performance [7].

Assuming that the LED has an average transmitted optical power P_0 and a modulation index ξ, the optical signal $s(t)$ at the output of the LED can be represented by [50]

$$s(t)=P_0[1+\ \xi\,x(t)]. \tag{2.11}$$

In Eq. (2.11), $x(t)$ is the normalized electrical modulating signal with $\sigma_x^2 = 1$. The modulation index is defined as the ratio of the LED's maximum current variation caused by the modulating signal to the LED bias current [51]. Assuming only LOS transmission, after removing the DC term, the received electrical signal $y(t)$ is expressed by

$$y(t) = RhP_0\xi x(t) + n(t), \tag{2.12}$$

where R is the responsivity of the PD, and $n(t)$ is the additive noise including both shot and thermal noises. The additive noise can be modeled as a real-valued additive white Gaussian noise (AWGN) with zero mean and variance $\sigma^2 = \sigma_{shot}^2 + \sigma_{thermal}^2$ [12]. The variances of shot and thermal noises are given as follows

$$\begin{cases} \sigma_{shot}^2 = 2q(RP_{rx} + I_{bg}I_2)B_n \\ \sigma_{thermal}^2 = 8\pi kT_K\eta A_d B_n^2 \left(\dfrac{I_2}{G} + \dfrac{2\pi\Gamma}{g_m}\eta A_d I_3 B_n\right) \end{cases}, \tag{2.13}$$

where q is the electronic charge, $P_{rx} = hP_0$ is the received optical power from the LED, I_{bg} is the background current due to ambient light, $I_2 = 0.562$ is the noise bandwidth factor, B_n is the equivalent noise bandwidth, k is the Boltzmann's constant, T_K is absolute temperature, η is the fixed capacitance of PD per unit area, G is the open-loop voltage gain, Γ is the FET channel noise factor, g_m is the FET transconductance, and the noise bandwidth factor $I_3 = 0.0868$ [7].

Based on Eq. (2.12), the SNR of the received electrical signal $y(t)$ can be obtained by

$$SNR = \frac{(RhP_0\xi)^2}{\sigma_{shot}^2 + \sigma_{thermal}^2}. \tag{2.14}$$

It can be seen that the SNR of the received signal is determined by many factors, including the responsivity of the PD, the optical channel DC gain, the average transmitted optical power, the modulation index of the LED, and the variances of the additive shot and thermal noises.

2.1.2 Modulation techniques

In VLC systems, as shown in Fig. 2.1, the input data are modulated into real-valued and non-negative signals before they are used to drive the LED. So far, many modulation techniques have been proposed for white LEDs based VLC systems. In this subsection, a brief overview of different modulation techniques that have been considered in VLC systems is provided. A comparison of the widely used modulation techniques is given in Table 2.1.

Table 2.1. Comparison of different modulation techniques in VLC

Modulation technique	**Spectral efficiency**	**System complexity**
OOK	Low	Low
CSK	Moderate	High
OFDM	High	High
SC-FDE	High	High

On-off keying (OOK): OOK is one of the simplest modulation schemes that have been used in VLC systems [26, 27, 32, 53–57]. In OOK-VLC, the LED is switched "on" and "off" when the data bit is "1" or "0", respectively. In the "off" state, the LED is not completely turned off; instead, the intensity of the light is simply reduced as long as the receiver could distinguish clearly between the "on" and "off" states [53]. Moreover, non-return-to-zero (NRZ) OOK is usually adopted in OOK-VLC systems, where the data bits "1" and "0" are represented by positive and negative currents [54]. In [55], S. Park *et al.* demonstrated a 10 Mb/s white LED based VLC system using NRZ-OOK. In [56], NRZ-OOK with blue filtering was employed the VLC system achieving a data rate of 40 Mb/s. In order to further increase the data rate of VLC systems, H. Minh *et al.* proposed to combine blue filtering with analogue equalization at the transmitter or receiver side using NRZ-OOK, achieving data rates of more than 100 Mb/s [26, 27]. In [57], a 614 Mb/s NRZ-OOK based VLC system was demonstrated where the duobinary technique with hybrid transmitter and receiver equalization was adopted. Although the implementation complexity of OOK modulation in VLC systems is very low, the spectral efficiency of OOK modulation is also low.

Color shift keying (CSK): CSK is a modulation scheme especially designed for VLC systems where multi-chip LEDs, such as red, green, and blue (RGB) LEDs, are used, which has been introduced in the new IEEE 802.15.7 standards [58]. In CSK, the transmitted bit corresponds to a specific color in the color space chromaticity diagram, which is defined by the CIE 1931 coordinates [59]. The chromaticity diagram maps all colors perceivable by human eyes to two chromaticity parameters, i.e., x and y [2]. The design and implementation of CSK in VLC systems have been extensively studied in literature [60–62]. Compared with OOK, CSK has a relatively higher spectral efficiency. However, CSK is not applicable to VLC systems where phosphor-based LEDs are used and moreover, the implementation of CSK requires a very complex circuit structure, which will significantly increase the system complexity [2].

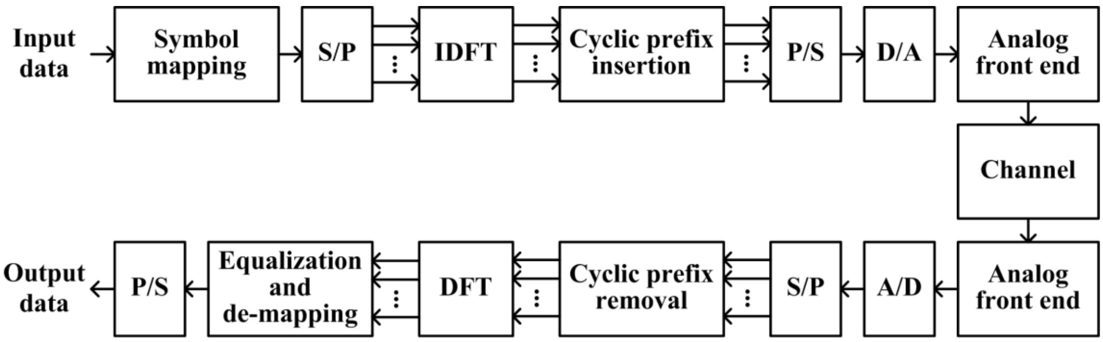

(a) OFDM

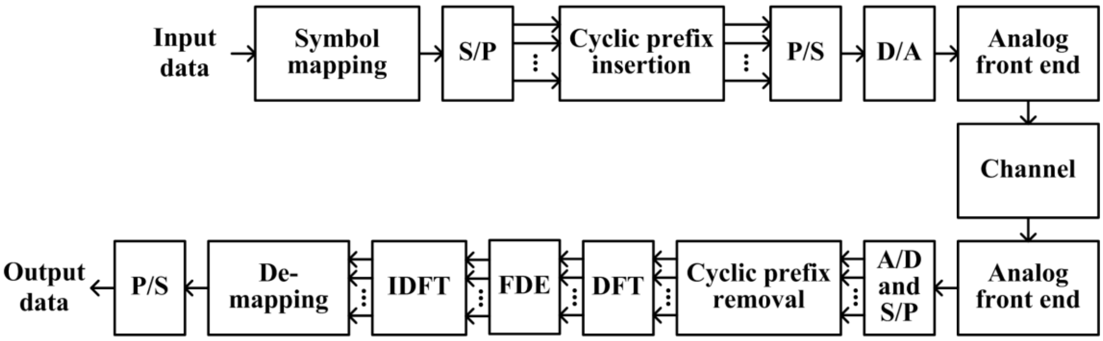

(b) SC-FDE

Figure 2.3. Block diagrams of (a) OFDM and (b) SC-FDE [71].

Orthogonal frequency division multiplexing (OFDM): In OFDM, multiple orthogonal sub-carriers are utilized to simultaneously transmit parallel data streams and hence inter-symbol-interference (ISI) can be reduced. Moreover, OFDM can achieve high spectral efficiency by adopting high-order QAM constellation mappings [63]. Due to its high spectral efficiency and robustness against ISI and multipath fading, OFDM has been widely applied in white LEDs based VLC systems [24, 29, 30, 64]. Since only real-valued signals can be transmitted in VLC systems, Hermitian symmetry is usually imposed before performing the inverse fast Fourier transform (IFFT) in OFDM based VLC systems [30]. As a special case of OFDM, DMT with adaptive bit and/or power loading has also been considered to increase the capacity of VLC systems [65–67]. Another key advantage of OFDM is that it can provide flexible subcarrier allocation and hence OFDM can also be considered as an effective multiple access technique, i.e., orthogonal frequency-division multiple access (OFDMA) [52, 68]. Nevertheless, OFDM surfers from high peak-to-average power ratio (PAPR) which could degrade the system performance of and several schemes have been proposed for the PAPR reduction in OFDM based VLC systems [69, 70].

Single carrier frequency domain equalization (SC-FDE): SC-FDE is a single-carrier (SC) modulation technique combined with frequency domain equalization (FDE). Compared with OFDM, SC-FDE has lower PAPR and hence achieves better BER performance than OFDM

[71]. Due to its improved performance, SC-FDE has also been considered in white LEDs based VLC systems utilizing various modulation formats such as OOK [72], pulse amplitude modulation (PAM) [73], and QAM [31, 74]. Although SC-FDE outperforms OFDM in terms of PAPR and meanwhile has a comparable implementation complexity as OFDM, SC-FDE cannot support flexible resource allocation in comparison to OFDM. Fig. 2.3 compares the principles of OFDM and SC-FDE.

2.1.3 Detection techniques

After free-space propagation, the light emitted by LEDs is detected to obtain the transmitted information. In white LEDs based VLC systems, several detection techniques can be utilized to convert the radiated light to electrical signals, which are listed as follows.

Photodiode (PD): PD is the most widely used optical-to-electrical converters in white LEDs based VLC systems [12]. More specifically, there are two types of PDs that can be employed in VLC systems: one is a positive-intrinsic-negative (PIN) diode and the other is an avalanche photodiode (APD) [16]. In comparison to a PIN diode, an APD has a much higher sensitivity in detecting optical signals, which is commonly used in high-speed VLC systems [65, 66, 75].

Single-photon avalanche diode (SPAD): Recently, SPAD based receivers have attracted great attention in white LEDs based VLC systems [76–78]. In PIN or APD based VLC systems, transimpedance amplifiers (TIAs) are generally used, which could significantly reduce the sensitivity of the receiver and degrade the system performance for low-power and long-distance transmissions. However, the SPAD detector does not require a TIA and thus the output signal is not distorted by thermal noise, resulting in improved system performance [79].

Solar cell: Due to the increased efficiency, solar cells have been widely applied in our daily life, such as solar-powered calculators, solar phone chargers, solar power arrays on space satellites, and solar-powered street lights [80]. Besides energy harvesting, solar cells have also been applied in white LEDs based VLC systems for simultaneous reception of solar power and VLC signals [81]. A solar panel based VLC receiver was demonstrated in [82], without the need of a power supply, and achieving a data rate of 11.84 Mb/s. In [83], a self-reverse-biased solar panel optical receiver was proposed to improve the communication and energy harvesting performance. In [84], a nano-plasmonic thin-film solar cell (TFSC) based receiver was designed for VLC systems. Although simultaneous energy harvesting and VLC can be obtained by using a solar cell based receiver, the achievable data rate is very limited.

Image sensor/camera: CMOS image sensors have gained popularity in recent years because of advances in multi-functionalization, low manufacturing costs, and low power consumption.

A high-speed image sensor consists of a PD array typically organized in an orthogonal grid [85], which has been widely applied in various automotive applications [86–88]. Moreover, low-speed image sensors embedded in cameras have also been adopted as receivers in VLC systems [89]. In camera based VLC, also named optical camera communication (OCC), two main methods have been proposed for signal detection: one is based on the rolling shutter effect of the CMOS sensor of the camera [90] and the other is based on the undersampling technique [91]. Nevertheless, the achievable data rate of OCC systems is quite low which limits its practical applications.

2.2 MIMO-VLC

In an indoor environment, multiple LEDs are commonly mounted in the ceiling for sufficient indoor illumination. By exploiting the existing multiple LEDs, MIMO transmission is a very natural and effective way to increase the capacity of VLC systems [32].

2.2.1 Transmission schemes

In typical indoor MIMO-VLC systems, there are mainly three transmission schemes including repetition coding (RC), spatial multiplexing (SMP) and spatial modulation (SM).

Repetition coding (RC): RC is the simplest MIMO transmission scheme where all the LEDs in the VLC system simultaneously transmit the same signal [92]. It has been shown that RC can achieve good performance in free-space optical (FSO) communication systems due to transmit diversity [93]. However, the multiplexing gain of RC based MIMO-VLC systems is quite limited.

Spatial multiplexing (SMP): In SMP, different signals are transmitted by different LEDs and hence multiple parallel channels can be created in SMP based MIMO-VLC systems [32]. The performance of SMP is greatly limited by the inter-channel-interference, since each receiver in the corresponding channel not only receives the desired signal but also the interference signals from the other channels [94]. So far, many techniques have been proposed to mitigate the inter-channel-interference in SMP based MIMO-VLC systems, such as precoding [95–97], power imbalance between the LEDs or link blockage [92], improved receiver design [98, 99], and so on. Compared with RC, SMP can achieve much high multiplexing gain in white LEDs based MIMO-VLC systems.

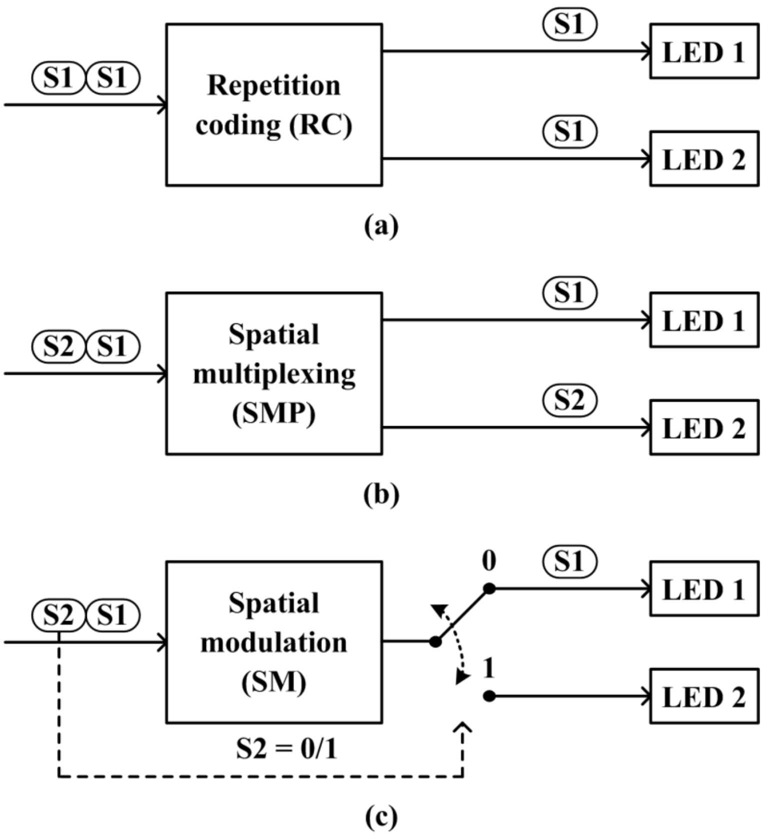

Figure 2.4. Illustration of three MIMO transmission schemes (a) RC, (b) SMP and (c) SM in a 2×2 MIMO-VLC system [33].

Spatial modulation (SM): SM is a technique that combines MIMO and digital modulation, where only one transmitter is active and transmits signal at any point of time [100]. In SM, the conventional signal constellation diagram is extended to an additional dimension, namely the spatial dimension, which can be utilized to transmit additional bits [101]. Since the data is encoded in both spatial and signal domains, SM achieves a relatively high multiplexing gain. Moreover, since only one LED is activated at any symbol duration, SM completely avoids inter-channel interference and hence has lower complexity compared with SMP [102].

Fig. 2.4 illustrates the principles of RC, SMP and SM in a 2×2 MIMO-VLC system [33]. A performance comparison of the above MIMO transmission schemes can be found in [92].

2.2.2 MIMO receivers

Generally, there are two types of optical receivers that can be used in white LEDs based VLC systems, i.e., non-imaging receiver (NImR) and imaging receiver (ImR) [32].

Non-imaging receiver (NImR): NImR consists of an array of independent PDs, each of which has an individual optical concentrator [103]. MIMO-VLC systems using NImR usually suffer from high channel correlation, leading to very significant inter-channel interference, which is mainly caused by the LOS transmission characteristic of VLC and the small spatial separation of PDs in typical NImRs [94, 96]. In order to reduce channel correlation and improve the performance of MIMO-VLC systems, non-imaging angle diversity receivers (NImADRs) have been proposed where tilted PDs instead of vertically oriented PDs are utilized to achieve angle diversity [104–106]. Nevertheless, NImADRs can only reduce the channel correlation of MIMO-VLC systems to a certain extent and the capacity improvement is still limited.

Imaging receiver (ImR): ImR is composed of an imaging lens, an optical filter and a detector array, where the imaging lens is employed to project the incident light from the LEDs onto the detector array while the optical filter is used to attenuate the unwanted ambient light [46]. Since ImRs can effectively decorrelate the multiplexed channels in MIMO-VLC systems and hence eliminate inter-channel interference, the capacity of MIMO-VLC systems using ImR can be fully exploited [107–109]. Nevertheless, the FOV of an ImR is relatively small which limits the mobility of the receiver.

2.3 Applications of VLC

Nowadays, LEDs have been widely deployed for illumination in indoor environments due to its high energy efficiency and cost-effectiveness [5]. It is predicted that LEDs will gradually replace conventional incandescent and fluorescent lamps for illumination and dominate the illumination market by 2020 [110]. Considering that the LEDs are always turned on in many indoor environments, the most promising application of LEDs is indoor high-speed wireless communication [16]. It has been reported that the achievable data rate of indoor VLC systems can reach up to multiple Gb/s, which is much higher than conventional RF based systems such as Wi-Fi [24, 31, 67, 75]. Besides high-speed wireless communication, white LEDs based VLC also has many other emerging applications, which are discussed as follows.

Vehicular communication: Vehicular communication using VLC has attracted great attention in recent years. The applications of VLC for vehicular communication can be divided into two categories: one is vehicle-to-infrastructure (V2I) communication and the other is vehicle-to-vehicle (V2V) communication [2]. In V2I systems, the vehicle is connected with traffic related infrastructure such as traffic light and streetlight [111–113]. In V2V systems, the headlights and taillights of a vehicle are used as transmitters and PD or image sensor are used as receivers to connect different vehicles [86–88, 114, 115]. Fig. 2.5 illustrates the application of VLC in V2I and V2V systems.

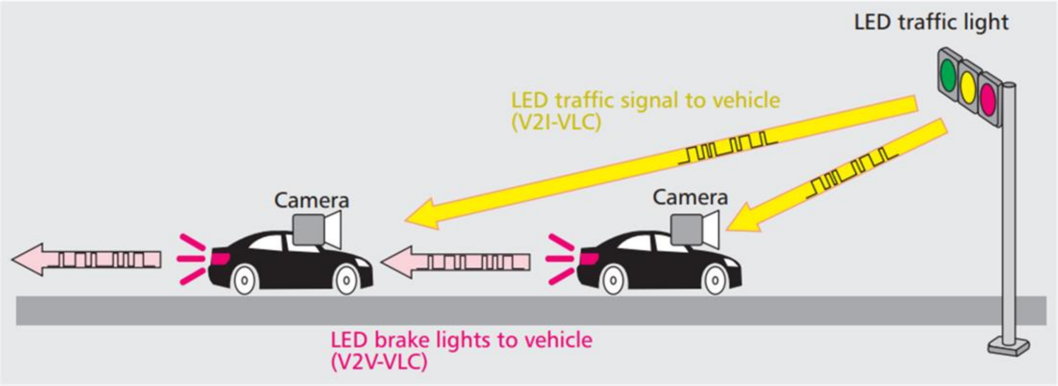

Figure 2.5. Illustration of VLC based V2I and V2V systems [86].

Underwater communication: Due to the growing need for underwater observation and subsea monitoring, underwater communication has stimulated considerable interest recently [116]. In underwater environments, conventional RF signals cannot be used for communication due to high attenuation [117]. Acoustic (sonar) waves have relatively low attenuation in seawater, but the data rate is quite limited [118]. Optical wireless communication, including VLC, has revealed great potential for high-speed underwater communication [116–120]. For VLC based underwater communication systems, visual confirmation becomes possible in relatively clear underwater environments [117]. Fig. 2.6 illustrates the concept of VLC based underwater communication.

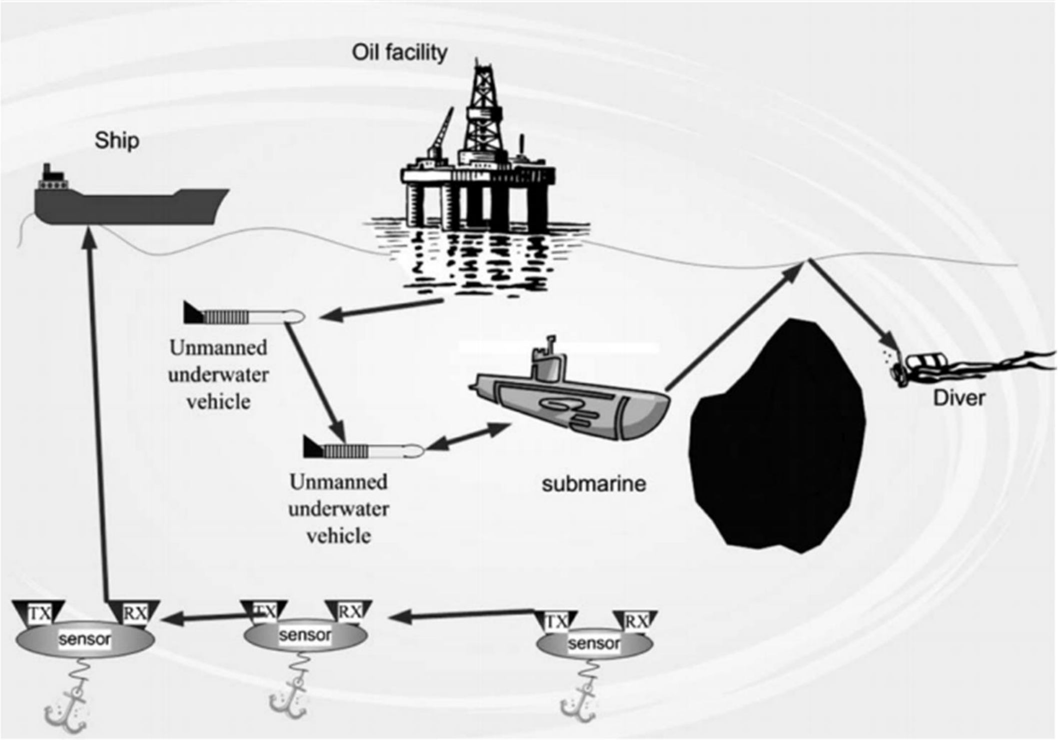

Figure 2.6. Illustration of VLC based underwater communication [116].

EMI-sensitive communication: Since visible light is used as the media for signal transmission in white LEDs based VLC systems, there is no RFI/EMI and hence VLC can be a promising technique for high-speed wireless communication in many EMI-sensitive environments such as aircraft cabins, hospitals, underground mines, spaceships, etc. [54, 121]. Fig. 2.7 shows a reading lamp based VLC system deployed in an in-flight environment.

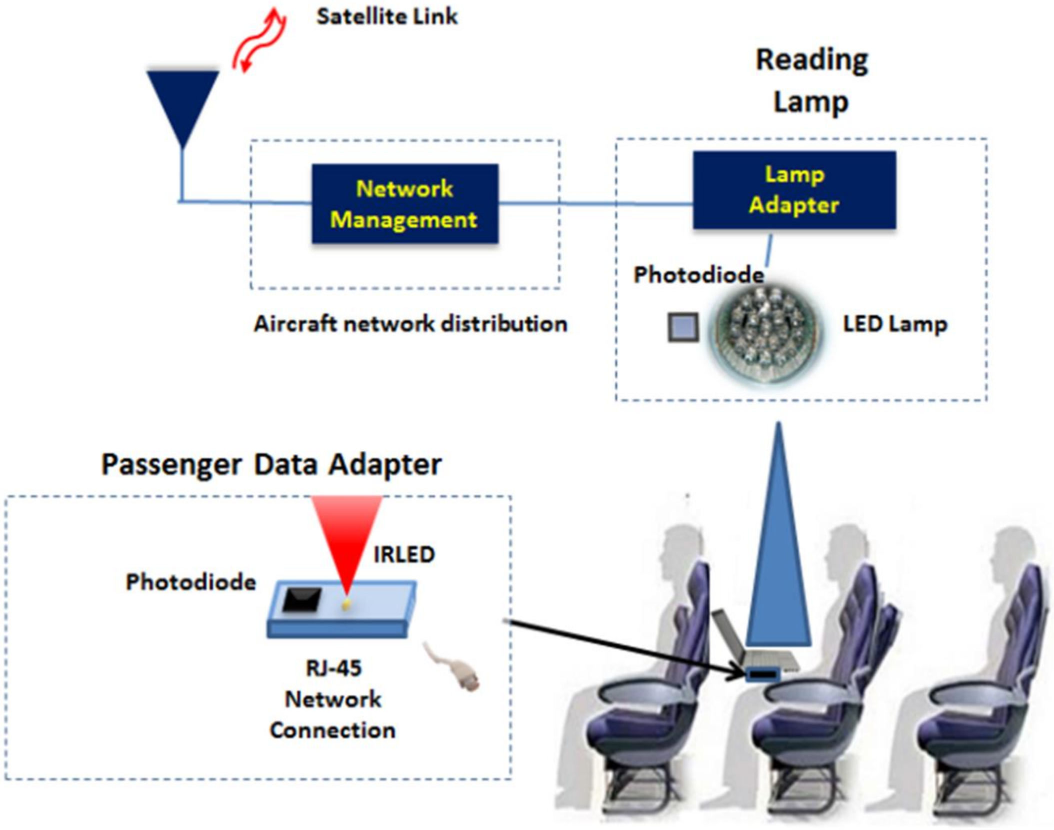

Figure 2.7. Illustration of VLC based in-flight communication [121].

Indoor positioning: Positioning, also known as localization, is the process of determining the spatial position of an object or person. Global positioning system (GPS) is most widely used positioning technique in our daily life, but it is not suitable in indoor environments [122]. Due to the wide deployment of white LEDs for illumination, it is a unique opportunity to develop a flexible, accurate and ubiquitous indoor positioning system by exploiting the existing white LEDs [122–124]. It is expected that the market for mobile indoor positioning in the retail sector will reach $5 billion by 2018 [8, 125]. In practical implementations, communication and positioning can be simultaneously supported in an integrated visible light communication and positioning (VLCP) system. Fig. 2.8 shows the concept of VLC based indoor positioning.

Figure 2.8. Illustration of VLC based indoor positioning [8].

(a) 2 LEDs (b) 3 LEDs (c) 4 LEDs (d) 5 LEDs (e) Setup w/ PD

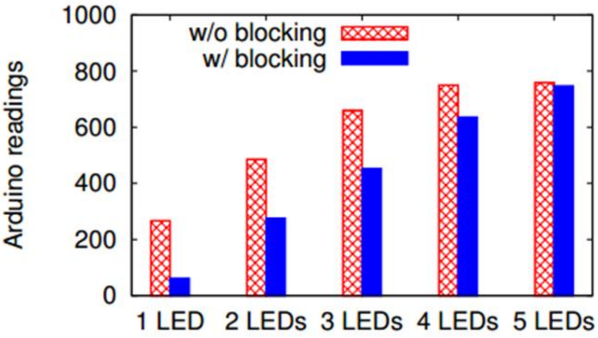

(f) Sensed light intensity

Figure 2.9. Illustration of VLC based human sensing [130].

Ranging, detection, and sensing: Besides conventional applications such as communication and positioning, VLC can also be applied in many other scenarios such as ranging, detection and sensing [85]. In [126, 127], white LEDs based VLC has been considered for range estimation by exploiting the phase information. In [128], VLC is used for efficient road surface detection based on the diffuse and specular reflections from the road surface. Motion detection using VLC was further demonstrated in [129], where motion was detected by observing the pattern created by intentional obstruction of a VLC link. In [130, 131], VLC based human and occupancy sensing were demonstrated by using shadows created by the human body and variances in diffuse reflection, respectively. Fig. 2.9 illustrates the principle of human sensing based on VLC.

2.4 Summary

In this chapter, a brief review of white LEDs based VLC systems has been presented. Since the light emitted by LEDs is naturally incoherent, IM/DD is generally adopted in white LEDs based VLC systems. Several modulation and detection techniques, which have been widely applied in VLC systems, have been briefly reviewed and compared. Moreover, MIMO-VLC technique has been discussed in terms of transmission schemes and receivers. Finally, a brief introduction on the various emerging practical applications of VLC in our daily life has also been provided.

Chapter 3 Non-Hermitian Symmetry OFDM for MIMO-VLC

3.1 Introduction

It has been discussed in Chapter 2 that OFDM using high-order QAM modulation is widely used capacity-enhancement technique in indoor VLC systems. Due to the IM/DD nature of white LEDs based VLC systems, Hermitian symmetry (HS) is usually imposed before performing IFFT so as to generate LED-compatible real-valued OFDM signals. HS-based OFDM (HS-OFDM) with a DC bias is also known as DCO-OFDM [132]. Many modified HS-OFDM schemes have been reported in the literature for spectral efficiency improvement and/or peak-to-average power ratio (PAPR) reduction, such as ACO-OFDM [133], unipolar OFDM [134], enhanced unipolar OFDM [135], spectral and energy efficient OFDM (SEE-OFDM) [136], asymmetrically and symmetrically clipped optical OFDM (ASCO-OFDM) [137], and so on. However, imposing HS doubles the sizes of IFFT and FFT. In recent years, a few approaches have been proposed to circumvent the HS constraint of OFDM for IM/DD optical systems. A real-valued OFDM scheme based on the fast Hartley transform (FHT) was reported in [138] where Fourier processing was replaced by the real processing of Hartley transform, but only real-valued constellations can be used. Based on a polar representation of complex symbols, polar OFDM was proposed, which can offer a doubled spectral efficiency as ACO-OFDM [139]. Moreover, the idea of first extracting the real and imaginary parts of a complex-valued OFDM signal and then separately transmitting them via multiple consecutive symbols was reported in [140, 141]. However, using multiple symbols to transmit one OFDM frame greatly reduces the capacity. In [30], it was mentioned that the real and imaginary parts can be separately transmitted via two chips, i.e. two different wavelengths, of a RGB-LED via the same optical link. Since RGB-LEDs are relatively more expensive than phosphor-based LEDs, the use of RGB-LEDs would increase the cost of VLC systems.

In practical indoor environments, multiple LEDs are commonly mounted in the ceiling to provide sufficient illumination. Hence, MIMO is a natural and effective way to increase the capacity of indoor VLC systems [32]. The above-mentioned OFDM schemes can be directly used in indoor MIMO-VLC systems. In this chapter, a novel non-HS OFDM (NHS-OFDM) modulation scheme is proposed for communication coverage improvement of indoor MIMO-VLC systems [142]. By transmitting the real and imaginary parts of a complex-valued OFDM signal through a pair of white LEDs, NHS-OFDM can circumvent the constraint of HS. The performance of an indoor 2×2 MIMO-VLC system using conventional HS-OFDM and the proposed NHS-OFDM is evaluated, where NImR and ImR are both considered. Analytical results show that the system using NHS-OFDM achieves superior bit error rate (BER) performance than that using HS-OFDM, with lower or nearly the same computational complexity. Furthermore, the superior BER performance of NHS-OFDM based MIMO-VLC is verified by proof-of-concept experiments and the experimental results demonstrate that, in an indoor 400 Mb/s 2×2 MIMO-VLC system using an ImR, NHS-OFDM improves the communication coverage area of the system by about 30% compared with conventional HS-OFDM for a target BER of 3.8×10^{-3}. Finally, the impact of LED pairing on the performance of general NHS-OFDM based MIMO-VLC systems is also analyzed

The rest of the chapter is organized as follows. In Section 3.2, the principle of the proposed NHS-OFDM based MIMO-VLC system is first introduced. In Section 3.3, the analytical BER expressions of a 2×2 MIMO-VLC system using conventional HS-OFDM and the proposed NHS-OFDM are then derived. Numerical and experimental results are presented in Section 3.4, and the impact of LED pairing on the performance of NHS-OFDM based MIMO-VLC systems is analyzed in Section 3.5. Finally, the conclusion is given in Section 3.6. The content of this chapter is related to the author’s work shown in [142–145].

3.2 Principle of NHS-OFDM based MIMO-VLC

This section introduces the principle of NHS-OFDM based MIMO-VLC and compares it with that employing conventional HS-OFDM [142]. For simplicity and without loss of generality, an indoor 2×2 MIMO-VLC system is considered.

Figs. 3.1(a) and (b) illustrate the block diagrams of an indoor 2×2 MIMO-VLC system using conventional HS-OFDM and the proposed NHS-OFDM, respectively. As shown in Fig. 3.1(a), two pairs of HS-OFDM transmitters and receivers are needed. The serial input data are first split into two parallel data streams and each stream is fed into a HS-OFDM transmitter. After serial-to-parallel (S/P) conversion, the parallel data are mapped to QAM symbols.

In order to generate a real-valued OFDM signal, HS is imposed before the N-point IFFT. A cyclic prefix (CP) is added and the resultant parallel signal is parallel-to-serial (P/S) converted. Then, a training sequence (TS) is added. After digital-to-analog (D/A) conversion and adding a DC bias, two unipolar analog signals $x_1(t)$ and $x_2(t)$ can be obtained at the outputs of two HS-OFDM transmitters, which are then separately modulated onto the intensities of two white LEDs.

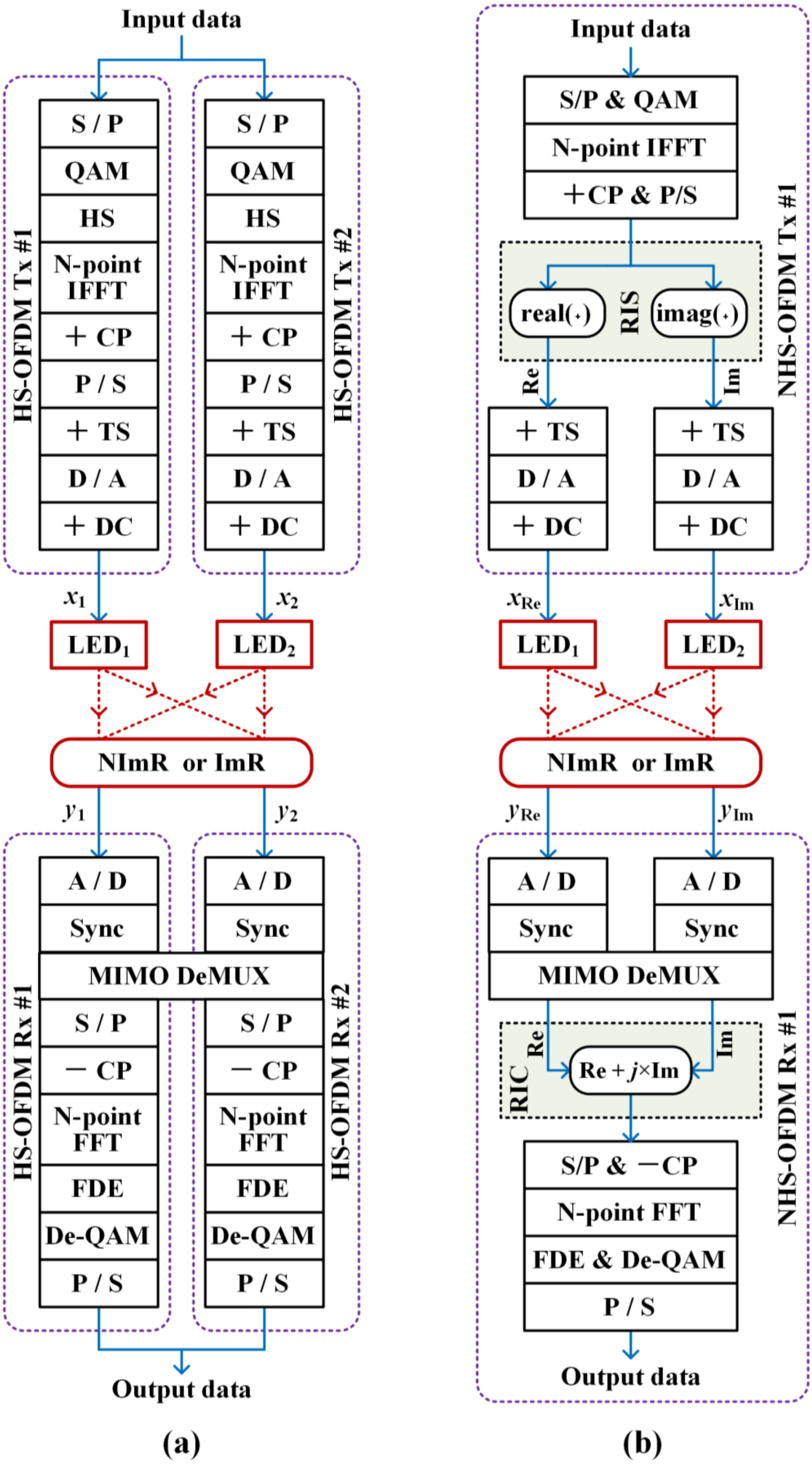

Figure 3.1. Block diagrams of a 2×2 MIMO-VLC system using (a) conventional HS-OFDM and (b) the proposed NHS-OFDM.

After being transmitted over the indoor free-space channel, the light is detected by a receiver, which can be a NImR or an ImR. Two output signals $y_1(t)$ and $y_2(t)$ are obtained and separately demodulated in two HS-OFDM receivers. In each HS-OFDM receiver, the received analog signal is analog-to-digital (A/D) converted. By exploiting the TS, time synchronization is performed. Based on the pre-estimated channel information, MIMO de-multiplexing (De-MUX) is executed. After performing S/P conversion, CP removal, N-point FFT, frequency domain equalization (FDE), QAM demapping and P/S conversion, an output data stream is generated. The final output data is obtained by combining the two parallel output data streams together. The QAM constellation can be obtained by using the received frequency domain QAM signal.

As shown in Fig. 3.1(b), only one pair of NHS-OFDM transmitter and receiver is needed in the 2×2 MIMO-VLC system using the newly proposed NHS-OFDM. In the NHS-OFDM transmitter, no HS is imposed before performing IFFT, instead a real-and-imaginary separator (RIS) is utilized to separate the real and imaginary parts of the complex-valued OFDM signal. The intensities of two LEDs are then modulated by the real and imaginary signals $x_{\mathrm{Re}}(t)$ and $x_{\mathrm{Im}}(t)$, respectively.

Since transmission distances of the real and imaginary signals might be different, the received real and imaginary signals $y_{\mathrm{Re}}(t)$ and $y_{\mathrm{Im}}(t)$ might have different phases and different electrical powers. In order to eliminate the phase imbalance between the received real and imaginary signals, the real and imaginary signals are separately synchronized by using the corresponding TSs after A/D conversion. Moreover, the electrical powers of the received real and imaginary signals are also balanced and the power balancing can be easily achieved via usual MIMO De-MUX. The phase and power balanced real and imaginary signals are then combined together in a real-and-imaginary combiner (RIC) to reconstruct the complex-valued signal.

It should be noted that the same time synchronization and MIMO De-MUX procedures are required in conventional HS-OFDM based MIMO-VLC systems. Therefore, the operations for balancing phase and power do not add any additional requirements in NHS-OFDM based MIMO-VLC systems.

It is also noteworthy that the proposed NHS-OFDM scheme can only be used in MIMO-VLC systems with one or more pairs of LEDs, whereas HS-OFDM can be used in both SISO-VLC and MIMO-VLC systems. It can be seen that HS-OFDM, which is also known as DCO-OFDM [132], exploits HS to generate a real-valued signal and the DC bias is added. Since DC bias are also required in NHS-OFDM, NHS-OFDM can be considered as a modified DCO-OFDM scheme for MIMO-VLC, which removes the constraint of HS.

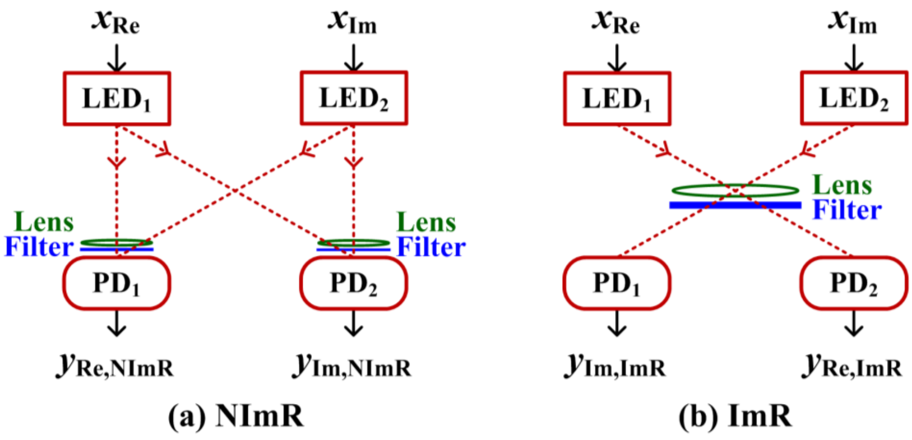

Figure 3.2. Schematic diagrams of a NHS-OFDM based 2×2 MIMO-VLC system using (a) a NImR and (b) an ImR.

Generally, two different types of receivers can be used in MIMO-VLC systems. Figs. 3.2(a) and (b) show the schematic diagrams of a 2×2 MIMO-VLC system using a NImR and an ImR, respectively. For the 2×2 MIMO-VLC system using a NImR, the channel matrix is given by

$$\mathbf{H}_{\mathrm{NImR}} = \begin{bmatrix} h_{11} & h_{12} \\ h_{21} & h_{22} \end{bmatrix}, \tag{3.1}$$

where h_{rt} $(t, r = 1, 2)$ is the optical channel DC gain between the t-th LED and the r-th PD. The definition of h_{rt} can be found in Eq. (2.7). However, when an ImR is employed, the ICI can be substantially eliminated [109] and hence the channel matrix becomes a diagonal matrix

$$\mathbf{H}_{\mathrm{ImR}} = \begin{bmatrix} 0 & h_{12} \\ h_{21} & 0 \end{bmatrix}. \tag{3.2}$$

3.3 BER analysis

Analytical BER expressions of the 2×2 MIMO-VLC system using conventional HS-OFDM and the proposed NHS-OFDM are derived and presented in this section.

3.3.1 BER of MIMO-VLC using HS-OFDM

Assuming that the two LEDs have the same average transmitted optical power P_0 and the same modulation index ξ, and the two PDs have the same responsivity R, the received signal vector $\mathbf{y} = [y_1\ y_2]^T$ in the indoor 2×2 MIMO-VLC system using conventional HS-OFDM is represented by [144]

$$\mathbf{y} = RP_0\xi\mathbf{H}\mathbf{x} + \mathbf{n}, \tag{3.3}$$

where $\mathbf{x}=[x_1\ x_2]^T$ is the transmitted signal vector, **H** is the channel matrix and $\mathbf{n}=[n_1\ n_2]^T$ is the additive noise vector. **H** is given by Eq. (3.1) when a NImR is used and **H** becomes Eq. (3.2) when an ImR is used. Both $n_1(t)$ and $n_2(t)$ can be modeled as real-valued AWGNs, each consisting of shot and thermal noises [146].

In order to recover data from the received electrical signal, MIMO De-MUX is required. So far, many techniques have been proposed, of which zero-forcing (ZF) using basic channel inversion is adopted here due to its low complexity [94]. After ZF based MIMO De-MUX and normalization, the estimate of **x** is obtained by:

$$\tilde{\mathbf{x}}=\frac{1}{RP_0\xi}\mathbf{H}^{-1}\mathbf{y}=\mathbf{x}+\frac{1}{RP_0\xi}\mathbf{H}^{-1}\mathbf{n}. \tag{3.4}$$

Based on Eq. (3.4), the SNRs of two received HS-OFDM signals using a NImR can be respectively given by

$$\begin{cases}\mathrm{SNR}_{\mathrm{HS1}}^{\mathrm{NImR}}=(RP_0\xi)^2\dfrac{(h_{11}h_{22}-h_{12}h_{21})^2}{h_{22}^2\sigma_{n_1}^2+h_{12}^2\sigma_{n_2}^2}\\ \mathrm{SNR}_{\mathrm{HS2}}^{\mathrm{NImR}}=(RP_0\xi)^2\dfrac{(h_{11}h_{22}-h_{12}h_{21})^2}{h_{21}^2\sigma_{n_1}^2+h_{11}^2\sigma_{n_2}^2}\end{cases}, \tag{3.5}$$

where $\sigma_{n_1}^2$ and $\sigma_{n_2}^2$ are the variances of $n_1(t)$ and $n_2(t)$, respectively. However, when an ImR is employed, h_{11} and h_{22} become zero and hence the SNRs are given by

$$\begin{cases}\mathrm{SNR}_{\mathrm{HS1}}^{\mathrm{ImR}}=(RP_0\xi)^2\dfrac{h_{21}^2}{\sigma_{n_2}^2}\\ \mathrm{SNR}_{\mathrm{HS2}}^{\mathrm{ImR}}=(RP_0\xi)^2\dfrac{h_{12}^2}{\sigma_{n_1}^2}\end{cases}. \tag{3.6}$$

The BER of an OFDM signal using $I\times J$ rectangular QAM mapping over an AWGN channel is approximated by [147]

$$\mathrm{BER}=\frac{2}{\log_2(IJ)}\left(\frac{I-1}{I}+\frac{J-1}{J}\right)\mathrm{Q}\left(\sqrt{\frac{6\mathrm{SNR}}{I^2+J^2-2}}\right), \tag{3.7}$$

where $\mathrm{Q}(\cdot)$ is the Q-function. Therefore, the BERs of the two HS-OFDM signals, $\mathrm{BER}_{\mathrm{HS1}}$ and $\mathrm{BER}_{\mathrm{HS2}}$, employing a NImR and an ImR can be obtained by substituting Eq. (3.5) and Eq. (3.6) into Eq. (3.7), respectively. The average BER of the 2×2 MIMO-VLC system using HS-OFDM is given by Eq. (3.8) on the top of the next page.

$$\mathrm{BER}_{\mathrm{HS}} = \frac{\mathrm{BER}_{\mathrm{HS1}} + \mathrm{BER}_{\mathrm{HS2}}}{2}. \tag{3.8}$$

3.3.2 BER of MIMO-VLC using NHS-OFDM

When NHS-OFDM is used in the 2×2 MIMO-VLC system, the transmitted signal vector is given by $\mathbf{x}' = [x_{\mathrm{Re}}\ x_{\mathrm{Im}}]^T$, which corresponds to a complex-valued NHS-OFDM signal expressed by $x_{\mathrm{NHS}}(t) = x_{\mathrm{Re}}(t) + jx_{\mathrm{Im}}(t)$. After being transmitted over the free-space channel, the received signal vector $\mathbf{y}' = [y_{\mathrm{Re}}\ y_{\mathrm{Im}}]^T$ is represented by

$$\mathbf{y}' = RP_0\xi\mathbf{H}\mathbf{x}' + \mathbf{n}', \tag{3.9}$$

where $\mathbf{n}' = [n_{\mathrm{Re}}\ n_{\mathrm{Im}}]^T$ is the additive noise vector. Similarly, ZF based MIMO De-MUX is performed and hence the estimated signal $\tilde{\mathbf{x}}' = [\tilde{x}_{\mathrm{Re}}\ \tilde{x}_{\mathrm{Im}}]^T$ is obtained by

$$\tilde{\mathbf{x}}' = \frac{1}{RP_0\xi}\mathbf{H}^{-1}\mathbf{y}' = \mathbf{x}' + \frac{1}{RP_0\xi}\mathbf{H}^{-1}\mathbf{n}'. \tag{3.10}$$

The powers of the real and imaginary parts are automatically balanced by performing MIMO De-MUX, and the complex-valued NHS-OFDM signal can be reconstructed by combining $\tilde{x}_{\mathrm{Re}}$ and $\tilde{x}_{\mathrm{Im}}$ together

$$\begin{aligned} \tilde{x}_{\mathrm{NHS}}(t) &= \tilde{x}_{\mathrm{Re}}(t) + j\tilde{x}_{\mathrm{Im}}(t) \\ &= x_{\mathrm{NHS}}(t) + \frac{(h_{22} - jh_{21})\, n_{\mathrm{Re}}(t) + (jh_{11} - h_{12})\, n_{\mathrm{Im}}(t)}{RP_0\xi(h_{11}h_{22} - h_{12}h_{21})}. \end{aligned} \tag{3.11}$$

Based on Eq. (3.11), the SNR of the received NHS-OFDM signal using a NImR is given by

$$\mathrm{SNR}_{\mathrm{NHS}}^{\mathrm{NImR}} = (RP_0\xi)^2 \frac{2(h_{11}h_{22} - h_{12}h_{21})^2}{(h_{21}^2 + h_{22}^2)\sigma_{n_{\mathrm{Re}}}^2 + (h_{11}^2 + h_{12}^2)\sigma_{n_{\mathrm{Im}}}^2}, \tag{3.12}$$

where $\sigma_{n_{\mathrm{Re}}}^2$ and $\sigma_{n_{\mathrm{Im}}}^2$ are the variances of $n_{\mathrm{Re}}(t)$ and $n_{\mathrm{Im}}(t)$, respectively. When an ImR is used, the SNR becomes

$$\mathrm{SNR}_{\mathrm{NHS}}^{\mathrm{ImR}} = (RP_0\xi)^2 \frac{2(h_{12}h_{21})^2}{h_{21}^2\sigma_{n_{\mathrm{Re}}}^2 + h_{12}^2\sigma_{n_{\mathrm{Im}}}^2}. \tag{3.13}$$

Substituting Eq. (3.12) and Eq. (3.13) into Eq. (3.7) yields the BER of the NHS-OFDM based indoor 2×2 MIMO-VLC system employing a NImR and an ImR, respectively.

3.4 Performance evaluation

In this section, the performance of a 2×2 MIMO-VLC system using conventional HS-OFDM and NHS-OFDM is numerically evaluated, based on the formulas derived in Section 3.3. It should be pointed out that the obtained analytical results are applicable to general MIMO-VLC systems using multiple pairs of LEDs.

Table 3.1. Key parameters of the 2×2 MIMO-VLC system

Parameter	**Value**
Room dimension	2m×2m×2.5m
Locations of two LEDs	(–0.5, 0, 2.5), (0.5, 0, 2.5)
Height of receiving plane	0.5 m
Transmitter semi-angle at half power	60°
Modulation index	0.3
Gain of optical filter	1
Gain of optical lens	1
Responsivity of PD	1 A/W

Table 3.1 lists the key parameters of the system setup. In this analysis, a 2×2 MIMO-VLC system in a 2m×2m×2.5m room is considered where two LEDs are mounted in the ceiling and the height of the receiving plane is 0.5 m. The semi-angle at half power of the LED is 60° and the modulation index is 0.3. The gains of the optical filter and the optical lens are both 1. The responsivity of the PD is 1 A/W.

3.4.1 BER performance

The SNR performance along the X direction with Y = 0 m is shown in Fig. 3.3(a), where an ImR is used. The average transmitted optical power of LED P_0 is 10 W, the modulation bandwidth of LED BW is 50 MHz and the active area of a PD, A_{PD}, is 10^{-5} m^2. As can be seen, the SNR values are the same for HS-OFDM and NHS-OFDM if and only if X = 0 m (i.e., the ImR is located at the center of the receiving plane). When the ImR is moved away from the center of the receiving plane, the SNRs of two HS-OFDM signals become different. For example, the SNRs of two HS-OFDM signals are 15.84 dB and 19.75 dB at X = 0.5 m, respectively, whereas the SNR of the NHS-OFDM signal is 17.37 dB. It can also be observed that the SNR of the NHS-OFDM signal is always in between the SNRs of the two HS-OFDM signals.

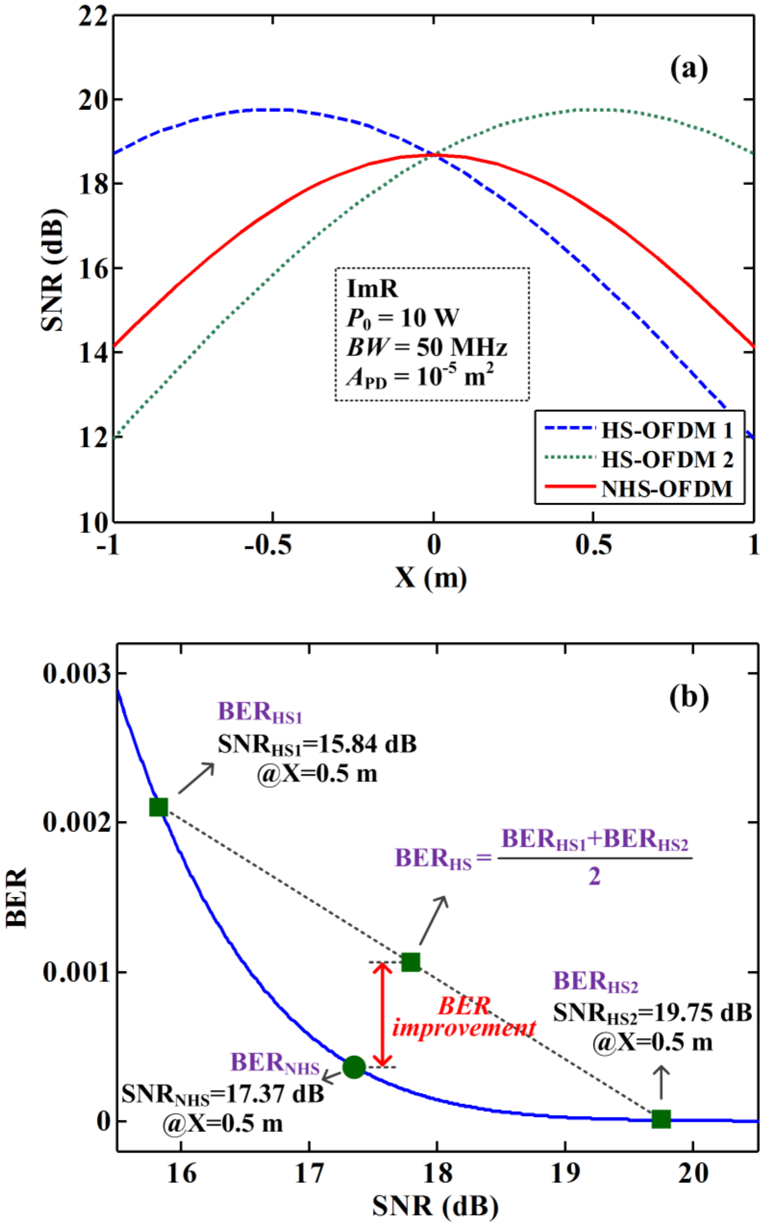

Figure 3.3. (a) SNR along the X direction with Y = 0 m employing an ImR, and (b) BER versus SNR for 16QAM-OFDM over an AWGN channel.

Fig. 3.3(b) shows the relationship between the BER and the SNR for a 4×4 rectangular QAM (16QAM) based OFDM signal over an AWGN channel. The BERs of two HS-OFDM signals are 2.1×10^{-3} and 5.2×10^{-6} at X = 0.5 m, respectively, and the average BER of the 2×2 MIMO-VLC system using HS-OFDM is 1.1×10^{-3}. In contrast, the BER of the system using NHS-OFDM at X = 0.5 m is 3.6×10^{-4}, which is a significant BER reduction. Figs. 3.3(a) and (b) explain why the 2×2 MIMO-VLC system using NHS-OFDM has better BER performance than the system using HS-OFDM. It can be generally concluded that NHS-OFDM can always achieve BER improvements over HS-OFDM as long as the two HS-OFDM signals have different SNRs. Fig. 3.3 shows the insight into the mechanism that makes the proposed NHS-OFDM advantageous in MIMO-VLC systems.

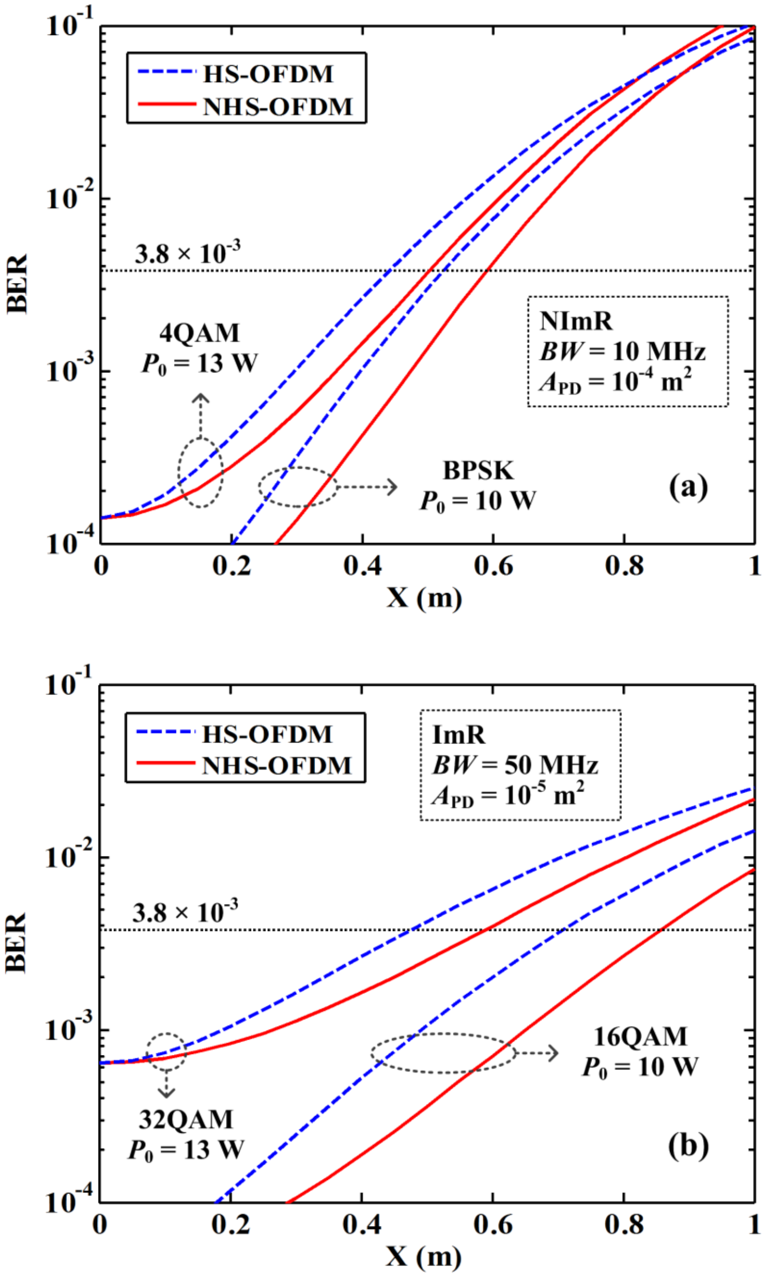

Figure 3.4. BER versus receiver position offset along the X direction with Y = 0 m for the 2×2 MIMO-VLC system employing (a) a NImR and (b) an ImR.

Figs. 3.4(a) and (b) show the BER versus the receiver position offset along the X direction with Y = 0 m for the 2×2 MIMO-VLC system employing a NImR and an ImR, respectively. When a NImR is employed, as shown in Fig. 3.4(a), the modulation bandwidth of LED *BW* is set at 10 MHz and the active area of PD A_{PD} is assumed to be 10^{-4} m^2. Due to the high ICI, two lower order constellations are considered. For a target BER of 3.8×10^{-3}, compared with the system using HS-OFDM, a relative larger receiver position offset can be achieved when using NHS-OFDM, for both binary phase shift keying (BPSK) with an average transmitted optical power of LED $P_0 = 10$ W and 4QAM with $P_0 = 13$ W. The same conclusion can also be drawn for the system employs an ImR, as shown in Fig. 3.4(b).

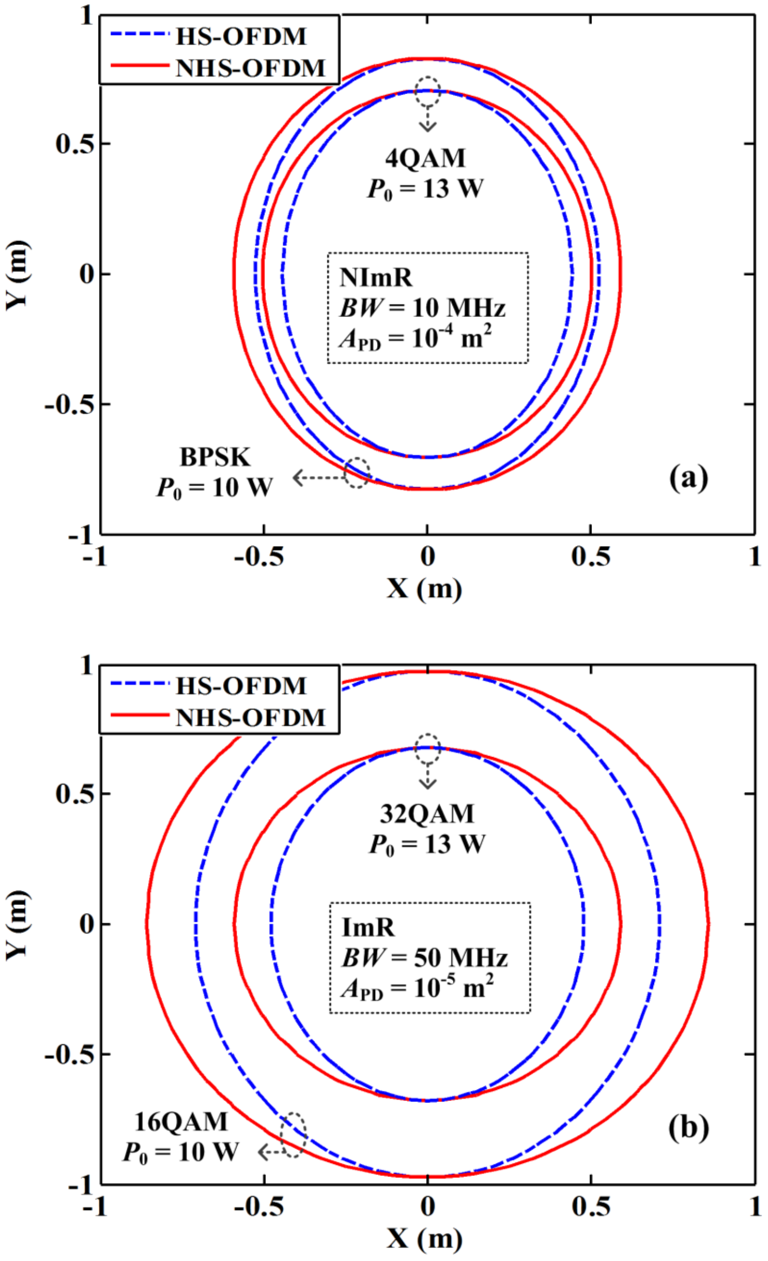

Figure 3.5. Communication coverage area of the 2×2 MIMO-VLC system for a target BER of 3.8×10^{-3} employing (a) NImR and (b) ImR.

Figs. 3.5(a) and (b) give the corresponding communication coverage areas of the 2×2 MIMO-VLC system employing a NImR and an ImR, respectively, for a target BER of 3.8×10^{-3}. The coverage contours can be approximated as ellipses and the coverage areas can be estimated by the areas of ellipses. The area of an ellipse is calculated by $\pi ab/4$ where a and b are the major and minor axes, respectively. As can be seen in Fig. 3.5(a), for BPSK with $P_0 = 10$ W, two ellipses have the same major axis of 1.7 m; while the minor axes associated with HS-OFDM and NHS-OFDM are 1.04 m and 1.2 m, respectively, indicating a coverage improvement of 15.4%. For 4QAM with $P_0 = 13$ W, a coverage area improvement of 13.6% is also achieved. Moreover, when an ImR is employed, as shown in Fig. 3.5(b), the coverage improvements for 16QAM with $P_0 = 10$ W and 32QAM with $P_0 = 13$ W are 21.4% and 20.8%, respectively. The above results show that the coverage improvement is only slightly reduced when the order of constellation is increased.

3.4.2 Transceiver complexity

In an indoor 2×2 MIMO-VLC system using HS-OFDM, as shown in Fig. 3.1(a), two pairs of HS-OFDM transmitters and receivers are required. However, only one pair of NHS-OFDM transmitter and receiver is required in the system using NHS-OFDM, as shown in Fig. 3.1(b). Since each HS-OFDM/NHS-OFDM transmitter (receiver) requires one N-point IFFT (FFT) module, the number of the required IFFT and FFT modules in the 2×2 MIMO-VLC system using NHS-OFDM is reduced by half, as compared with the system using HS-OFDM. Note that this conclusion holds for general indoor MIMO-VLC systems with one or multiple pairs of white LEDs.

Since the output (input) of the IFFT (FFT) module in HS-OFDM is of real value, Hermitian symmetric IFFT and real-valued FFT are used. In contrast, complex-valued IFFT and FFT are used in NHS-OFDM. As discussed in [148], the computational complexity of real-valued FFT is largely dependent on the algorithms utilized. For the algorithm that treats the real-valued input as a complex-valued input with an imaginary part of zero and then applies the complex-valued FFT, the computational complexity of one N-point real-valued FFT is exactly the same as that of one N-point complex-valued FFT [148]. For the algorithm which exploits the symmetries of real-valued FFT, i.e., the real part of the output is even symmetric and the imaginary part is odd symmetric, the computational complexity can be reduced by about a factor of 2 [148]. Likewise, Hermitian symmetric IFFT can be computed by reversing the computation of real-valued FFT [149].

Therefore, depending on the algorithms applied for the computation of Hermitian symmetric IFFT and real-valued FFT, the MIMO-VLC system using NHS-OFDM has lower or nearly the same computational complexity as the system using conventional HS-OFDM.

3.4.3 Experimental demonstration

In order to verify the performance of NHS-OFDM in indoor MIMO-VLC systems, a proof-of-concept experimental demonstration utilizing an ImR is performed. The setup of an indoor 2×2 MIMO-VLC system is illustrated in Fig. 3.6, where the transmission distance is 100 cm. Two off-the-shelf white LEDs (Luxeon Star) are used as optical transmitters, which have a 3-dB modulation bandwidth of about 2.5 MHz and the spacing between them is 20 cm. An ImR is configured as the optical receiver, which consists of an imaging lens, two blue filters (BFs) and two PDs (Thorlabs, PDA10A, 0.8 mm^2 active area and 180 MHz 3-dB bandwidth). The imaging lens is placed in front of the two PDs such that each of the two LEDs is precisely imaged onto a corresponding PD. Therefore, the separation between two PDs is not fixed which is dynamically adjusted with different receiver position offsets.

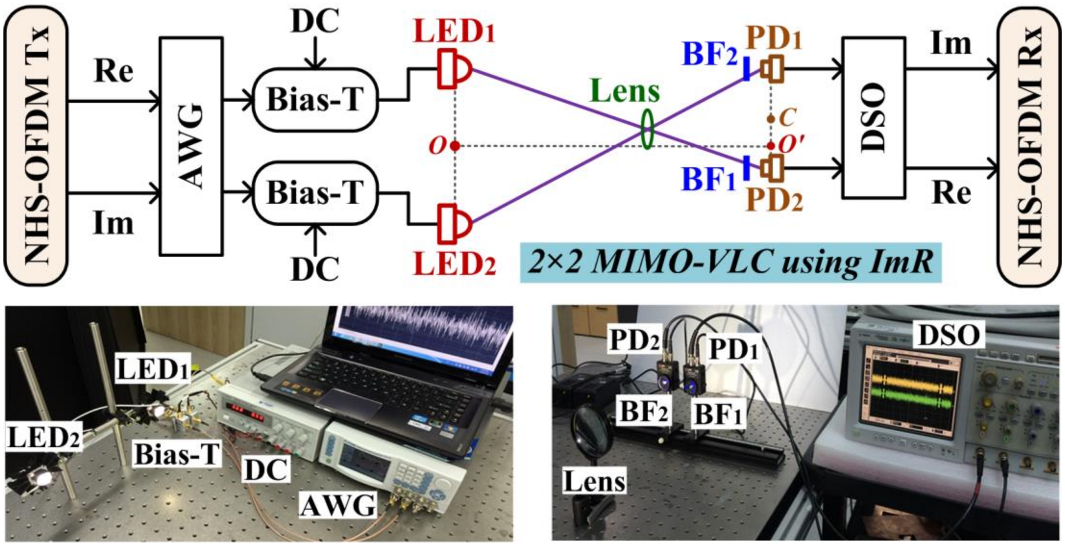

Figure 3.6. Experimental setup of the 2×2 MIMO-VLC system using ImR.

As illustrated in Fig. 3.6, *O* and *C* are the center points of the two LEDs and the two PDs, respectively, and *O'* is the foot of the perpendicular from *O* to the detector plane. Here, the receiver position offset is defined as the distance between *O'* and *C*, and the transmission distance as the distance between *O* and *O'*.

The digital NHS-OFDM signal is generated offline by MATLAB with an IFFT size of 256. In order to spectrally separate the baseband signal from the high frequency aliasing products generated by digital-to-analogue converters (DACs), subcarriers in the high frequency part are left unmodulated for oversampling, which is also referred to as zero padding [150]. As a result, 128 subcarriers in total are used for data transmission and no HS is imposed.

For fair performance comparison, two independent HS-OFDM signals are also generated with 256-point IFFT. Both oversampling and HS are performed and 64 subcarriers in total are used for data transmission in each HS-OFDM signal.

For both NHS-OFDM and HS-OFDM signals, 16QAM mapping is applied and the CP length is set to 8 which is 1/32 of the IFFT size. Moreover, a pseudo random binary sequence (PRBS) with the length of 20 is used as the TS for both time synchronization and channel matrix estimation, and a total of 200 OFDM payload symbols are followed for BER measurement. In order to extend the 3-dB modulation bandwidth of the LEDs, digital pre-FDE is performed and the detailed procedure can be found in [151]. The real and imaginary parts of the complex-valued NHS-OFDM signal are separately loaded to a multi-channel arbitrary waveform generator (AWG, Tabor WW2074) with a sampling rate of 200 MSa/s. Therefore, the bandwidth of the real and imaginary signals is 50 MHz and the raw data rate is 400 Mb/s.

The analog real and imaginary signals are separately superimposed onto 500-mA DC bias currents via two bias-Tees (Mini-Circuits, ZFBT-6GW+). The resultant signals are used to modulate the intensities of two LEDs. The luminous flux of each LED is about 63 lm. The light is detected by the ImR and the received signals are sampled by a digital storage oscilloscope (DSO, Agilent infiniium 54832B) with a sampling rate of 4 GSa/s. Subsequently, the output digital real and imaginary signals are processed offline. For comparison, two HS-OFDM signals achieving a total data rate of 400 Mb/s with the bandwidth of 50 MHz are transmitted through the same system.

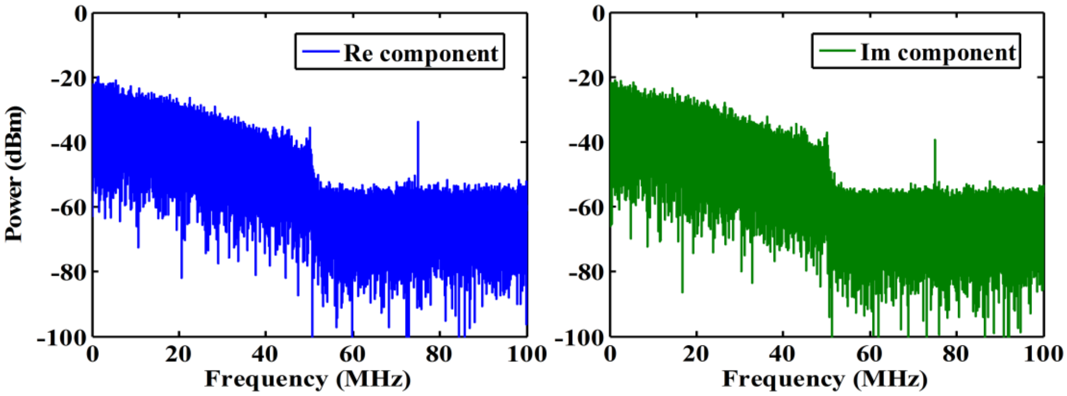

(a) without pre-FDE

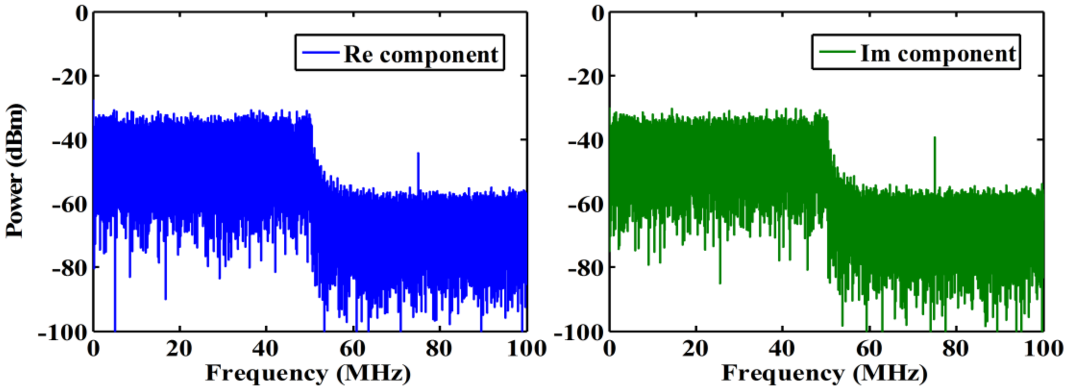

(b) with pre-FDE

Figure 3.7. Measured electrical spectra of the received real (Re) and imaginary (Im) parts of the NHS-OFDM signal (a) without pre-FDE and (b) with pre-FDE.

Fig. 3.7 compares the measured electrical spectra of the received real and imaginary parts of the NHS-OFDM signal. Without performing pre-FDE, as shown in Fig. 3.7(a), the electrical power of high frequency components is greatly attenuated and a power attenuation of ~ 20 dB is found for both the real and imaginary parts. However, the electrical spectra are significantly flattened with a power fluctuation less than 3 dB after performing pre-FDE, as shown in Fig. 3.7(b).

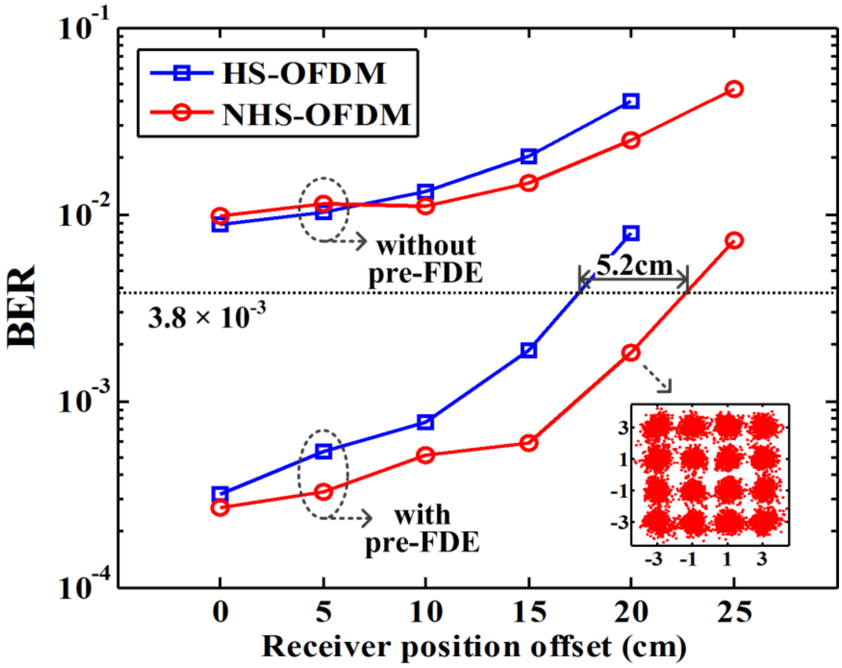

Figure 3.8. Measured BER versus receiver position offset with a distance of 100 cm.

Fig. 3.8 shows the measured BER performance as a function of the receiver position offset for a transmission distance of 100 cm. As can be seen, the BER is always greater than the 7% forward error correction (FEC) threshold of 3.8×10^{-3} when digital pre-FDE is not performed. However, the BER is substantially reduced after performing pre-FDE. It also can be seen that HS-OFDM and NHS-OFDM have nearly the same BER performance when the receiver position offset is 0 cm, while NHS-OFDM outperforms HS-OFDM as the receiver position offset increases. To reach a target BER of 3.8×10^{-3}, the maximum receiver position offsets by using HS-OFDM and NHS-OFDM are 17.4 cm and 22.6 cm, respectively. Therefore, NHS-OFDM achieves a 5.2 cm increased receiver position offset than HS-OFDM.

Since the communication coverage area of the 2×2 MIMO-VLC system can be approximated as an ellipse and the coverage areas can be estimated by the areas of ellipses. Two ellipses, associated with HS-OFDM and NHS-OFDM, have the same major axis but different minor axis. Moreover, the semi-minor axes (half of the minor axes) are given by the corresponding maximum receiver position offsets. As a result, NHS-OFDM improves the communication coverage area of the 2×2 MIMO-VLC system by about 30% for BER = 3.8×10^{-3}, compared with conventional HS-OFDM.

3.5 Impact of LED pairing

In the above analytical and experimental investigations, a simple two-channel MIMO-VLC system using NHS-OFDM with one pair of LEDs is considered. However, a general NHS-OFDM based MIMO-VLC system might have multiple pairs of LEDs and different LED pairing schemes can be adopted when applying NHS-OFDM. In this section, the impact of LED pairing on the performance of NHS-OFDM based MIMO-VLC systems with multiple pairs of LEDs is analyzed [145].

3.5.1 NHS-OFDM with LED pairing

It can be clearly seen from Fig. 3.1 that the signals are transmitted in pairs in NHS-OFDM based MIMO-VLC systems. Hence, it is necessary to divide the individual LEDs into pairs when there are multiple LEDs in the ceiling. The way that the LEDs are paired is associated with the layout of the LEDs in the ceiling. Several LED layouts have been studied, where square and hexagon are the mostly used LED layouts in indoor VLC systems [6]. Therefore, square and hexagonal LED layouts are considered in the following analysis.

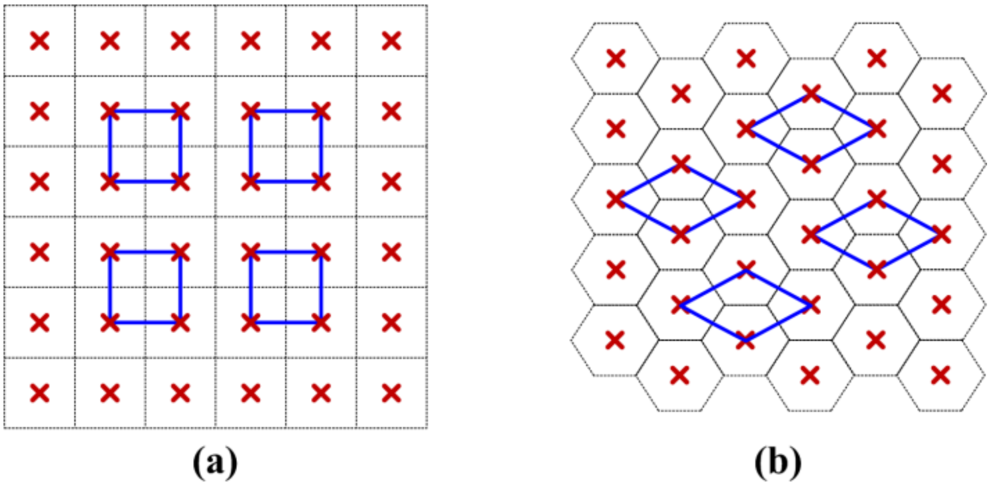

Figure 3.9. Cluster formation in (a) square and (b) hexagonal LED layout where red “×” indicates an LED.

Fig. 3.9 depicts the cluster formation in square and hexagonal LED layouts. It can be seen from Fig. 3.9(a) that the square layout can be divided into multiple square clusters and each cluster consists of four LEDs placed in a square.

Similarly, as shown in Fig. 3.9(b), the hexagonal layout can be divided into multiple rhombic clusters, each also consisting of four LEDs placed in a rhombus. It can be found that both the square and rhombic clusters consist of two pairs of LEDs.

Without loss of generality, an indoor four-channel MIMO-VLC system with four LEDs (two pairs of LEDs) can be adopted to investigate and analyze the impact of LED pairing on the performance of NHS-OFDM based MIMO-VLC systems

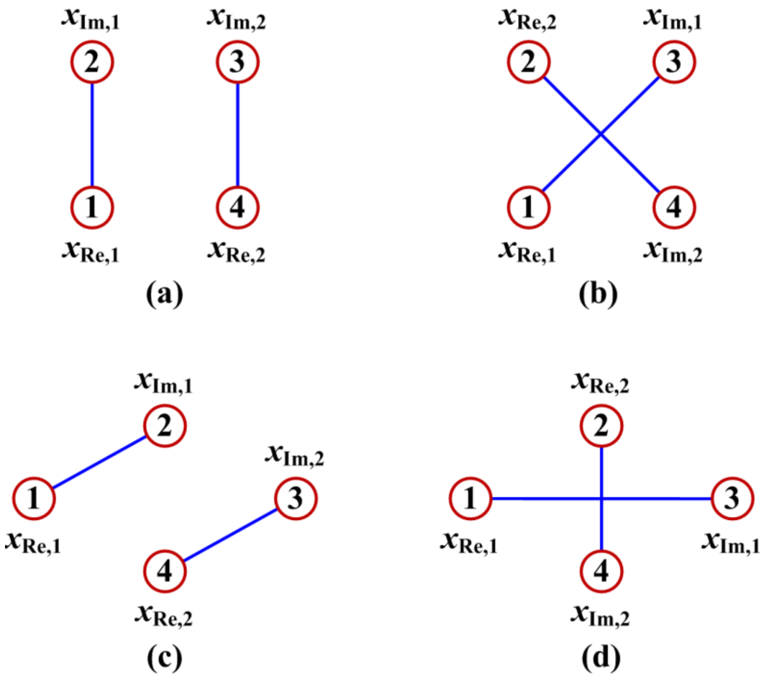

Figure 3.10. LED pairing: (a) parallel pairing in a square cluster, (b) cross pairing in a square cluster, (c) parallel pairing in a rhombic cluster, and (d) cross pairing in a rhombic cluster.

Fig. 3.10 shows the LED pairing schemes in square and rhombic clusters, which corresponds to an indoor four-channel MIMO-VLC system with totally two pairs of LEDs. Considering the geometric symmetry, the four LEDs in a square cluster can be paired in two ways: one is parallel pairing and the other is cross pairing. For parallel pairing, as shown in Fig. 3.10(a), two adjacent LEDs are paired together and two pairs of LEDs are parallel with each other in the square cluster. However, for cross pairing, two LEDs in the opposite corners are paired together and two pairs of LEDs cross with each other, as shown in Fig. 3.10(b). Similarly, it can be observed from Figs. 3.10(c) and (d) that four LEDs in a rhombic cluster can also be parallelly or crosswise paired.

3.5.2 BER analysis

The schematic diagram of a 2N-channel imaging MIMO-VLC system with N pairs of LEDs using NHS-OFDM is shown in Fig. 3.11. The serial input data of the system are first split into N parallel data streams and each data stream is then fed into a NHS-OFDM modulator where two outputs are generated. As can be seen, 2N LEDs are divided into N pairs and each pair of LEDs is driven by the two outputs of a NHS-OFDM modulator. After free-space propagation, an ImR is employed to detect the optical signal. The received N pairs of signals are fed into the respective NHS-OFDM demodulators. The output data can be obtained by combining together the N outputs of the NHS-OFDM demodulators. Although an even number of channels are considered in the imaging MIMO-VLC system due to the pairwise transmission nature of NHS-OFDM, the obtained results in the following can be easily generalized to an imaging MIMO-VLC system with an arbitrary number of channels. More specifically, when the system has an odd number of channels, a hybrid HS-OFDM/NHS-OFDM approach can be adopted, i.e., the paired LEDs transmit the NHS-OFDM signals while the remaining one LED which is not included in any LED pairs transmits the HS-OFDM signal.

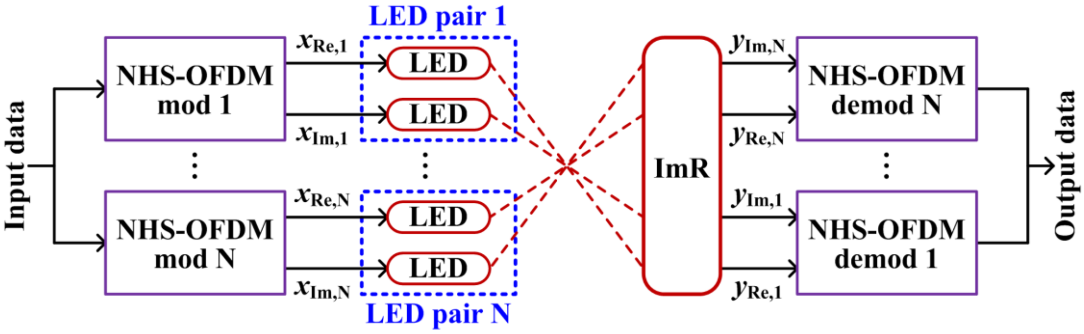

Figure 3.11. Schematic diagram of a 2N-channel imaging MIMO-VLC system with N pairs of LEDs using NHS-OFDM.

It is assumed that the 2N LEDs have the same average transmitted optical power P_0 and the same modulation index ξ, and meanwhile all the detectors in the detector array of the ImR have the same responsivity R. By dividing the total 2N individual LEDs into N pairs, the transmitted optical signal vector of the i-th pair of LEDs (LED $2i$–1 and LED $2i$) can be represented by

$$\mathbf{s}_i = P_0(1 + \xi \mathbf{x}_i), \tag{3.14}$$

where $\mathbf{x}_i = [x_{\mathrm{Re},i}\ x_{\mathrm{Im},i}]^T$ is the modulating signal vector. $x_{\mathrm{Re},i}(t)$ and $x_{\mathrm{Im},i}(t)$ are respectively the normalized real and imaginary parts of the complex-valued signal, i.e., $x_i(t) = x_{\mathrm{Re},i}(t) + jx_{\mathrm{Im},i}(t)$, which is generated from the i-th NHS-OFDM modulator. It is assumed that LED $2i$–1 and LED $2i$ transmit the Re part and the Im part of the complex-valued signal, respectively. After indoor free-space propagation, the light is detected by an ImR. The DC component is removed from the received signal and the resultant electrical signal vector is expressed by

$$\mathbf{y}_i = RP_0\xi\, \mathbf{H}\mathbf{x}_i + \mathbf{n}_i, \tag{3.15}$$

where **H** is the channel matrix and $\mathbf{n}_i$ is the additive noise vector. The channel matrix **H** has a dimension of $(k_1 + k_2) \times 2$, where k_1 and k_2 are the numbers of detectors that are covered by the two light spots corresponding to LED $2i$–1 and LED $2i$, respectively. For an indoor imaging MIMO-VLC system using an ImR, the ICI becomes negligible. Hence, the channel matrix **H** can be represented by a diagonal matrix, which is given by

$$\mathbf{H} = \mathrm{diag}(\underbrace{h_{1,2i-1},\cdots,h_{k_1,2i-1}}_{\text{Re part}},\ \underbrace{h_{k_1+1,2i},\cdots,h_{k_1+k_2,2i}}_{\text{Im part}}). \tag{3.16}$$

Substituting Eq. (3.16) into Eq. (3.15) yields the received electrical signal vectors of the 2N-channel imaging MIMO-VLC system using an ImR. Moreover, the noise vector $\mathbf{n}_i$ is given by $\mathbf{n}_i = [n_{\mathrm{Re},i}\ n_{\mathrm{Im},i}]^T$, where $n_{\mathrm{Re},i}(t)$ and $n_{\mathrm{Im},i}(t)$ can both be modeled as real-valued AWGNs, each consisting of shot noise and thermal noise.

In order to recover the transmitted data from the received signals, ZF based MIMO De-MUX is performed and the estimate of the transmitted signal vector is given by

$$\tilde{\mathbf{x}}_i = \frac{1}{RP_{\mathrm{opt}}\xi}\mathbf{H}^{-1}\mathbf{y}_i = \mathbf{x}_i + \frac{1}{RP_{\mathrm{opt}}\xi}\mathbf{H}^{-1}\mathbf{n}_i. \tag{3.17}$$

It is known that each light spot may cover multiple detectors in the detector array of the ImR and multiple output signals carrying the same signal are obtained. Thus, diversity combining can be performed to generate a final output signal. In this analysis, select-best combining (SBC) is adopted for simplicity [34]. When using SBC, the detector that has the highest SNR is selected. After diversity combining, the real and imaginary signals from two light spots can be obtained by

$$\begin{cases} \tilde{x}_{\mathrm{Re},i} = \arg\max\limits_{\tilde{x}_{ij}} \{\mathrm{SNR}(\tilde{x}_{ij})\},\ 1 \le j \le k_1 \\ \tilde{x}_{\mathrm{Im},i} = \arg\max\limits_{\tilde{x}_{ij}} \{\mathrm{SNR}(\tilde{x}_{ij})\},\ k_1+1 \le j \le k_1+k_2 \end{cases}, \tag{3.18}$$

where $\mathrm{SNR}(\tilde{x}_{ij})$ is the estimated SNR of $\tilde{x}_{ij}(t)$ which is the j-th element of $\tilde{\mathbf{x}}_i$. Following Eq. (3.18), the corresponding optical channel gains can also be attained by

$$\begin{cases} h_{\mathrm{Re},i} = \arg\max\limits_{h_{ij}} \{\mathrm{SNR}(\tilde{x}_{ij})\},\ 1 \le j \le k_1 \\ h_{\mathrm{Im},i} = \arg\max\limits_{h_{ij}} \{\mathrm{SNR}(\tilde{x}_{ij})\},\ k_1+1 \le j \le k_1+k_2 \end{cases}, \tag{3.19}$$

where h_{ij} is the j-th diagonal element of **H**. Therefore, the complex-valued signal at the input of the i-th NHS-OFDM demodulator can be reconstructed by

$$\tilde{x}_i = \tilde{x}_{\mathrm{Re},i} + j\tilde{x}_{\mathrm{Im},i}. \tag{3.20}$$

Based on Eq. (3.20), the SNR of the received complex-valued signal can be obtained by

$$\mathrm{SNR}_i = \frac{2(RP_{\mathrm{opt}}\xi h_{\mathrm{Re},i}h_{\mathrm{Im},i})^2}{h_{\mathrm{Im},i}^2\sigma_{\mathrm{Re},i}^2 + h_{\mathrm{Re},i}^2\sigma_{\mathrm{Im},i}^2}, \tag{3.21}$$

where $\sigma_{\mathrm{Re},i}^2$ and $\sigma_{\mathrm{Im},i}^2$ are the variances of $n_{\mathrm{Re},i}(t)$ and $n_{\mathrm{Im},i}(t)$, respectively. Substituting Eq. (3.21) into Eq. (3.7) yields the BER, i.e. BER_i, obtained at the output of the *i*-th NHS-OFDM demodulator. Finally, the average BER of the 2N-channel imaging MIMO-VLC system using NHS- OFDM is given by

$$\mathrm{BER}_{\mathrm{av}} = \frac{1}{\mathrm{N}}\sum_{i=1}^{\mathrm{N}} \mathrm{BER}_i\,. \tag{3.22}$$

3.5.3 Comparison of different LED pairing schemes

Based on the analytical expressions derived above, the performance of different LED pairing schemes in an indoor four-channel imaging MIMO-VLC system is compared [145]. The key parameters of the system are listed in Table 3.2. A typical room with a dimension (length × width × height) of 5 m × 5 m × 3 m is considered and the height of the receiving plane is 0.85 m. All the four LEDs have the same semi-angle at half power of 60° and each LED consists of four chips. The modulation index is 0.3 and the modulation bandwidth is 50 MHz. Although the 3-dB modulation bandwidth of a phosphor-coated white LED is only several MHz, the modulation bandwidth can be increased by using pre-FDE techniques [26,163]. 16QAM ($I = 4$, $J = 4$) mapping is adopted in NHS-OFDM modulation and demodulation. Thus, the raw data rate achieved in this four-channel MIMO-VLC system is $4 \times \log_2 16 \times 50 = 800$ Mb/s. The gains of the optical filter and lens are both assumed to be 1. The active area and responsivity of the detector used are 19.6 mm^2 and 0.53 A/W, respectively. For simplicity of analysis and without loss of generality, it is assumed that each light spot covers four detectors. Moreover, the background current due to ambient light is 190 μA. For the purpose of comparison, the performance of an indoor four-channel imaging MIMO-VLC system using HS-OFDM with exactly the same parameters is also investigated.

Table 3.2. Key parameters of the four-channel MIMO-VLC system

Parameter	**Value**
Room dimension	5m×5m×3m
Height of receiving plane	0.85 m
Transmitter semi-angle at half power	60°
Modulation index	0.3
Modulation bandwidth	50 MHz
Gain of optical filter	1
Gain of optical lens	1
Responsivity of PD	0.53 A/W

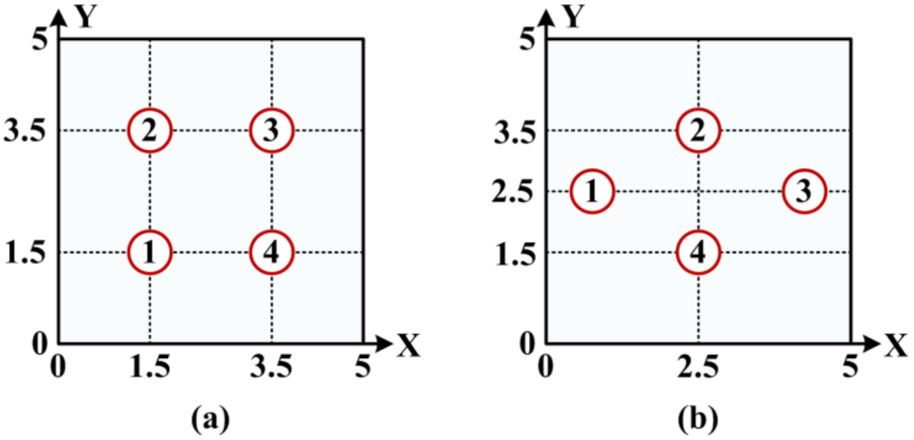

Figure 3.12. Two LED placements (a) square and (b) rhombus.

Figs. 3.12(a) and (b) depict the square and rhombic LED placements, respectively. The coordinates of the lower left corner of the floor are set to (0, 0, 0) and the units of all the coordinates are meters. In the square placement, the coordinates of the four LEDs are (1.5, 1.5, 3), (1.5, 3.5, 3), (3.5, 3.5, 3) and (3.5, 1.5, 3), as in Fig. 3.12(a). However, the coordinates in the rhombic placement are ($2.5-\sqrt{3}$, 2.5, 3), (2.5, 3.5, 3), ($2.5+\sqrt{3}$, 2.5, 3) and (2.5, 1.5, 3), as can be seen from Fig. 3.12(b).

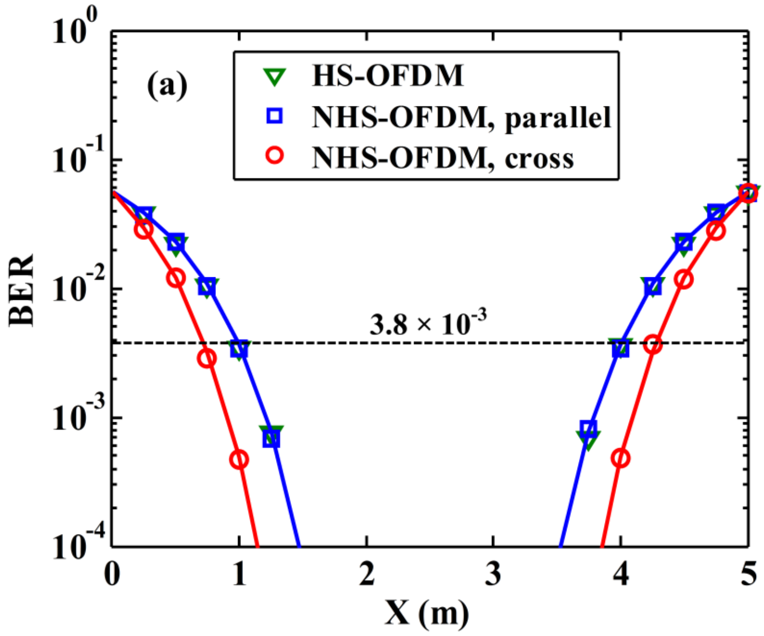
(a)
HS-OFDM
NHS-OFDM, parallel
NHS-OFDM, cross
3.8 × 10^-3
BER
10^0
10^-1
10^-2
10^-3
10^-4
0
1
2
3
4
5
X (m)

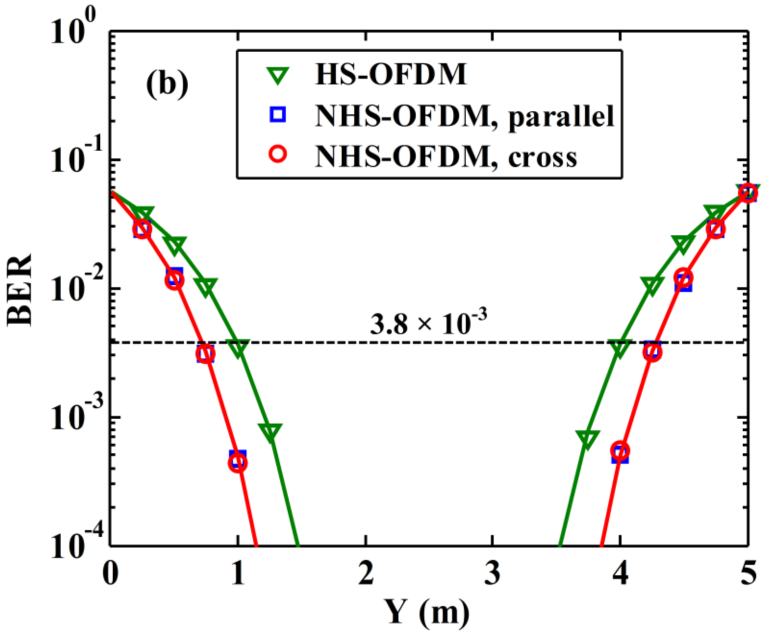
(b)
HS-OFDM
NHS-OFDM, parallel
NHS-OFDM, cross
3.8 × 10^-3
BER
10^0
10^-1
10^-2
10^-3
10^-4
0
1
2
3
4
5
Y (m)

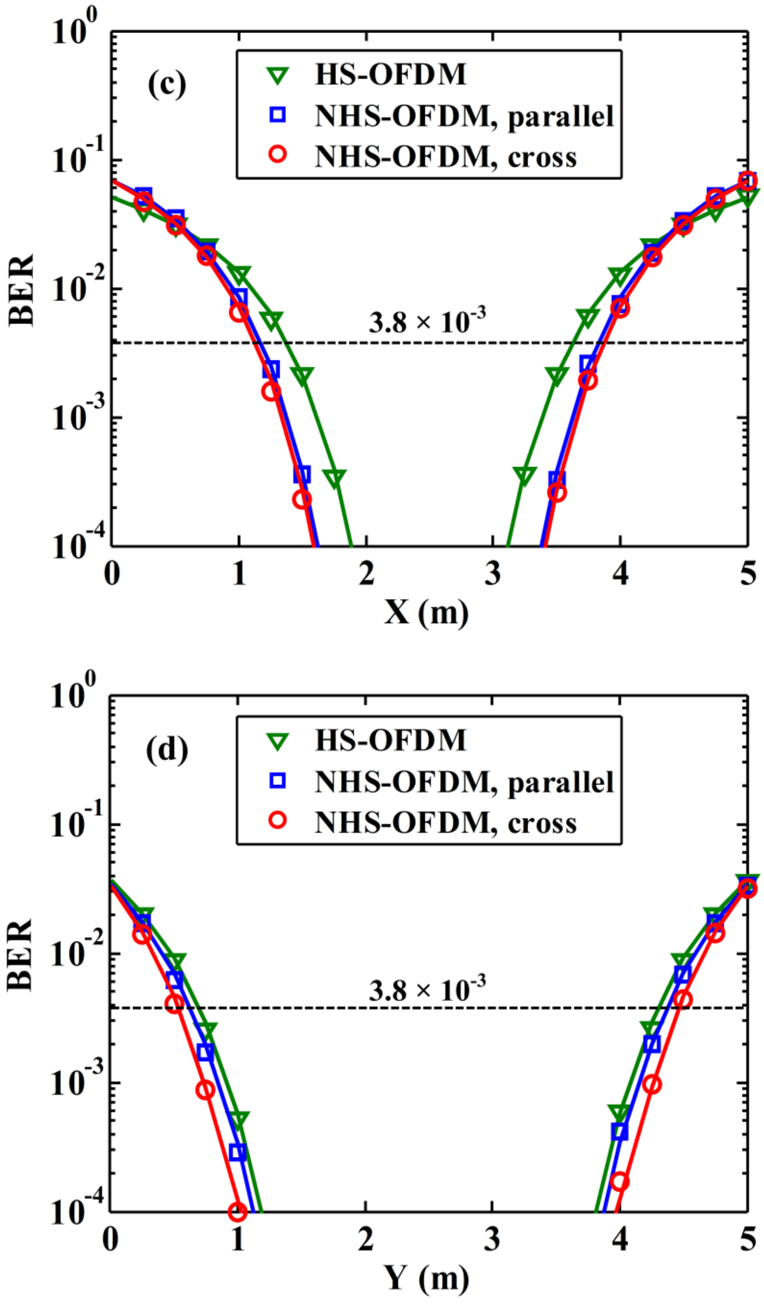

Figure 3.13. (a) BER versus X with Y = 2.5 m for a square LED placement, (b) BER versus Y with X = 2.5 m for a square LED placement, (c) BER versus X with Y = 2.5 m for a rhombic LED placement, and (d) BER versus Y with X = 2.5 m for a rhombic LED placement.

The BER performance of the four-channel imaging MIMO-VLC system is first analyzed, in which two modulation techniques (HS-OFDM and NHS-OFDM) and two LED placements (square and rhombus) are considered for comparison. Besides analytical results, Monte Carlo simulations are further conducted where totally 2000 HS-OFDM/NHS-OFDM symbols are transmitted for BER measurement. The average transmitted optical power of each LED in the indoor four-channel imaging MIMO-VLC system is set to 8 W.

Fig. 3.13 shows the BER performance of the four-channel imaging MIMO-VLC system, where the simulation results and the analytical results are represented by markers and lines, respectively. It can be clearly observed that the analytical results agree very well with the simulation results.

Fig. 3.13(a) plots the BER versus receiver position offset along the X direction with Y = 2.5 m for a square LED placement. It can be seen that the same BER performance is obtained for HS-OFDM and parallel pairing based NHS-OFDM, while the best BER performance is achieved by NHS-OFDM with cross pairing. As a general conclusion obtained in [144], NHS-OFDM can outperform HS-OFDM only when two HS-OFDM signals have different SNRs. For Y = 2.5 m, the HS-OFDM signals from LED 1 and LED 2 (LED 3 and LED 4) have the same SNRs, and hence HS-OFDM and NHS-OFDM have the same BER performance when LED 1 and LED 2 (LED 3 and LED 4) are paired together. However, when cross pairing is adopted, the HS-OFDM signals from LED 1 and LED 2 (LED 3 and LED 4) always have different SNRs along the X direction for Y = 2.5 m, except X = 2.5 m. As a result, NHS-OFDM with cross pairing can achieve much better BER performance than HS-OFDM and NHS-OFDM with parallel pairing. However, for X = 2.5 m as shown in Fig. 3.13(b), NHS-OFDM outperforms HS-OFDM along the Y direction with either parallel or cross pairing. It is revealed that NHS-OFDM can achieve the same BER performance with parallel pairing or cross pairing, due to the geometric symmetry.

In contrast, when the four LEDs are placed in a rhombus, the geometric symmetry no longer exists. As can be seen from Figs. 3.13(c) and (d), NHS-OFDM with cross pairing outperforms NHS-OFDM with parallel pairing, while HS-OFDM attains the worst BER performance. As shown in Figs. 3.13(a) to (d), the BER performance of an MIMO-VLC system using NHS-OFDM largely depends on the way that the LEDs are paired. Considering the impact of LED pairing, it can be generally concluded that NHS-OFDM with cross pairing is the best option for the MIMO-VLC system, with either a square or a rhombic LED placement.

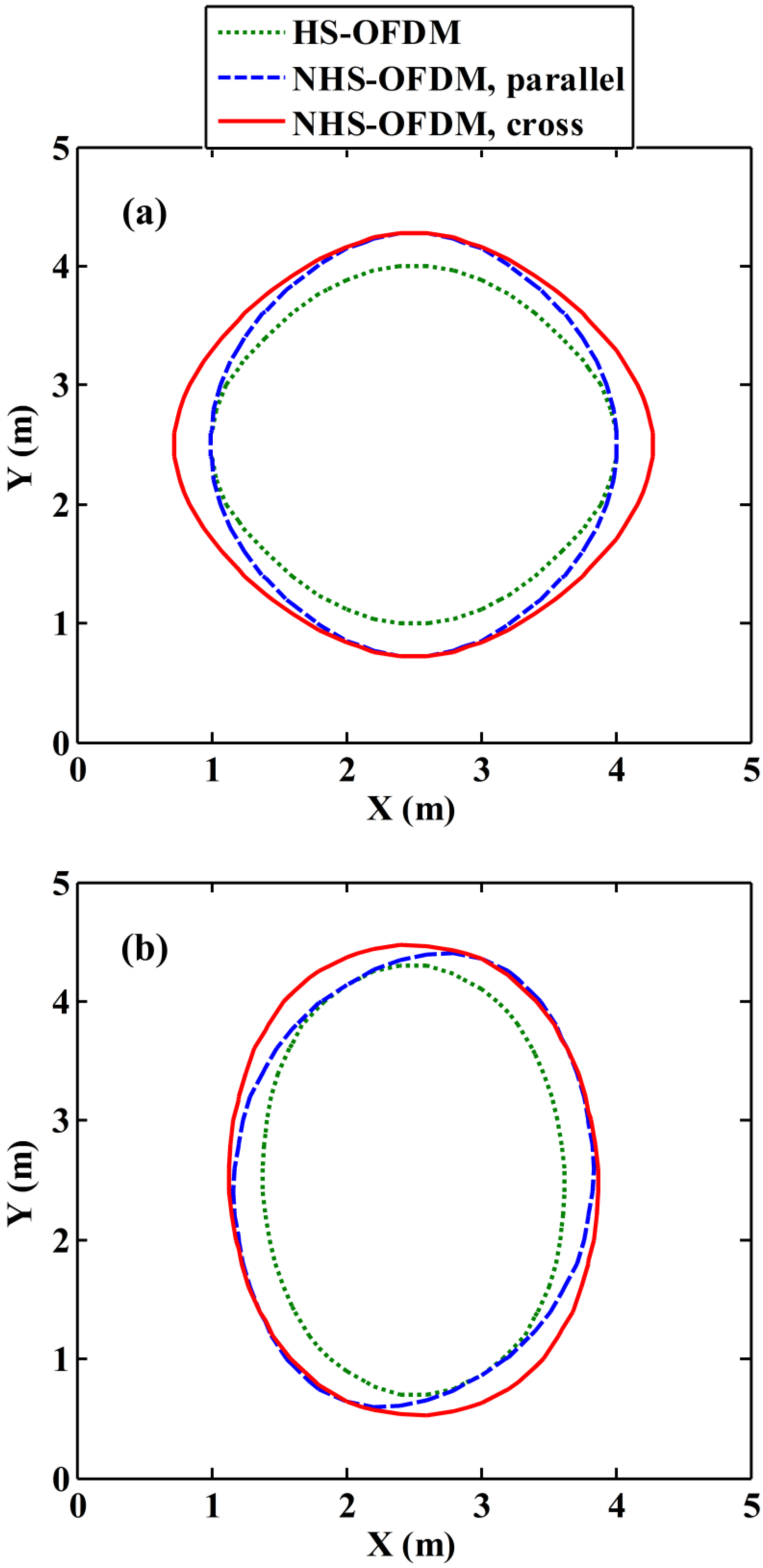

Figure 3.14. Communication coverage of the four-channel imaging MIMO-VLC system at a target BER of 3.8×10^{-3} for (a) a square LED placement and (b) a rhombic LED placement. The average transmitted optical power per LED is 8 W.

The communication coverage of the four-channel imaging MIMO-VLC system at a target BER of 3.8×10^{-3} is shown in Fig. 3.14, where the average transmitted optical power of each LED is 8 W. For a square LED placement, the coverages using HS-OFDM are covered by the green dotted lines, as shown in Fig. 3.14(a), while the coverages using NHS-OFDM with parallel and cross pairing are covered by the blue dashed lines and the red solid lines, respectively. As can be seen, the coverage contours using both HS-OFDM and NHS-OFDM with cross pairing can be approximated as circles, while the coverage contours using NHS-OFDM with parallel pairing can be approximated as ellipses. The area of a circle is calculated by $A_\mathrm{c} = \pi r_\mathrm{c}^2$ where r_c is the radius of the circle, and the area of an ellipse is given by $A_\mathrm{e} = \pi ab$ where a and b are the major and minor axes of the ellipse, respectively. The coverage circle using HS-OFDM has a radius of 1.5 m and hence the area is 7.1 m^2.

By replacing HS-OFDM with NHS-OFDM, the covered area can be improved. Specifically, the coverage contour becomes an ellipse when utilizing NHS-OFDM with parallel pairing, indicating that the coverage is only increased along the Y direction while the coverage along the X direction remains the same. The major and minor axes of the coverage ellipse are 1.8 and 1.5 m, and hence the area is 8.5 m^2, suggesting a communication coverage improvement of about 19.7%. Moreover, the coverage circle using NHS-OFDM with cross pairing has a radius of 1.8 m and the area is 10.2 m^2. As a result, a further 20% coverage improvement is obtained by using cross pairing.

For a rhombic LED placement, as can be seen from Fig. 3.14(b), the coverage contours using HS-OFDM and NHS-OFDM can all be approximated as ellipses. Similarly, the smallest coverage is attained by HS-OFDM, while NHS-OFDM with cross pairing outperforms NHS-OFDM with parallel pairing in terms of covered area. As can be seen from Figs. 3.14(a) and (b), LED pairing is a key factor that determines the communication coverage of NHS-OFDM based MIMO-VLC systems. By selecting a proper LED pairing scheme, the communication coverage area of NHS-OFDM based indoor MIMO-VLC systems can be maximized.

Besides LED pairing, the average transmitted optical power of each LED is another key factor that needs to be examined. Fig. 3.15 shows the relationship between the covered area and the average transmitted optical power per LED in the indoor four-channel imaging MIMO-VLC system using HS-OFDM and cross pairing based NHS-OFDM at a target BER of 3.8×10^{-3}. For a square LED placement, as shown in Fig. 3.15(a), the covered area is continuously increased with the increase of the average transmitted optical power of each LED. For a rhombic LED placement, as shown in Fig. 3.15(b), the covered area also continuously increases with the increase of the average transmitted optical power of each LED.

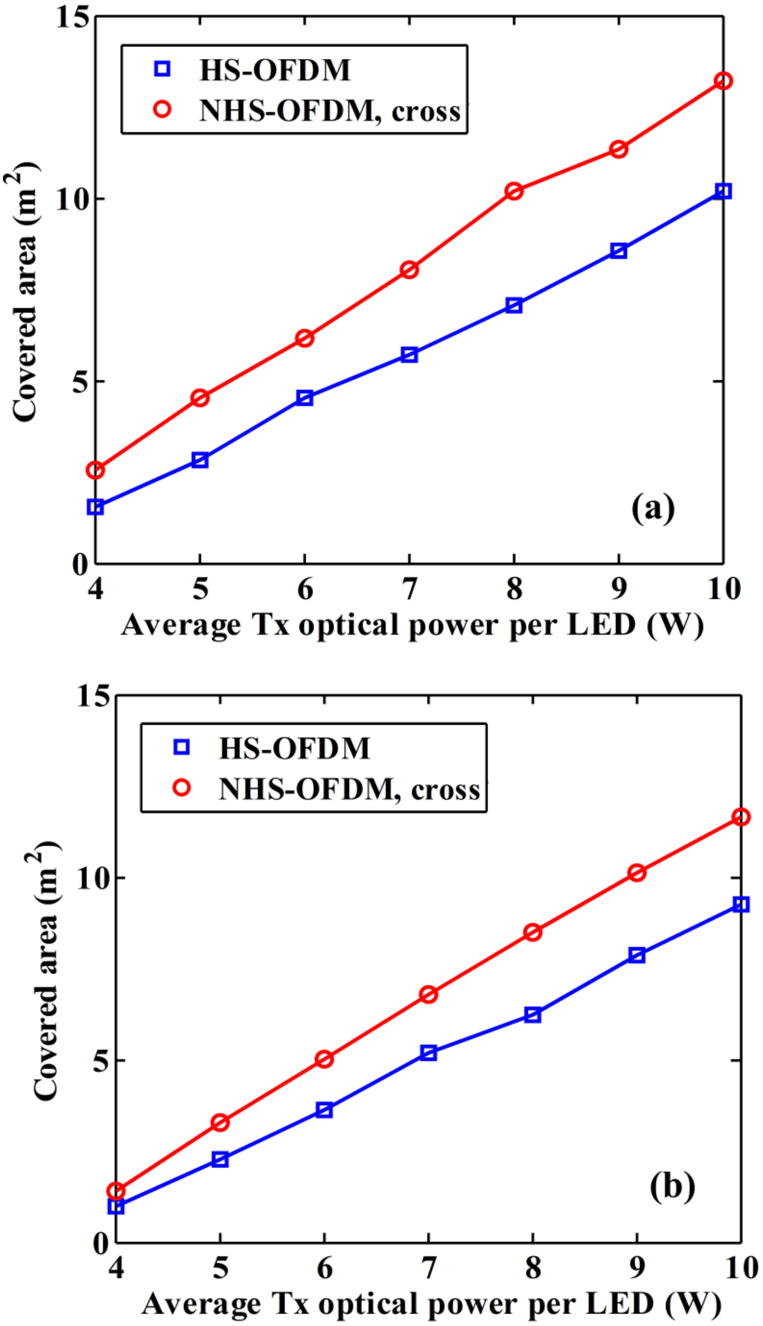

Figure 3.15. Communication coverage area versus average transmitted optical power per LED at a target BER of 3.8×10^{-3} for (a) a square LED placement and (b) a rhombic LED placement.

In conclusion, an indoor four-channel imaging MIMO-VLC system, with either a square or a rhombic LED placement, achieves the largest communication coverage by using NHS-OFDM with cross pairing.

3.6 Conclusion

In this chapter, a novel NHS-OFDM modulation scheme has been proposed for MIMO-VLC systems. The HS constraint imposed in conventional HS-OFDM is removed by transmitting the real and imaginary parts of a complex-valued OFDM signal through a pair of white LEDs in the MIMO-VLC system. The performance of an indoor MIMO-VLC system employing the proposed NHS-OFDM modulation scheme has been investigated and demonstrated by both numerical analysis and proof-of-concept experiments. The performance of conventional HS-OFDM has also been investigated in such a system for comparison. The analytical BER expressions of a general MIMO-VLC system using both HS-OFDM and NHS-OFDM have been derived, which have also been successfully verified by Monte Carlo simulations. The analytical results have shown that the 2×2 MIMO-VLC system using NHS-OFDM exhibits lower or comparable computational complexity as the system using HS-OFDM, but achieves superior BER performance. As a general conclusion, it has been shown that NHS-OFDM can always achieve BER improvements over HS-OFDM as long as the two HS-OFDM signals have different SNRs. More specifically, a non-imaging 2×2 MIMO-VLC system using NHS-OFDM achieves communication coverage improvements of 15.4% and 13.6% when the constellations are BPSK and 4QAM, respectively, compared with the same system utilizing conventional HS-OFDM. Moreover, the coverage improvement is increased when an ImR is adopted in the 2×2 MIMO-VLC system. The analytical results have also revealed that the coverage improvement is only slightly reduced when the order of constellation is increased. The experimental results have further verified that, for a target BER of 3.8×10^{-3}, NHS-OFDM improves the communication coverage area of a 400 Mb/s imaging 2×2 MIMO-VLC system by about 30% compared with HS-OFDM. Furthermore, the impact of LED pairing on the performance of NHS-OFDM based MIMO-VLC systems has also been analyzed. It has been shown that an indoor four-channel imaging MIMO-VLC system, with either a square or a rhombic LED placement, achieves the largest communication coverage by using NHS-OFDM with cross pairing. In conclusion, NHS-OFDM can be a promising technique for MIMO-VLC based high-speed indoor wireless access.

Chapter 4 Imaging Receiver Using Angle Diversity Detectors for MIMO-VLC

4.1 Introduction

As discussed in Chapter 3, MIMO is a very natural and effective way to increase the capacity of indoor VLC systems and MIMO-VLC based high-speed indoor wireless communication has attracted tremendous attention in recent years [103, 105–109]. In indoor MIMO-VLC systems, LOS transmission is usually considered and the optical channel gains between one LED and two closely placed PDs could be very similar, resulting in high spatial correlation that might severely degrade the performance of MIMO-VLC systems [32]. So far, many techniques have been proposed to reduce the high channel correlation of MIMO-VLC systems. In [92, 152], power imbalance was applied among multiple LED transmitters so as to reduce channel correlation. A prism-array receiver was proposed in [153], where a prism is placed on the surface of a PD array so that a full-rank MIMO channel matrix can be achieved. In [154], a photonic crystal based narrow-window angular filter was applied in front of the PD array, enabling interference-free parallel transmission.

Besides, non-imaging angle diversity receivers (NImADRs) have been proposed to reduce the channel correlation of MIMO-VLC systems, including an angular-segmented receiver [104], a receiver using inclined photodetectors (PDs) [105] and a pyramid or hemispheric shaped receiver [106]. Nevertheless, NImADRs can only reduce the channel correlation to a certain extent and the capacity improvement is limited, which largely depends on the performance of the NImADR applied. As reported in [32, 46, 107, 143], imaging receivers (ImRs) reveal the potential to fully exploit the capacity of MIMO-VLC systems, because they can effectively decorrelate the multiplexed channels and hence reduce the channel correlation. Due to the negligible inter-channel interference, ImRs based MIMO is also referred to as space division multiplexing (SDM) [109]. A Gigabit/s MIMO-VLC system using a convex lens based ImR was demonstrated in [107]. However, the coverage of such a system is limited due to the small field-of-view (FOV) of the ImR. The FOV of a conventional ImR is mainly determined by the imaging lens and the size of the planar PD array [46]. In order to improve the FOV of an ImR, two advanced imaging lenses have been adopted to replace the common convex lens, including a fisheye lens [109] and a hemispherical lens [155], [156].

In this chapter, an imaging angle diversity receiver (ImADR) is proposed and analyzed for the reduction of channel correlation and hence communication coverage improvement in indoor

MIMO-VLC systems [157]. By using angle diversity PDs instead of vertically oriented PDs, the proposed ImADR has a wider FOV and achieves higher optical channel gain than the conventional ImR. The performance of the proposed ImADR in an indoor four-channel MIMO-VLC system is evaluated. It is revealed that, for a target bit error rate (BER) of 10^{-3}, the system using the proposed ImADR achieves 44% reduction in the average transmitted optical power and 130% improvement in the communication coverage area in comparison to the system using a conventional ImR.

The rest of the chapter is organized as follows. In Section 4.2, the principle of the proposed ImADR is first introduced. Performance comparison between ImR and ImADR is presented in Section 4.3, in terms of FOV, area of detector array and optical channel gain. In Section 4.4, the BER performance of indoor MIMO-VLC systems employing different types of receivers is analyzed. Finally, Section 4.5 concludes this chapter. The content of this chapter is related to the author’s work shown in [157, 158].

4.2 Principle of ImADR

The schematic diagram of the proposed ImADR is shown in Fig. 4.1. The ImADR consists of an imaging lens, an optical filter and an array of angle diversity PDs. The imaging lens is used to project the incident light from the LED arrays onto the PD array. The optical filter is used to attenuate the unwanted ambient light.

Differing from the conventional ImR which has a two-dimensional (2-D) circular PD array consisting of vertically oriented PDs, as shown in Fig. 4.2, the proposed ImADR has a three-dimensional (3-D) spherical-cap-shaped PD array consisting of angle diversity PDs. Note that either a common convex lens or an advanced imaging lens such as a fisheye lens can be adopted in the proposed ImADR. Here, a convex lens based ImADR is considered for the simplicity of analysis.

As can be seen from Fig. 4.1, each of the signal spots might cover multiple adjacent PDs. To generate a final output signal from one signal spot, the optical channel gain between an LED chip in the LED array and a PD in the PD array can be individually calculated. Those PDs that are not illuminated by the signal light can be excluded by setting an adequate threshold level [32]. The resultant signals from the PDs that are illuminated by the signal light can be further processed to obtain a final output signal via diversity combining [159].

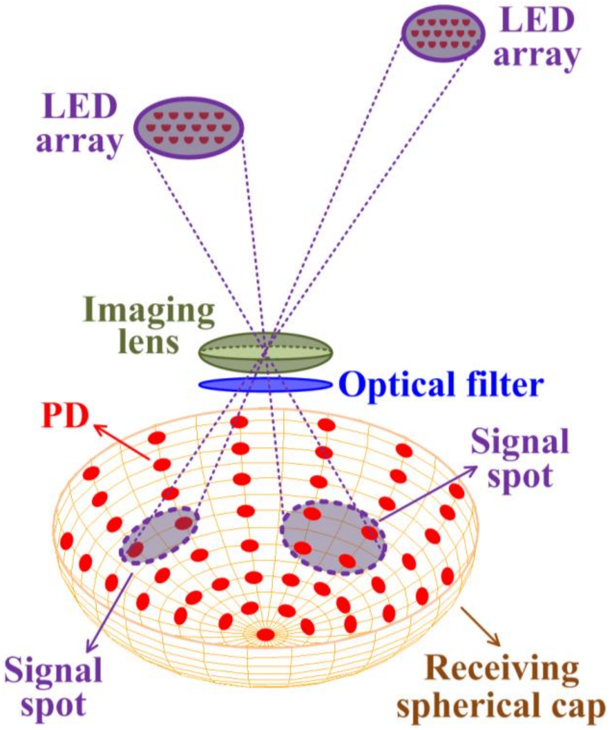

Figure 4.1. Schematic diagram of the proposed ImADR.

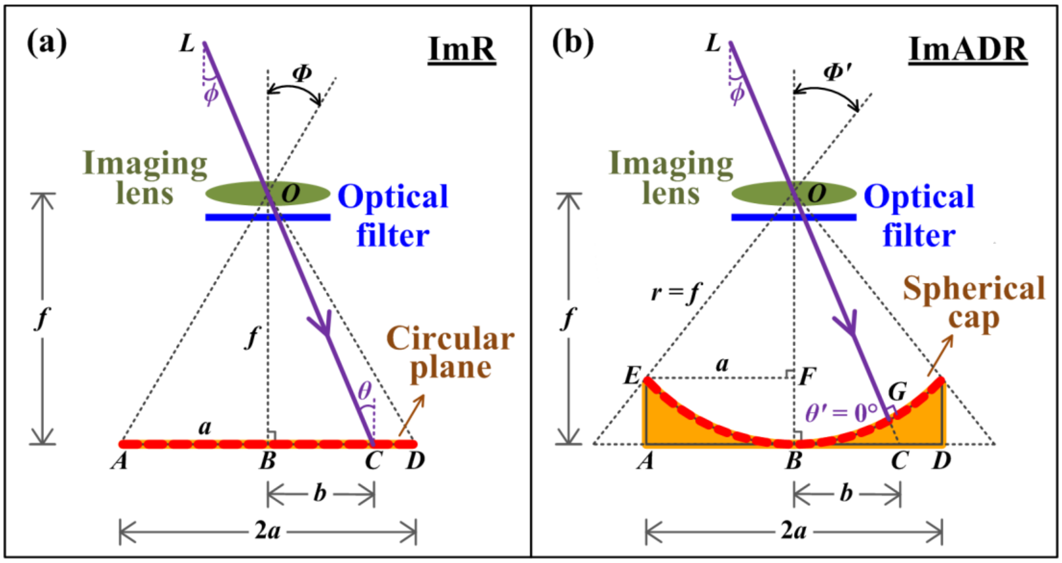

Figure 4.2. Side views of (a) a conventional ImR using vertically oriented PDs and (b) the proposed ImADR using angle diversity PDs, both with the same horizontal size.

4.3 Performance comparison between ImR and ImADR

Detailed performance comparison between a conventional ImR and the proposed ImADR is presented in terms of FOV, area of detector array and optical channel gain.

4.3.1 Field of view

Figs. 4.2(a) and (b) illustrate the side views of a conventional ImR with vertically oriented PDs and the proposed ImADR with angle diversity PDs, respectively. In the conventional ImR, f is the focal length of the convex lens, a is the radius of the 2-D circular PD array, and Φ is the half-angle FOV of the ImR. Using the right triangle OAB, Φ is given by

$$\Phi = \tan^{-1}(AB/OB) = \tan^{-1}(a/f). \tag{4.1}$$

As can be seen from Fig. 4.2(a), the horizontal size of an ImR is determined by the diameter of the 2-D circular PD array. For an ImADR with the same horizontal size, as shown in Fig. 4.2(b), the radius of the base of the 3-D spherical-cap-shaped PD array in the ImADR is equal to the radius a of the circular PD array in the ImR. It is assumed that the spherical-cap-shaped PD array is centered at O and the radius of the spherical cap is $r = f$. Using the right triangle OEF, the half-angle FOV of the ImADR is obtained by

$$\Phi' = \sin^{-1}(EF/OE) = \sin^{-1}(a/f). \tag{4.2}$$

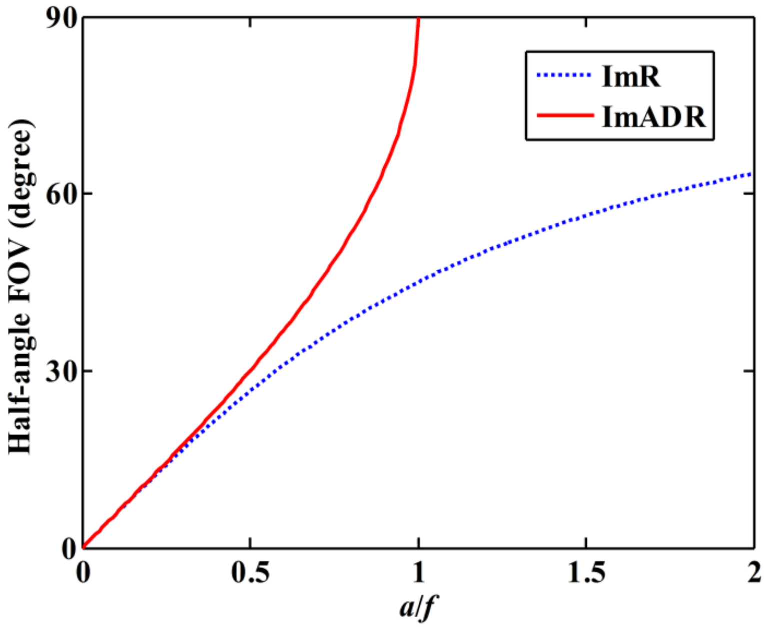

Figure 4.3. Half-angle FOV versus a/f for ImR and ImADR.

Fig. 4.3 shows the relationship between the half-angle FOV and the ratio a/f for both ImR and ImADR, with the latter achieving a much larger FOV than the former. For example, at $a/f = 1$, the half-angle FOVs are 45° and 90° for the ImR and the ImADR, respectively. Moreover, to achieve the same FOV of 60°, the required values for a/f are 1.73 and 0.87 for the ImR and ImADR, respectively. Hence, about 75% reduction in the horizontal area of the receiver is achieved by using ImADR in comparison to ImR.

4.3.2 Area of detector array

As shown in Fig. 4.2(a), the area of the 2-D circular PD array of the conventional ImR which has a radius of a is given by $A_{\mathrm{ImR}} = \pi a^2$. Since $a = f\tan\Phi$, A_{ImR} is calculated by

$$A_{\mathrm{ImR}} = \pi f^2 \tan^2\Phi. \tag{4.3}$$

For an ImADR with the same half-angle FOV Φ, as shown in Fig. 4.2(b), the area of the 3-D spherical-cap-shaped PD array is given by $A_{\mathrm{ImADR}} = 2\pi fe$, where e is the height of the spherical cap.

Using similarity between triangles OAB and OCD, the equation $a'f = a(f - e)$ can be obtained. Moreover, using the right triangle OCD, the equation $CD^2 = OC^2 - (OB - BD)^2$ can also be attained. After some geometrical calculations, the height of the spherical cap is obtained by

$$e = f - \frac{f^2}{\sqrt{f^2 + a^2}}. \tag{4.4}$$

Using $a = f\tan\Phi$, e is given by

$$e = f\left(1 - 1/\sqrt{1 + \tan^2\Phi}\right). \tag{4.5}$$

Using the relationship $1 + \tan^2\Phi = 1/\cos^2\Phi$, e is obtained by

$$e = f(1 - \cos\Phi). \tag{4.6}$$

Moreover, using the relationship $1 - \cos\Phi = 2\sin^2(\Phi/2)$, e is finally defined as

$$e = 2f\sin^2(\Phi/2). \tag{4.7}$$

Hence, the area of the spherical-cap-shaped PD array of ImADR is obtained by

$$A_{\mathrm{ImADR}} = 4\pi f^2 \sin^2(\Phi/2). \tag{4.8}$$

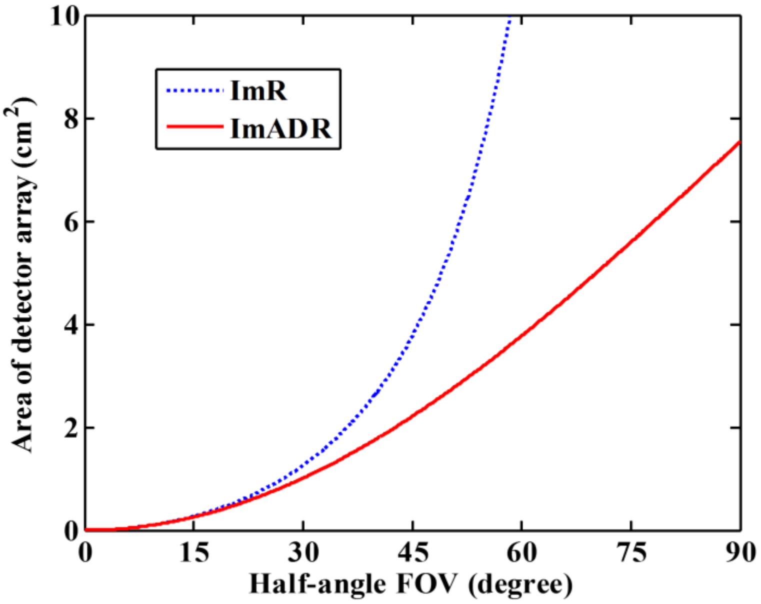

Figure 4.4. Area of detector array versus half-angle FOV.

Fig. 4.4 displays the relationship between the area of detector array and the half-angle FOV, where the focal length of the imaging lens is assumed to be 1.2 cm. It can be observed that ImADR has a smaller area of detector array than ImR, especially for a large half-angle FOV. For example, for the half-angle FOV of 45°, the detector array areas are 3.8 cm^2 and 2.2 cm^2 for the ImR and ImADR, respectively. Hence, a detector array area reduction of about 42% is achieved by using the ImADR. Since the number of detectors is mainly determined by the area of the detector array, it can be concluded that ImADR requires fewer detectors than the conventional ImR for achieving the same FOV.

4.3.3 Optical channel gain

In typical indoor environments with LEDs lighting fixtures, the receiver can detect both the line-of-sight (LOS) and diffuse components. Here only the LOS component is considered in the analysis, since the light intensity of the LOS path is much higher than that of the diffuse paths [32].

The LOS irradiance of an LED can be modeled by a generalized Lambertian radiation pattern and the optical channel gain between the t-th LED array and the r-th PD in the PD array can be calculated by [32]

$$h_{rt} = \sum_{i=1}^{n} \frac{(m+1)A_{\mathrm{PD}}}{2\pi d_{rt_i}^2} \mu\eta \cos^m \phi_{rt_i} \cos\theta_{rt_i} , \tag{4.9}$$

where n is the number of LED chips in each LED array, $m = -\ln 2/\ln(\cos(\Psi_{1/2}))$ is the order of Lambertian emission, $\Psi_{1/2}$ is the transmitter semi-angle at half power, A_{PD} is the active area of the PD, d_{rti} is the distance between the i-th LED chip in the t-th LED array and the r-th PD, μ and η are the gains of the optical filter and the imaging lens, respectively, ϕ_{rti} is the emission angle, and θ_{rti} is the incident angle. If θ_{rti} is outside the FOV of the receiver, the optical channel gain h_{rt} becomes zero.

For both the conventional ImR and the proposed ImADR, all the parameters in Eq. (4.9) are the same except for d_{rti} and θ_{rti}. As shown in Fig. 4.2(b), the difference in the distance is denoted by CG, which is negligible in comparison to the distance between the LED array and the imaging lens. Thus, the difference in the optical channel gains between the ImR and the ImADR is primarily caused by different incident angles.

Assuming that both the ImR and the ImADR are vertically oriented, see Fig. 4.2(a), the incident angle θ of the ImR is equal to the emission angle ϕ, which is given by using the right triangle OBC

$$\theta = \tan^{-1}(BC/OB) = \tan^{-1}(b/f), \tag{4.10}$$

where b $(0 \leq b \leq a)$ is the distance between the center of the focal plane and the image of the LED chip on the focal plane.

In the ImADR, as in Fig. 4.2(b), the incident angle $\theta' = 0°$ since the spherical-cap-shaped PD array is centered at O. Substituting θ and θ' into Eq. (4.9) yields the optical channel gain of the ImR h_{ImR} and that of the ImADR h_{ImADR}, respectively. The ratio between h_{ImADR} and h_{ImR} (i.e., the optical channel gain improvement) is given by

$$\frac{h_{\mathrm{ImADR}}}{h_{\mathrm{ImR}}} = \frac{\cos\theta'}{\cos\theta} = \frac{1}{\cos(\tan^{-1}(b/f))}. \tag{4.11}$$

From the practical point of view, Eq. (4.11) indicates the improvement in the received optical and electrical power levels.

Fig. 4.5 shows the relationship between the optical channel gain improvement and a/f. It can be seen that the optical channel gain improvement increases continuously with the increase of a/f. For $b = a/2$, an improvement of 3 dB is achieved when a/f is 1.8. Moreover, the optical channel gain improvement also increases with b. An optical channel gain improvement of 8 dB is achieved for $a/f = 2$ when $b = a$.

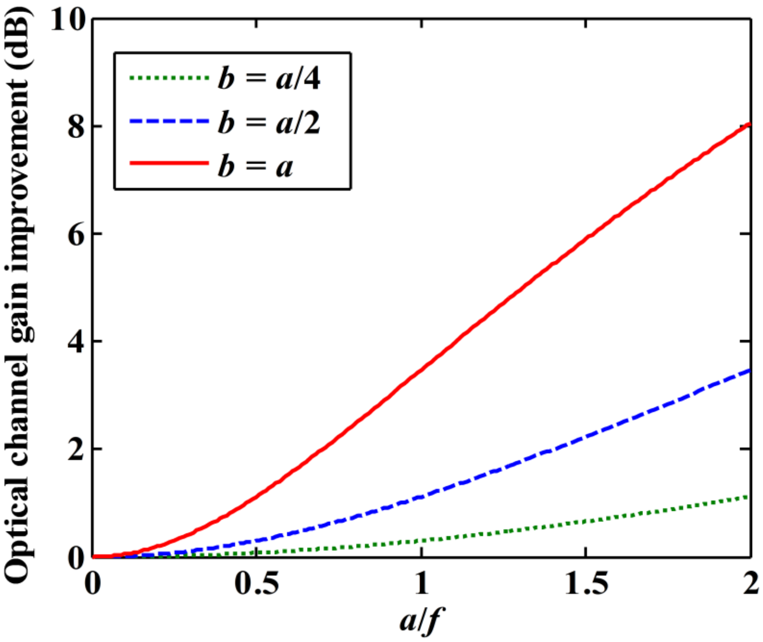

Figure 4.5. Optical channel gain improvement in dB versus *a*/*f* for a range of *b*.

4.4 BER performance

4.4.1 BER analysis

The analytical BER expression for an indoor imaging MIMO-VLC system using the proposed ImADR and OFDM modulation is derived. It is assumed that N independent OFDM signals are modulated onto N LED arrays, respectively, which are transmitted in the free space and received by a PD array, and there are total N signal spots on the PD array, corresponding to N LED arrays [46]. Moreover, the j-th ($1 \le j \le N$) spot covers k adjacent PDs. Following [159], the signal-to-noise ratio (SNR) at the output of the i-th PD in the j-th spot can be calculated by

$$SNR_{ij} = \frac{(R\gamma P_{r,ij})^2}{\sigma_{tot,ij}^2}, \quad 1 \le i \le k, \tag{4.12}$$

where R is the responsivity of the PD and γ is the modulation index. $P_{r,ij} = h_{ij}P_0$ is the average received optical power, where h_{ij} is the optical channel gain between the i-th PD and the j-th LED array, and P_0 is the average transmitted optical power of the j-th LED array. Moreover, $\sigma_{tot,ij}^2$ is the total AWGN including both shot and thermal noises, i.e., $\sigma_{tot,ij}^2 = \sigma_{shot,ij}^2 + \sigma_{thermal,ij}^2$ [32].

Since k output signals can be obtained from the k adjacent PDs in the j-th signal spot, diversity combining techniques can be adopted to re-generate the final output signal. Here two diversity combining techniques are considered, which are the select-best combining (SBC) and the maximal-ratio combining (MRC) [159]. In SBC, a PD in the PD array with the highest SNR is selected with the SNR given by

$$SNR_{\mathrm{SBC},j} = \max_i \left\{ \frac{(R\gamma P_{\mathrm{rx},ij})^2}{\sigma^2_{\mathrm{tot},ij}} \right\} = \max_i \{ \mathrm{SNR}_{ij} \} . \tag{4.13}$$

In contrast, in MRC, all the k output signals are used instead of only one by setting the weight $w_{ij} = R^2\gamma^2 P^2_{\mathrm{rx},ij} / \sigma^2_{\mathrm{tot},ij}$ [159], thereby maximizing the SNR, which is obtained by

$$SNR_{\mathrm{MRC},j} = \frac{\left(\sum_{i=1}^{k} w_{ij} R\gamma P_{\mathrm{rx},ij} \right)^2}{\sum_{i=1}^{k} w^2_{ij} \sigma^2_{\mathrm{tot},ij}} = \sum_{i=1}^{k} \frac{(R\gamma P_{\mathrm{rx},ij})^2}{\sigma^2_{\mathrm{tot},ij}} = \sum_{i=1}^{k} \mathrm{SNR}_{ij} . \tag{4.14}$$

The BER expression for the j-th channel OFDM signal using $I \times J$ rectangular QAM mapping can be approximated by [147]

$$BER_j = \frac{2}{\log_2(IJ)} \left(\frac{I-1}{I} + \frac{J-1}{J} \right) \mathrm{Q} \left(\sqrt{\frac{6SNR_j}{I^2 + J^2 - 2}} \right), \tag{4.15}$$

where $\mathrm{Q}(\cdot)$ is the Q-function. Substituting Eq. (4.13) and Eq. (4.14) into Eq. (4.15) yields the BER of the j-th channel OFDM signal using SBC and MRC, respectively. Therefore, for the N-channel imaging MIMO-VLC system, the average BER is given by

$$BER_{\mathrm{av}} = \frac{1}{N} \sum_{j=1}^{N} BER_j . \tag{4.16}$$

4.4.2 System setup and results

Monte Carlo simulations are performed to verify the above analytical results. A four-channel imaging MIMO-VLC system is considered in an indoor room environment with a dimension of 5m×3m×3m, where totally four LED arrays, each with two LED chips, are mounted in the ceiling. The geometric setup of the four-channel imaging MIMO-VLC system is illustrated in Fig. 4.6. It is assumed that each signal spot covers two PDs and each PD has an active area of 1 cm^2. The other parameters of the simulated system are given in Table 4.1. Four independent 16QAM ($I = J = 4$) OFDM signals each with a 50 MHz bandwidth are transmitted and the total data rate of the system is 800 Mb/s.

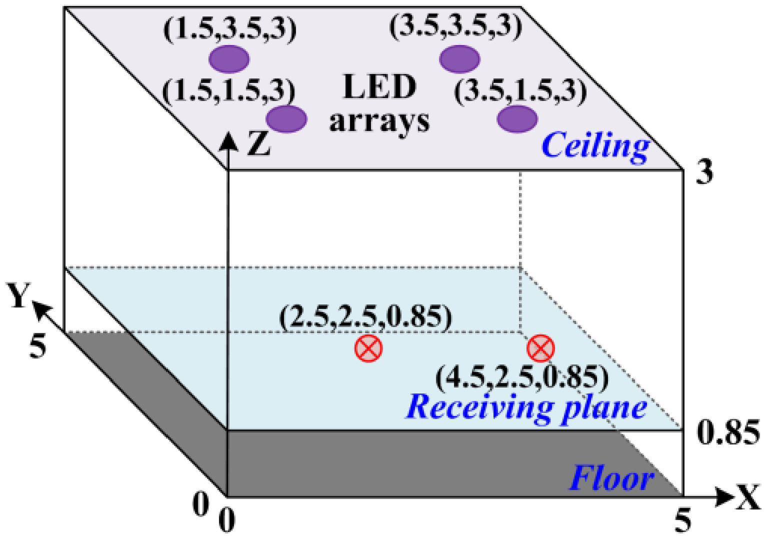

Figure 4.6. Geometric setup of the four-channel imaging MIMO-VLC system.

Table 4.1. Simulation parameters

Parameter	**Value**
Room dimension	5m×5m×3m
Locations of four LED arrays	(1.5, 1.5, 3), (1.5, 3.5, 3) (3.5, 1.5, 3), (3.5, 3.5, 3)
Height of receiving plane	0.85 m
Transmitter semi-angle at half power	60°
Modulation index	0.2
Focal length of the imaging lens	1.2 cm
Responsivity of PD	0.53 A/W
Active area of PD	1 cm^2
IFFT/FFT size	128
QAM constellation order	16
Modulation bandwidth	50 MHz
Overall data rate	800 Mb/s

Fig. 4.7 depicts the relationship between the BER and the average transmitted optical power, showing a good agreement between predicted and simulated results. For a receiver location (2.5, 2.5), i.e., the center of the receiving plane, the MRC based system requires lower optical power than the SBC based system.

With the receiver moved to the location (4.5, 2.5), the required average transmitted optical powers for MRC based ImR and ImADR are 11.8 and 6.6 W, respectively. Hence, a power reduction of about 44% is achieved by using the ImADR.

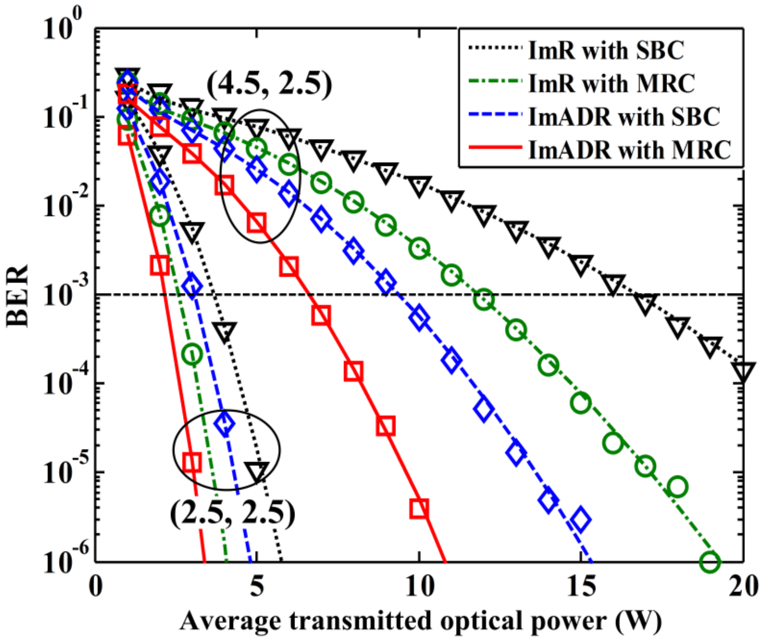

Figure 4.7. BER versus average transmitted optical power. Markers and lines show the simulation and analytical results, respectively.

Fig. 4.8 compares the communication coverage (contours) over the receiving plane for a target BER of 10^{-3} with an average transmitted optical power of 8 W. The coverage contours can be approximated as circles and the coverages are estimated by the areas of the circles.

It can be seen that MRC outperforms SBC, and ImADR with MRC achieves the largest coverage. ImR with MRC attains a coverage diameter of 3.1 m whereas ImADR with MRC attains a coverage diameter of 4.7 m, thus resulting in a coverage improvement of about 130%.

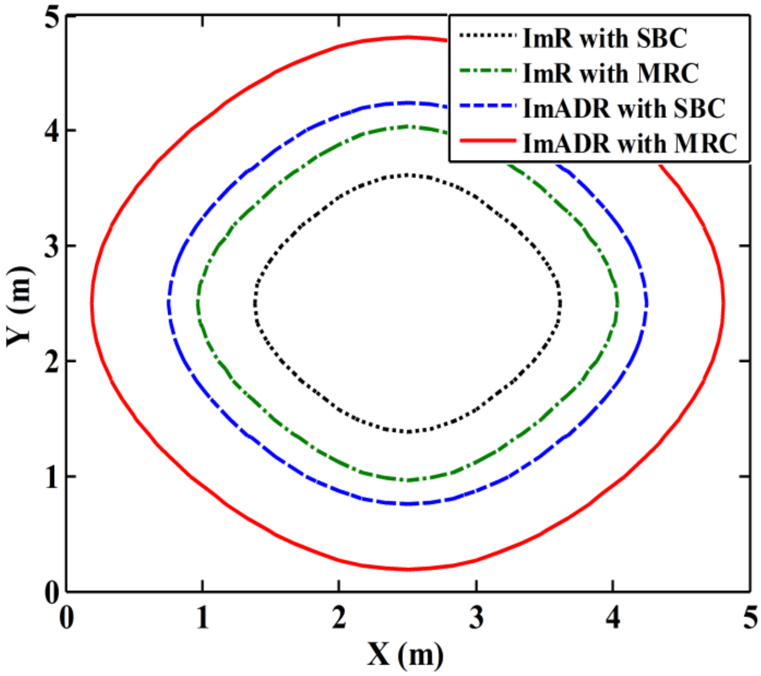

Figure 4.8. Communication coverage comparison for a target BER of 10^{-3} with an average transmitted optical power of 8 W.

4.5 Conclusion

In this chapter, a novel wide-FOV and high-gain ImADR has been proposed and investigated for indoor MIMO-VLC systems. Compared with a conventional ImR using a 2-D circular PD array consisting of vertically oriented PDs, the proposed ImADR utilizes a 3-D spherical-cap-shaped PD array consisting of angle diversity PDs. Moreover, either a common convex lens or an advanced imaging lens such as a fisheye lens can be adopted in the proposed ImADR. Detailed performance comparison between a conventional ImR and an ImADR has been carried out in terms of receiver FOV, area of detector array, optical channel gain and BER. When both ImR and ImADR have the same horizontal size, the ImADR can achieve a much larger FOV than the ImR. To achieve the same FOV of 45°, the ImADR can obtain a 42% reduction in detector array area in comparison to the conventional ImR. Moreover, due to the use of a 3-D spherical-cap-shaped PD array, an optical channel gain improvement of up to 8 dB can be achieved by an ImADR compared with an ImR. Analytical and simulation results have also shown that for a target BER of 10^{-3}, an indoor four-channel MIMO-VLC system using the proposed ImADR achieves 44% reduction in the average transmitted optical power and 130% improvement in the communication coverage area than the same system using a conventional ImR. Therefore, the proposed ImADR is a promising candidate for high-speed indoor MIMO-VLC systems.

Chapter 5 Angle Diversity Multi-Element Receiver for ICI Mitigation in Multi-Cell VLC

5.1 Introduction

In Chapters 3 and 4, advanced modulation and detection techniques have been proposed for indoor MIMO-VLC systems. However, the focus of these techniques is only for performance improvement of single-cell VLC systems. In practical indoor environments, a VLC/MIMO-VLC system usually consists of multiple optical attocells such that the full coverage of an indoor environment can be achieved [18]. It has been shown that inter-cell interference (ICI) is a major issue that severely degrades the overall performance of indoor multi-cell VLC systems [2, 18]. When the users are located at the overlapping area of two or more adjacent cells, the signal-to-interference-and-noise ratio (SINR) of these users would be considerably low due to the existence of strong interference components. In order to efficiently mitigate the ICI and hence improve the overall performance of multi-cell VLC systems, several approaches have been reported in recent years. Kim *et al.* demonstrated a frequency division based carrier allocation approach in [36], where different RF subcarriers are allocated to different cells and electrical filtering is used to extract the desired RF subcarriers for a specific user without being affected by the interference. Although the ICI can be mitigated, the achievable spectral efficiency within each cell is substantially reduced due to spectrum partitioning, as well as the use of a large guard band. An improved carrier allocation approach by using filter bank multicarrier (FBMC) was proposed in [37], where the guard band is greatly reduced because FBMC has considerably suppressed spectrum sidelobes. Nevertheless, the spectral efficiency improvement achieved by reducing the guard band is limited since spectrum partitioning is still required. In [38], Bykhovsky and Arnon proposed an interference-constrained subcarrier reuse algorithm based on discrete multi-tone (DMT) in a heuristic manner, leading to an improvement in the average bit-rate as compared with the conventional DMT method, but with a relatively high implementation complexity. In [39], Ryoo *et al.* demonstrated a differential optical detection approach by employing polarization division, which can reduce the in-band interference and hence avoid the need of spectrum partitioning. However, accurate polarization control and cell planning are required in order to successfully implement this scheme.

In recent years, the use of angle diversity enhanced receivers for performance improvements of VLC systems, especially MIMO-VLC systems, has attracted great attention [104–106]. In this chapter, a novel angle diversity multi-element receiver (ADMER) based ICI mitigation technique is proposed for SINR fluctuation reduction in indoor multi-cell VLC systems [160, 161]. The proposed ADMER consists of N_r detectors (elements), including one top detector and $N_r - 1$ inclined side detectors. A two-cell VLC system using an ADMER with $N_r = 3$ is first experimentally demonstrated and then a four-cell VLC system utilizing four ADMERs with $N_r = 5$, 6, 7 and 9 is analyzed and examined. In the analysis, the impact of receiver random rotation is considered and the performances of four ADMERs are optimized by maximizing the achievable average SINR. The experimental and analytical results both show that the proposed ADMER can effectively mitigate ICI and significantly reduce the SINR fluctuation in indoor multi-cell VLC systems.

The rest of the chapter is organized as follows. In Section 5.2, the principle of the proposed ADMER is first introduced. An experimental demonstration of a two-cell VLC system using an ADMER with $N_r = 3$ is presented in Sections 5.3. A detailed numerical analysis of a four-cell VLC system using four different ADMERs is further conducted in Sections 5.4. Finally, Section 5.5 concludes this chapter. The content of this chapter is related to the author's work reported in [160, 161].

5.2 Principle of ADMER

The proposed ADMER consists of N_r circular-shaped detectors (elements), including one top detector and $N_r - 1$ side detectors. It is assumed that all the detectors have the same radius r, the same half-angle FOV Ψ and the same optical/electrical performance.

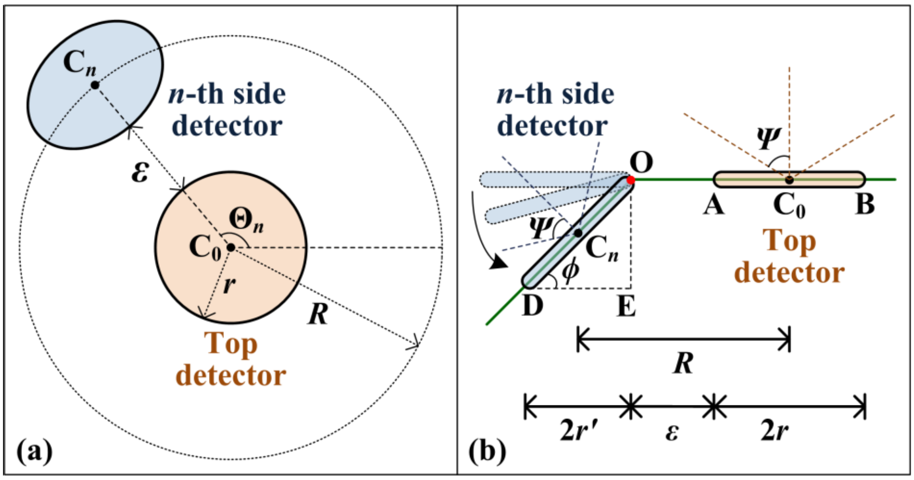

Figure 5.1. (a) Top view and (b) side view of the proposed ADMER. Only the top detector and the n-th side detector are shown for illustration.

The top view and side view of the ADMER are illustrated in Figs. 5.1(a) and (b), respectively. As shown in Fig. 5.1(a), the top detector is located at the central position C_0, while all the side detectors are located at the circumference of a circle that is centered at C_0 with a radius of R. The gap between the top detector and the side detector is ε. The azimuth angle of the n-th side detector is Θ_n. For the ADMER with total N_r detectors, it is assumed that the azimuth angle of the 1-st side detector is fixed at $\Theta_1 = 0°$ and the azimuth angle of the n-th side detector is represented by

$$\Theta_n = 360° \times \frac{n-1}{N_r - 1},\ n = 2,\cdots, N_r - 1. \tag{5.1}$$

For example, the azimuth angles of all four side detectors are 0°, 90°, 180° and 270°, respectively, when $N_r = 5$. Fig. 5.1(b) shows the side view of the top detector and the n-th side detector. As can be seen, the top detector ($n = 0$) is not inclined while the side detector is inclined. In the proposed ADMER, all the side detectors have the same inclination angle ϕ. Assuming that the receiver plane is vertically oriented, the inclination angle of the n-th detector is expressed by

$$\phi_n = \begin{cases} 0°, & \text{if } n = 0 \\ \phi, & \text{if } n = 1,\cdots, N_r - 1 \end{cases}. \tag{5.2}$$

By rotating the side detector around the point O, the inclination angle ϕ of the side detectors can be adjusted. When $\phi = 0°$, the side detectors are not inclined and hence the receiver becomes a multi-element receiver without angle diversity.

It is assumed that the position of the receiver is represented by the central position C_0 of the top detector. Based on the receiver geometry illustrated in Figs. 5.1(a) and (b), the relationship between the position of the top detector and the positions of the side detectors are derived as follows.

The radius R, i.e. the horizontal distance between C_0 and C_n, is given by $R = \varepsilon + r + r'$ and $r' = r\cos\varphi$. Hence, the radius is calculated by $R = \varepsilon + r(1 + \cos\phi)$. Let (x_0, y_0, z_0) and (x_n, y_n, z_n) be the coordinates of positions C_0 and C_n, respectively. After some geometric calculations, the relationship between (x_0, y_0, z_0) and (x_n, y_n, z_n) is given by

$$\begin{cases} x_n = x_0 + [\varepsilon + r(1 + \cos\phi)]\cos\Theta_n \\ y_n = y_0 + [\varepsilon + r(1 + \cos\phi)]\sin\Theta_n \\ z_n = z_0 - r\sin\phi \end{cases}. \tag{5.3}$$

In an indoor multi-cell VLC system, the receiver located at the non-overlapping area of a cell is served by the corresponding cell and not affected by ICI. If the receiver is located at the overlapping area of multiple adjacent cells, usually the specific cell from which the receiver gets the highest SINR is selected [162]. When an ADMER is employed in an indoor multi-cell VLC system, the specific cell that serves the receiver is selected based on the highest SINR obtained by the top detector. Moreover, since the FOVs of two or more detectors in an ADMER could overlap, multiple detectors could simultaneously receive the desired signal for the serving cell.

In order to achieve a final output signal from multiple received signals, diversity combining techniques can be utilized such as equal-gain combining (EGC), select-best combining (SBC), maximal-ratio combining (MRC) and optimum combining (OPC) [162]. Although EGC is the simplest way to combine together the received signals, the SINR performance could be very poor since the interference cannot be suppressed. For SBC, the detector that achieves the highest SINR is selected and hence the interference can be substantially suppressed and the ADMER can achieve a high overall SINR. Due to the existence of interference, MRC is not optimal and the highest SINR can be achieved by OPC that is optimal. However, the implementation complexity of MRC and OPC is relatively high. As a trade-off between the SINR performance and implementation complexity, SBC is adopted for the proposed ADMER.

5.3 Experimental demonstration of a two-cell VLC system

In this section, an indoor two-cell VLC system using the proposed ADMER is experimentally demonstrated, where an ADMER with $N_r = 3$ is considered for ICI mitigation [160].

5.3.1 Experimental setup

Fig. 5.2 illustrates the experimental setup of a two-cell OFDM-VLC system. Two off-the-shelf phosphor-coated white LEDs (Luxeon SP-02) are used as the optical transmitters and the spacing between them is 35 cm. In order to concentrate the light emitted by the LEDs, two lampshades are adopted with the same half-angle FOV of 26°.

Two digital OFDM signals are generated offline by MATLAB with an IFFT size of 256 and 16QAM mapping. Total 64 subcarriers (2nd to 65th) are modulated with data and the other subcarriers are left unmodulated. The CP length is set to 8, which is 1/32 of the IFFT size. A PRBS with 20 bits is utilized for time synchronization and a total of 200 OFDM payload symbols are followed for SINR estimation. The SINR value is estimated from the error vector magnitude (EVM) [37].

Since the 3-dB modulation bandwidth of the LEDs is only about 2 MHz, digital pre-FDE is executed to increase the modulation bandwidth [163].

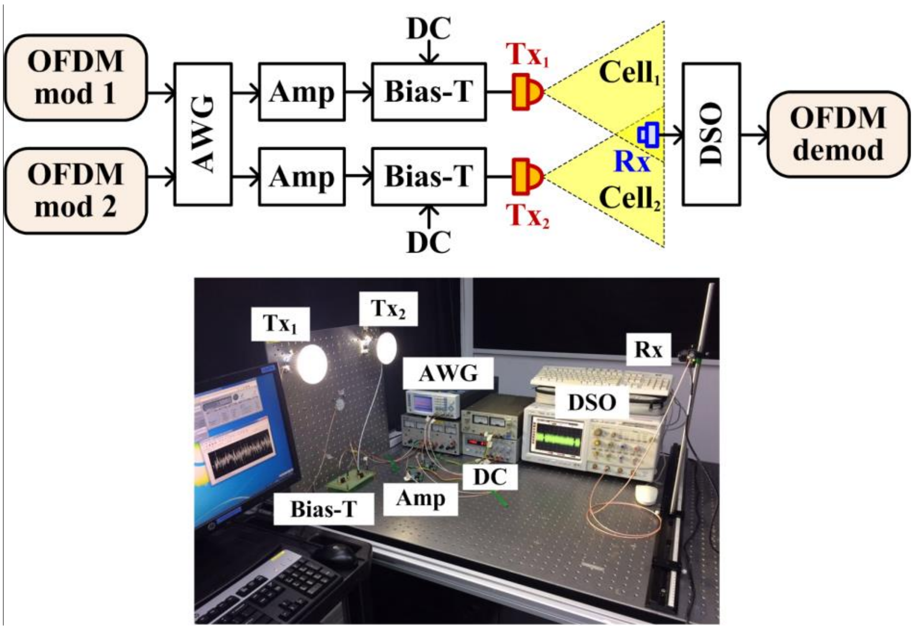

Figure 5.2. Experimental setup of a two-cell OFDM-VLC system.

Two real-valued digital OFDM signals are separately loaded to a multi-channel arbitrary waveform generator (AWG, Tabor WW2074) with a sampling rate of 40 MSa/s and a peak-to-peak voltage of 3 V. Hence, the bandwidth of the OFDM signals is 10 MHz and the raw data rate of each cell is 40 Mb/s.

The analog OFDM signals are amplified and separately superimposed onto 13-V DC bias voltages via two self-designed bias-Tees. The resultant two signals are used to modulate the intensities of two LEDs, respectively. Two adjacent cells corresponding to two LEDs use the same RF spectrum and therefore no spectrum partitioning is performed. The transmission distance is set to 100 cm and the radiated light is captured by a receiver. The received signal is sampled by a digital storage oscilloscope (DSO, Agilent infiniium 54832B) at 1 GSa/s.

Subsequently, the output electrical signal is demodulated offline. The OFDM modulation and demodulation procedures can be found in [163]. The experimental testbed is shown in the photo in Fig. 5.2.

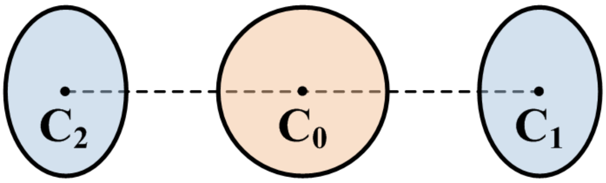

Figure 5.3. Top view of an ADMER with $N_r = 3$.

In this proof-of-concept experiment, an ADMER with $N_r = 3$ is used. Fig. 5.3 depicts the top view of the ADMER with $N_r = 3$. As can be seen, the ADMER consists of one top detector and two side detectors, where the azimuth angles of the two side detector are 0° and 180°.

For the purpose of performance comparison, a single-element receiver (SER) with $N_r = 1$ and a non-angle diversity multi-element receiver (NADMER) with $N_r = 3$ are also considered. The SER is made up of a single uninclined detector consisting of a lens (Thorlabs LA1951-A-ML) with a half-angle FOV of 30°, a blue filter (Thorlabs FD1B) and a PD (Thorlabs PDA36A). The PD has an active area of 13 mm^2 and a 3dB bandwidth of 10 MHz.

Compared with SER, the NADMER comprises multiple uninclined detectors. Due to the lack of an integrated detector array, the NADMER is emulated by adjusting the position of one detector and separately receiving different signals at different positions.

Similarly, the ADMER consists of the same number of detectors as the NADMER. In order to achieve angle diversity, the ADMER is emulated by adjusting both the position and the inclination angle of the detector at different positions. For both NADMER and ADMER, the pitch length is set to 1 cm.

Although the data rate in this demonstration is relatively low, the focus here is to verify the feasibility and effectiveness of ICI mitigation employing ADMER in multi-cell VLC systems. Higher data rate can be achieved by using high-power LEDs and large-bandwidth PDs.

5.3.2 Experimental results

The SINR distribution of the two-cell OFDM-VLC system using an SER is first investigated. The positions of two LED transmitters, i.e., Tx_1 and Tx_2, are set to –17.5 cm and 17.5 cm, respectively. The receiver position offset is assumed to be zero when the receiver is facing the central position of Tx_1 and Tx_2. Due to the geometric symmetry of the system setup, the receiver position offset is set in the range of –17.5 cm to 17.5 cm.

The measured SINR versus receiver position offset is shown in Fig. 5.4. When Tx_1 is on and Tx_2 is off, the highest SINR is 15.8 dB achieved at a receiver position offset of –17.5 cm, i.e., the receiver is directly facing Tx_1. Moreover, the SINR decreases with the receiver moving away from Tx_1, and the SINRs are 15.3 and 3.4 dB when the receiver position offsets are 0 and 7.5 cm, respectively. Due to geometric symmetry, a symmetrical distribution is found when Tx_1 is off and Tx_2 is on.

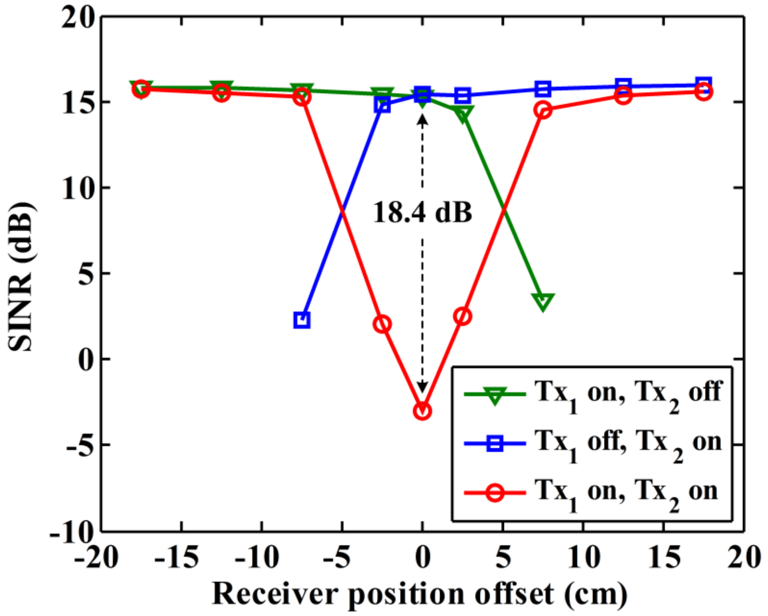

Figure 5.4. Measured SINR versus receiver position offset using an SER.

However, when both Tx_1 and Tx_2 are on, an SINR degradation of 18.4 dB is observed at the receiver position offset of 0 cm and the SINR fluctuation is very high due to ICI. Therefore, it is of great importance to perform efficient ICI mitigation in indoor multi-cell VLC systems.

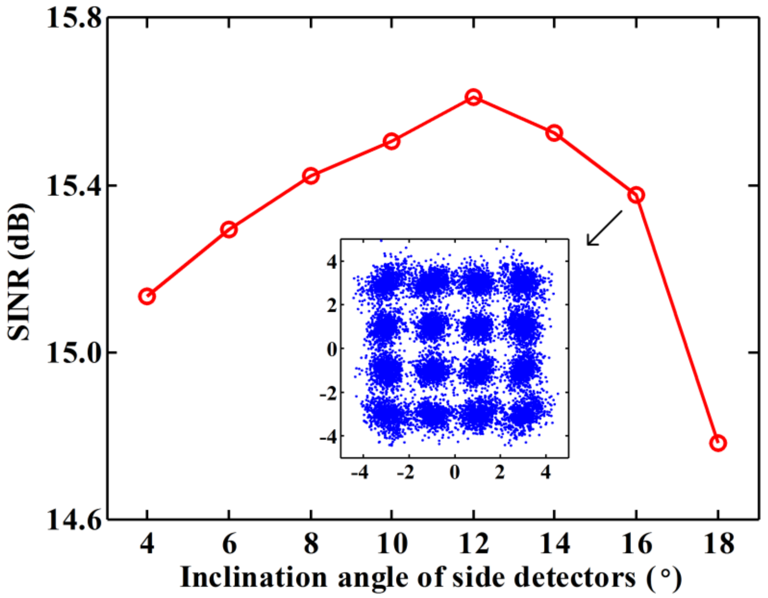

Figure 5.5. Measured SINR versus inclination angle of side detectors in the ADMER.

Since the severest ICI occurs at the receiver position offset of 0 cm, the relationship between the SINR and the inclination angle of side detectors in the ADMER is next examined at the receiver position offset of 0 cm. The side detectors are inclined with an angle in the range of 4° to 18° with a step of 2°.

Fig. 5.5 shows the measured SINR in dB versus the inclination angle of the side detectors in the ADMER with $N_r = 3$. It can be found that the SINR increases with the increase of inclination angle and the maximum SINR is achieved with an inclination angle of 12°. As can be seen, the incident angle is given by arctan (17.5/100) ≈ 10° when an SER is used. Therefore, the LOS optical channel gain corresponding to the signal component is the highest when the inclination angle is 10°, indicating an incident angle of 0°.

However, the best SINR performance is achieved with an inclination angle of 12° instead of 10°. This is because the half-angle FOV of the optical lens is 30° and hence the interference component is un-negligible although the signal component is strongest when the inclination is 10°. In contrast, as the inclination angle is increased to 12°, the received signal power is slightly reduced, but the interference component becomes negligible, resulting in a further SINR improvement. The inset in Fig. 5.5 illustrates the corresponding received 16QAM constellation diagram.

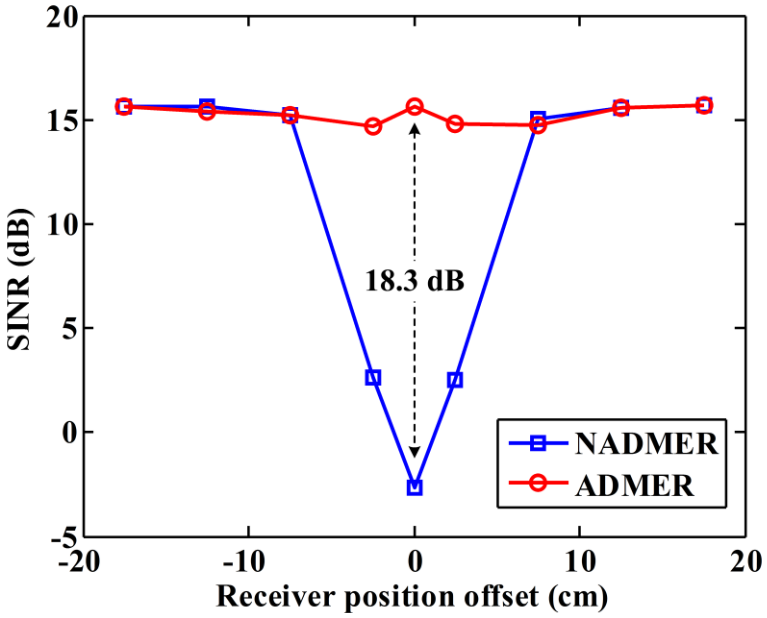

Figure 5.6. Measured SINR versus receiver position offset using NADMER and ADMER.

The SINR performance of the two-cell OFDM-VLC system using a NADMER and an ADMER is further compared. As shown in Fig. 5.6, when using a NADMER, significant SINR degradations are observed within the overlapping area of the two cells due to ICI. Particularly, the achieved SINRs are only –2.63 dB at the receiver position offset of 0 cm.

However, when an ADMER is employed, the SINR performance in the overlapping area is substantially improved. As can be seen, by replacing the NADMER with an ADMER, SINR improvements of 18.3 dB are attained. Moreover, the NADMER and the ADMER can achieve nearly the same SINR performance in the non-overlapping area.

Table 5.1. Experimental SINR performance comparison

SINR (dB)	SER with $N_r = 1$	NADR with $N_r = 3$	ADR with $N_r = 3$
Minimum value	-3.04	-2.63	14.69
Maximum value	15.74	15.67	15.67
Fluctuation	18.78	18.30	0.98

The SINR fluctuation utilizing SER, NADMER and ADMER is also compared. As listed in Table 5.1, the maximum and minimum SINR values using an SER are –3.04 and 15.74 dB, respectively, indicating an SINR fluctuation of 18.78 dB. Moreover, an SINR fluctuation of 18.30 dB is attained when using a NADMER.

However, when an ADMER is used, the SINR fluctuations are reduced to 0.98 dB. Therefore, the SINR distribution of the two-cell OFDM-VLC system can be flattened within only 1 dB of fluctuation by employing an ADMER with $N_r = 3$.

5.4 Numerical analysis of a four-cell VLC system

Here, the SINR performance of an indoor four-cell VLC system using the proposed ADMER is numerically analyzed. Four ADMER structures with $N_r = 5$, 6, 7 and 9 are considered in the analysis, and their respective performances are investigated and compared [161].

5.4.1 System setup

The top view of the proposed ADMER with different number of detectors is shown in Fig. 5.7. The azimuth angle of a side detector is determined by the total number of side detectors in the receiver. The azimuth angle gap between two adjacent side detectors is $\Delta\Theta = 360°/(N_r - 1)$.

It can be found from Fig. 5.7 that the azimuth angle gaps of the receiver with total 5, 6, 7 and 9 detectors are 90°, 72°, 60° and 45°, respectively. As can be seen, the azimuth angle gap is reduced with the increase of the number of side detectors.

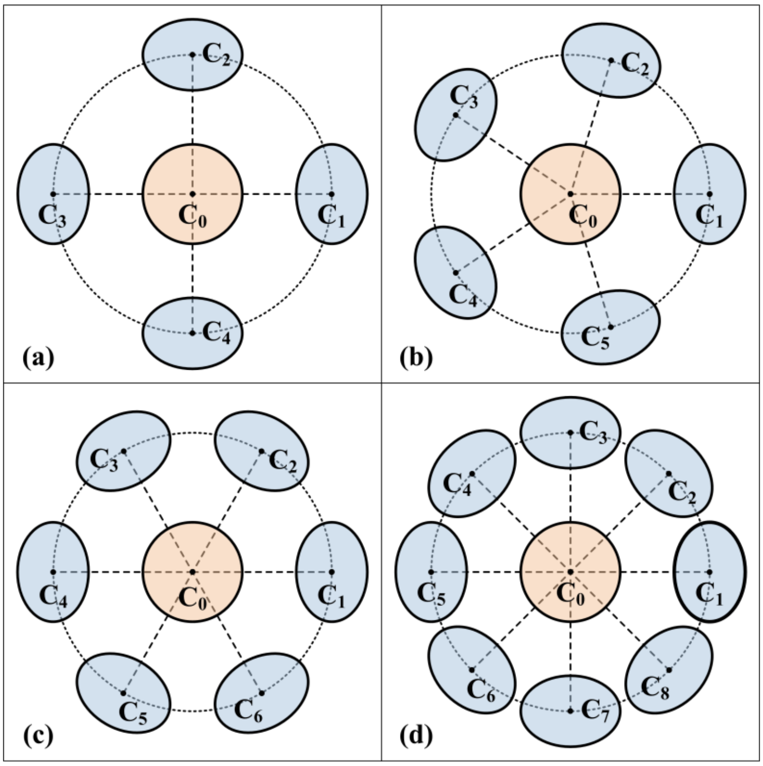

Figure 5.7. Top view of the ADMER with (a) $N_r = 5$, (b) $N_r = 6$, (c) $N_r = 7$ and (d) $N_r = 9$.

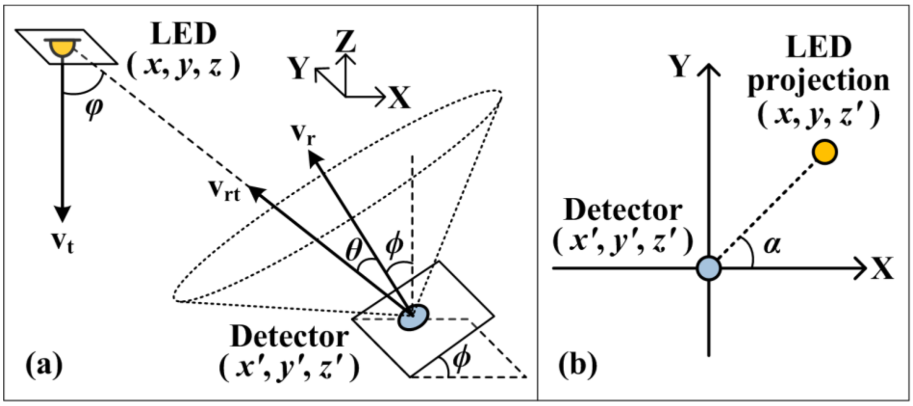

Figure 5.8. (a) Geometry for optical channel gain calculation of the side detectors and (b) LED projection on the detector plane.

In an ADMER, one top detector and multiple inclined side detectors are used. The optical channel gain of the top detector can be obtained by Eq. (2.7). However, the optical channel gain of a side detector cannot be directly obtained by using Eq. (2.7), since all side detectors are inclined with a common inclination angle and each side detector is also rotated with its own azimuth angle. As shown in Fig. 5.8(a), the emission angle φ is determined only by the positions of the LED and the side detector. Assuming that the LED and the side detector are located at (x, y, z) and (x', y', z') respectively, $\cos\varphi$ can be obtained by

$$\cos\varphi = \frac{z - z'}{\left[(x - x')^2 + (y - y')^2 + (z - z')^2\right]^{1/2}}. \tag{5.4}$$

However, the incident angle θ is determined not only by the positions of the LED and the side detector, but also the inclination angle ϕ and the azimuth angle α.

The azimuth angle is given by

$$\alpha = \Theta + \omega, \tag{5.5}$$

where Θ is the initial azimuth angle of the side detector without rotation and ω is the random rotation angle which is the same for all the side detectors and uniformly distributed between 0° and 360° [164].

Let $\mathbf{v}_{\mathrm{r}}$ and $\mathbf{v}_{\mathrm{rt}}$ be the normal vector of the plane of the side detector and the vector from the side detector to the LED, respectively, $\cos\theta$ is given by

$$\cos\theta = \frac{(\mathbf{v}_{\mathrm{r}}, \mathbf{v}_{\mathrm{rt}})}{\|\mathbf{v}_{\mathrm{r}}\| \cdot \|\mathbf{v}_{\mathrm{rt}}\|}, \tag{5.6}$$

where $(\cdot,\cdot)$ denotes the inner product of two vectors and $\|\cdot\|$ is the vector norm. For a detector with an inclination angle ϕ and an azimuth angle α, the normal vector of the detector plane is given by [165]

$$\mathbf{v}_{\mathrm{r}} = [\sin\phi\cos\alpha, \sin\phi\sin\alpha, \cos\phi]. \tag{5.7}$$

The azimuth angle α of the side detector is determined by the positions of the LED projection and the side detector, as shown in Fig. 5.8(b), which is calculated by [146]

$$\alpha = \begin{cases} \alpha_0, & \text{if } x \ge x', y \ge y' \\ \pi - \alpha_0, & \text{if } x < x', y \ge y' \\ \pi + \alpha_0, & \text{if } x < x', y < y' \\ 2\pi - \alpha_0, & \text{if } x \ge x', y < y' \end{cases}, \tag{5.8}$$

where $\alpha_0 = \arctan(|y - y'|/|x - x'|)$. Moreover, the vector from the side detector to the LED is expressed by

$$\mathbf{v}_{\mathrm{rt}} = [x, y, z] - [x', y', z'] = [x - x', y - y', z - z']. \tag{5.9}$$

Therefore, Eq. (5.6) can be rewritten as

$$\cos\theta = \frac{[(x-x')\cos\alpha + (y-y')\sin\alpha]\sin\phi + (z-z')\cos\phi}{\sqrt{(x-x')^2 + (y-y')^2 + (z-z')^2}}. \tag{5.10}$$

By substituting Eq. (5.4) and Eq. (5.10) into Eq. (2.7), the optical channel gain for the side detector is obtained by

$$h(\phi,\Psi) = \frac{(m+1)A_d T(\theta)g(\theta)\{[(x-x')\cos\alpha + (y-y')\sin\alpha]\sin\phi + (z-z')\cos\phi\}(z-z')^m}{2\pi d^2\left[(x-x')^2 + (y-y')^2 + (z-z')^2\right]^{(1+m)/2}}. \tag{5.11}$$

It should be noted that $h(\phi,\Psi)$ becomes zero when the emission angle of larger than the semi-angle at half power of the LED or the incident angle is outside the FOV of the detector. As can be seen, $h(\phi,\Psi)$ is a function of the inclination angle ϕ and the half-angle FOV Ψ of the side detector.

In indoor VLC systems, the primary function of the LEDs is illumination and communication is its secondary function [10]. The illumination performance at a position of the room can be described by the horizontal illuminance, which is defined as

$$E_h = \sum_{i=1}^{N_0} \frac{I_0 \cos^l \varphi_i \cos\theta_i}{d_i^2}, \tag{5.12}$$

where N_0 is the number of LEDs that illuminate this position, I_0 is the maximum luminous intensity of each LED, φ_i and θ_i are the emission and incident angles between the i-th LED and this position, respectively, and d_i is the transmission distance.

After free-space propagation, the light emitted by the i-th LED is detected by the ADMER and the received electrical signal at the output of the j-th detector in the ADMER is represented by

$$y_j(i) = \sum_{i=1}^{N_t} \gamma\xi h_{ij} P_0 x_i(t) + n_j(t), \tag{5.13}$$

where γ is the responsivity of the detector, ξ is the modulation index of the LED, h_{ij} is the optical channel gain, P_0 is the average transmitted optical power of the LED, $x_i(t)$ is the transmitted electrical signal with unit power from the i-th LED, and $n_j(t)$ is the additive noise which includes shot and thermal noises. Both shot and thermal noises can be modeled as real-valued additive white Gaussian noises (AWGNs) and the corresponding variances are given by

$$\begin{cases} \sigma_{shot}^2 = 2q(\gamma P_j + I_{bg} I_2) B_n \\ \sigma_{thermal}^2 = 8\pi k T_K \eta A B_n^2 \left(\dfrac{I_2}{G} + \dfrac{2\pi \Gamma}{g_m} \eta A_d I_3 B_n \right) \end{cases}, \tag{5.14}$$

where $P_j = P_0 \sum_{i=1}^{N_t} h_{ij}$ is the average received optical signal power at the *j*-th detector, I_{bg} is the background current due to ambient light, and B_n is the equivalent noise bandwidth. The other parameters shown in Eq. (5.14) can be found in [12].

Assuming that the *j*-th detector is served by the *i*-th LED, the SINR at the output of the *j*-th detector is expressed by

$$SINR_{ij} = \frac{(\gamma \xi h_{ij} P_0)^2}{\sum_{i'=1, i' \neq i}^{N_t} (\gamma \xi h_{i'j} P_0)^2 + \sigma_{shot}^2 + \sigma_{thermal}^2}, \tag{5.15}$$

where $\sum_{i'=1, i' \neq i}^{N_t} (\gamma \xi h_{i'j} P_0)^2$ represents the electrical power of the interference signal from all the interfering LEDs and σ_{shot}^2 and $\sigma_{thermal}^2$ are the noise variances as defined in Eq. (5.14).

5.4.2 Results and discussions

In this section, the SINR performance of an indoor multi-cell VLC system using the proposed ADMER is analyzed.

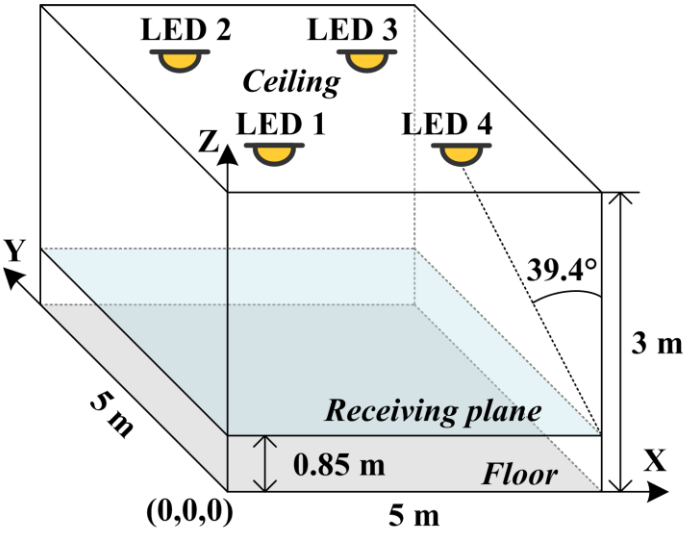

Figure 5.9. Geometric setup of the four-cell VLC system in a 5m×5m×3m room.

The geometric setup of an indoor four-cell VLC system is illustrated in Fig. 5.9. The system is considered in a typical room with a dimension of 5m×5m×3m and and the key parameters of the system setup are listed in Table 5.2.

Four LEDs are mounted in the ceiling and the semi-angle at half power of the LED is 40°. The average transmitted optical power and the modulation index of each LED are 5 W and 0.3, respectively. Each LED has a maximum luminous intensity of 3000 cd. The receiving plane is 0.85 m above the floor. The gains of the optical filter and the optical concentrator are both 1. The receiver plane is assumed to be vertically oriented pointing to the ceiling. The radius of all the circular-shaped detectors is 2.5 mm, corresponding to an active area of 19.6 mm^2. The gap between the top detector and the side detectors is set to 3 mm. The responsivity of all the detectors is 0.53 A/W. A modulation bandwidth of 10 MHz is used and the background current is 5100 µA due to the ambient light.

Table 5.2. Key parameters of system setup

Parameter	**Value**
Room dimension	5m×5m×3m
Locations of four LED arrays	(1.25, 1.25, 3), (1.25, 3.75, 3) (3.75, 3.75, 3), (3.75, 1.25, 3)
Height of receiving plane	0.85 m
Semi-angle at half power of LED	40°
Average transmitted optical power of LED	5 W
Maximum luminous intensity of LED	3000 cd
Modulation index	0.3
Radius of detector	2.5 mm
Gap between top and side detectors	3 mm
Responsivity of detector	0.53 A/W
Modulation bandwidth	10 MHz
Background current	5100 µA

In order to achieve full illumination coverage of the room, as can be seen from Fig. 5.9, the minimum half-angle FOV of the detector is $\Psi_{\min} = 39.4°$.

The illumination performance of the indoor four-cell VLC system is first evaluated by using Eq. (5.12). Fig. 5.10 shows the horizontal illumination distribution around the receiving plane.

As can be seen, the illumination at the positions right below the four LEDs is the highest (~ 650 lx) and it becomes lower when moving towards the corners. Overall, the illumination is above 400 lx for more than 50% of the room area and the illumination for the rest of the room is above 150 lx, which is in accordance with indoor illumination requirements stated in the European lighting standard [166].

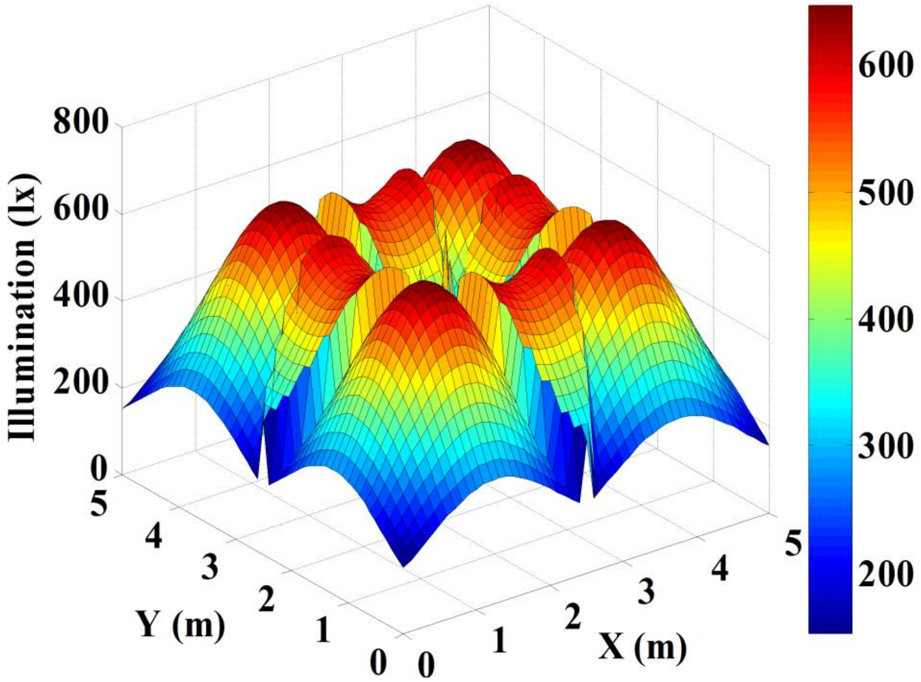

Figure 5.10. Horizontal illumination distribution around the receiving plane.

Under such an illumination environment, the SINR performance of the system is further analyzed by using a single-element receiver (SER) consisting of a single un-inclined detector with a half-angle FOV of 40°.

The SINR distribution around the receiving plane is shown in Fig. 5.11. It is observed that the highest SINR is 26.1 dB that is achieved at the positions right below the four LEDs. Furthermore, the SINR performance in the overlapping area is significantly reduced and the SINR at the center of the receiving plane is the lowest that is –4.8 dB.

Due to the existence of severe ICI, an SINR fluctuation of as high as 30.9 dB is obtained. Hence, substantial performance degradations will occur when the receivers are located at the overlapping area of the indoor four-cell VLC system, which greatly limits the overall SINR performance of the system.

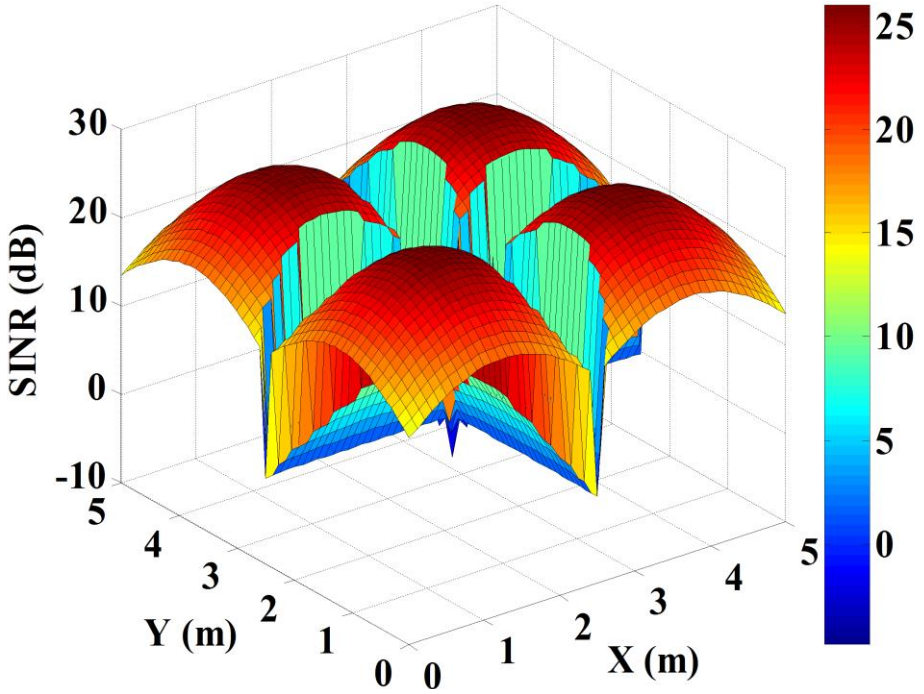

Figure 5.11. SINR distribution around the receiving plane using an SER.

By replacing the SER with the proposed ADMER, the ICI can be mitigated and hence the overall system performance can be improved. As derived in Eq. (5.11), the optical channel gain is a function of the inclination angle ϕ and the half-angle FOV Ψ of the side detectors. Since the SINR is largely dependent on the optical channel gain as given in Eq. (5.15), the ADMER can be optimized by selecting optimal inclination angle ϕ and detector half-angle FOV Ψ that maximize the achievable SINR. Since the center of the receiving plane suffers from the severest ICI, the optimization is then performed at the central position of the receiving plane to find the optimal ϕ and Ψ.

In practical indoor VLC systems, the receiver could have different rotation angles which are assumed to be uniformly distributed between 0° and 360° [164]. In order to optimize the proposed ADMER in a fair and practical way, average SINR is used as the metric of interest in the following optimization. Assuming the ADMER is randomly rotated for total N_ω times and the random rotation angle ω_i ($i = 1, 2, \cdots, N_\omega$) is uniformly distributed between 0° and 360° with a corresponding output SINR of $SINR_i$, the average SINR is given by.

$$SINR_{av} = \frac{1}{N_\omega}\sum_{i=1}^{N_\omega} SINR_i\,. \tag{5.16}$$

As shown in Fig. 5.1(b), the inclination angle ϕ of an ADMER can be adjusted by rotating the side detector around point O and ϕ is in the range between 0° and 90°. Moreover, the half-angle FOV Ψ of all the detectors is another adjustable parameter and the minimum value of Ψ

is 39.4°. Therefore, here it is assumed that the inclination angle $\phi \in [10°, 90°]$ and half-angle FOV $\Psi \in [40°, 80°]$ during the optimization. Based on derivations above, contour plots are used to evaluate the average SINR performance in terms the inclination angle ϕ and the half-angle FOV Ψ of the side detectors in the ADMER.

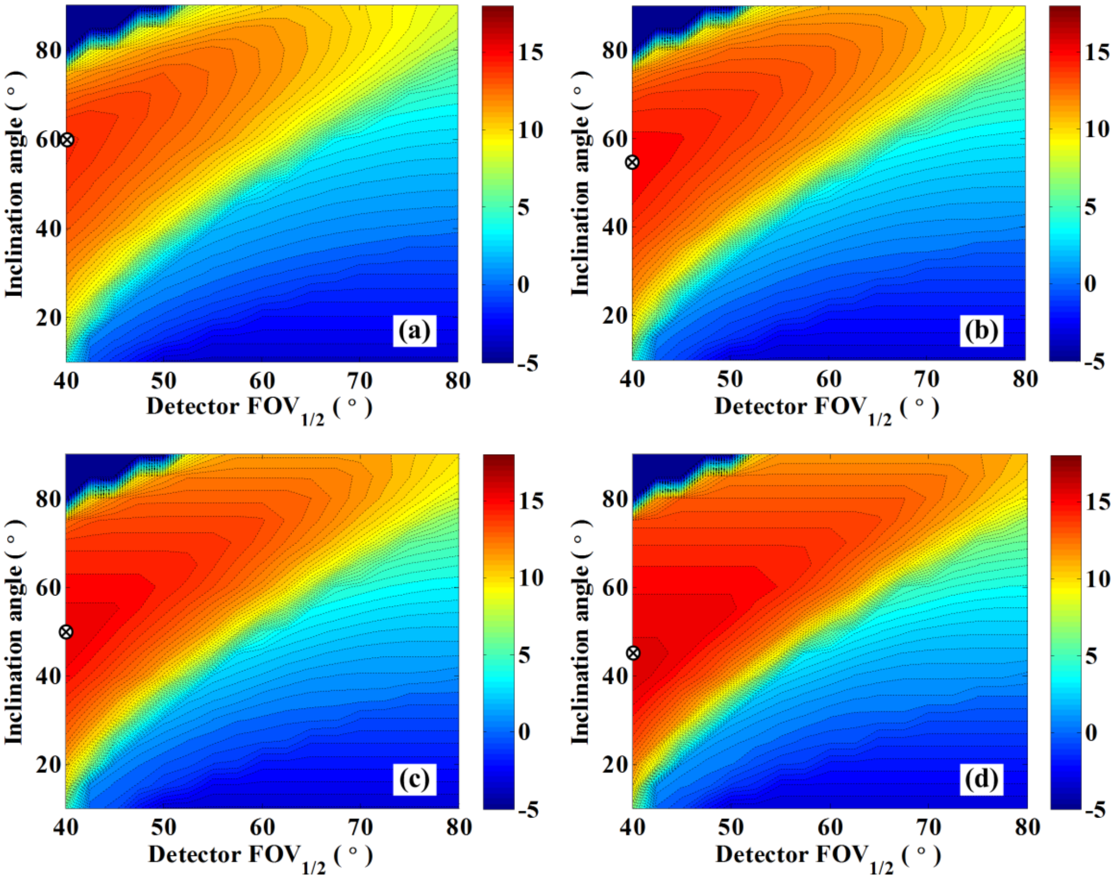

Figure 5.12. Contour plots of average SINR (dB) at the central position of the receiving plane for (a) N_r = 5, (b) N_r = 6, (c) N_r = 7 and (d) N_r = 9.

Figs. 5.12(a) to (d) show the contour plots for $N_r = 5$, 6, 7 and 9, respectively. As can be seen, the average SINR is gradually decreased with the increase of the detector half-angle FOV Ψ for all four cases, indicating that the SINR performance is dominated by the ICI when a larger Ψ is used. Moreover, it is noticed that the optimal inclination angle is getting smaller with more detectors in the ADMER.

The cross markers shown in Fig. 5.12 denote the selected optimal values of ϕ and Ψ for $N_r = 5$, 6, 7 and 9. The optimal half-angle FOVs of all the detectors for $N_r = 5$, 6, 7 and 9 are all set to $\Psi = 40°$, while the optimal inclination angles of the side detectors for $N_r = 5$, 6, 7 and 9 are 60°, 55°, 50° and 45°, respectively.

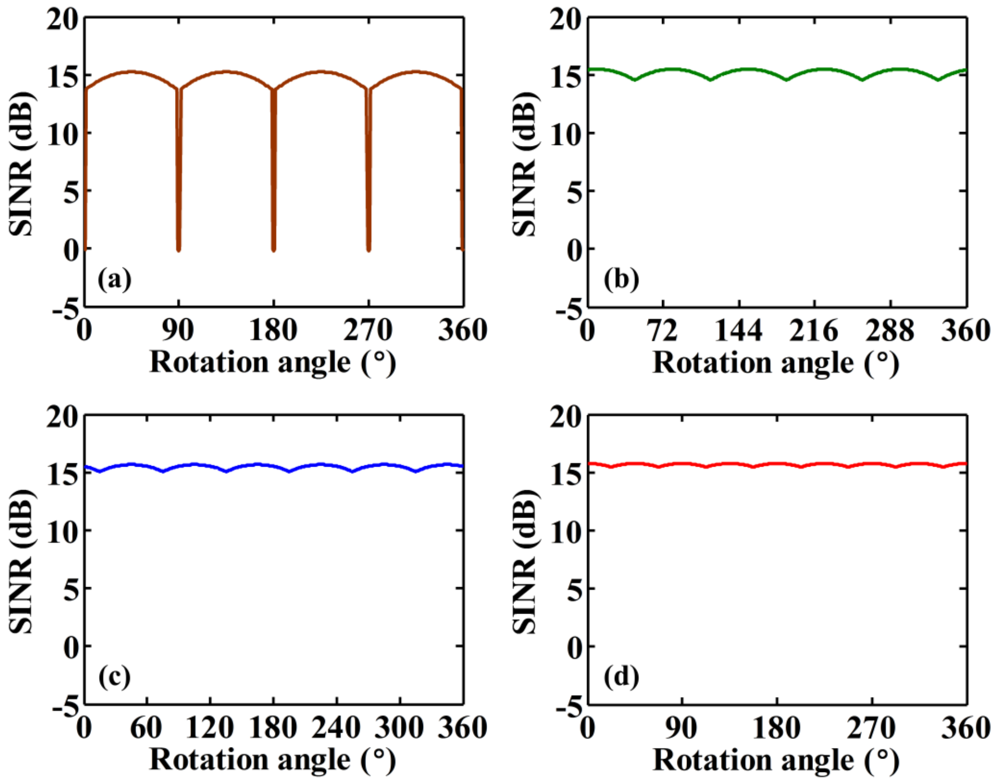

Figure 5.13. SINR versus rotation angle of the ADMER for (a) N_r = 5, (b) N_r = 6, (c) N_r = 7 and (d) N_r = 9.

Based on the obtained optimal parameters, the relationship between the achievable SINR and the rotation angle of the ADMER is next analyzed. Figs. 5.13(a) to (d) show the SINR versus the rotation angle for N_r = 5, 6, 7 and 9, respectively. It can be clearly seen that the SINR fluctuates significantly for N_r = 5 and the minimum SINR is about 0 dB which is achieved when the rotation angles are 0°, 90°, 180° and 270°. The substantial decrease of SINR is due to the geometric symmetry of the ADMER with N_r = 5. When the rotation angles are 0°, 90°, 180° or 270°, the four side detectors of the ADMER with N_r = 5 are all located at the symmetric positions between two adjacent LEDs and thus all the side detectors suffer from severe ICI. However, when N_r is increased to 6, 7 or 9, the symmetry is eliminated and the SINR fluctuation is significantly reduced.

Table 5.3. SINR fluctuation comparison

SINR (dB)	$N_r = 5$	$N_r = 6$	$N_r = 7$	$N_r = 9$
Minimum value	–0.2	14.5	15.1	15.5
Maximum value	15.2	15.5	15.7	15.8
Fluctuation	15.4	1.0	0.6	0.3

The SINR performance for different N_r values is summarized in Table 5.3. As can be seen, the SINR fluctuation for $N_r = 5$ reaches 15.4 dB, while the SINR fluctuation for $N_r = 6$ is only 1 dB, resulting an SINR fluctuation reduction of up to 14.4 dB. In addition, the SINR fluctuation can be further slightly reduced to 0.6 and 0.3 dB for $N_r = 7$ and 9, respectively.

Since the receiver could be randomly rotated with any rotation angles in practical scenarios, the SINR fluctuation needs to be as low as possible. Thus, the option $N_r = 5$ can be excluded. Due to the increased complexity, the options $N_r = 7$ and 9 can also be excluded since nearly the same SINR performance can be achieved with $N_r = 6$. Hence, an ADMER with $N_r = 6$ is the best option for achieving excellent robustness against random rotations in such a four-cell VLC system.

The performance of the four-cell VLC system using different receivers is further compared. The SINR distribution using an SER is shown in Fig. 5.11, where significant SINR fluctuations can be observed. Figs. 5.14 and 5.15 show the average SINR distributions using an ADMER with $N_r = 5$ and 6, respectively. It can be seen that, compared with $N_r = 5$, a relatively smooth and flat average SINR distribution is achieved with $N_r = 6$. As summarized in Table 5.4, the average SINR fluctuation using an SER is up to 30.9 dB. The fluctuation can be reduced to 16.7 and 10.9 dB when an ADMER with $N_r = 5$ and 6 is used, which corresponds to an average SINR fluctuation reduction of 14.2 and 20 dB, respectively.

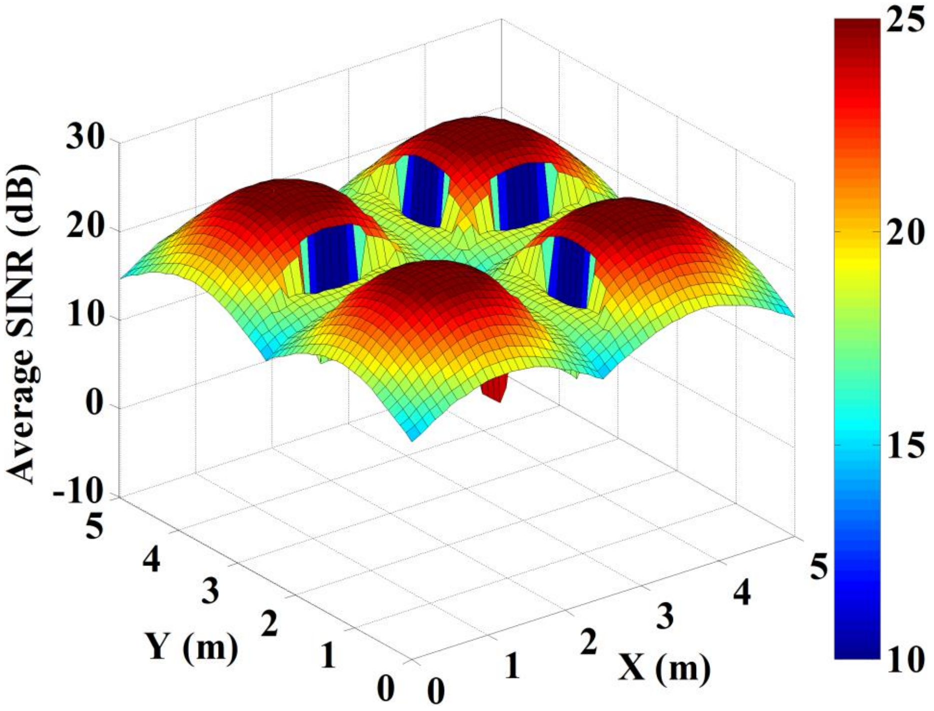

Figure 5.14. Average SINR distribution using an ADMER with $N_r = 5$.

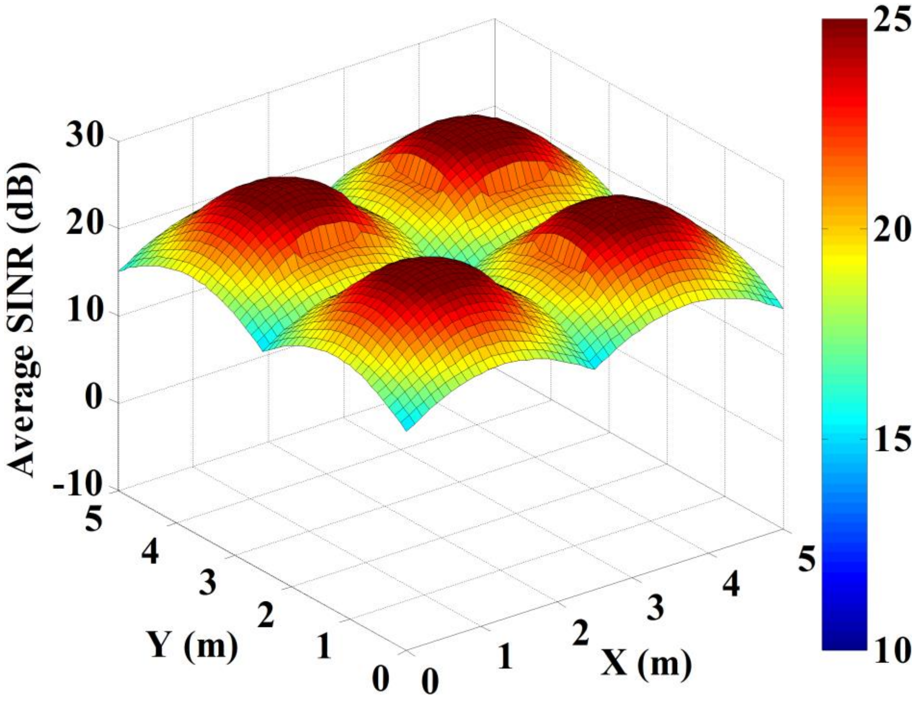

Figure 5.15. Average SINR distribution using an ADMER with $N_r = 6$.

The average SINR distributions using an ADMER with $N_r = 7$ and 9 are not shown since they are nearly the same as $N_r = 6$. In conclusion, an ADMER with $N_r = 6$, i.e., including one top detector and five side detectors, is also the best option for ICI mitigation and average SINR fluctuation reduction.

Table 5.4. Average SINR fluctuation comparison

Average SINR (dB)	$N_r = 1$	$N_r = 5$	$N_r = 6$
Minimum value	–4.8	9.4	15.2
Maximum value	26.1	26.1	26.1
Fluctuation	30.9	16.7	10.9

5.5 Conclusion

In this chapter, an ADMER has been proposed and investigated for efficient ICI mitigation and SINR fluctuation reduction in indoor multi-cell VLC systems. The performance of indoor multi-cell VLC systems using the proposed ADMER has been evaluated by both proof-of-concept experiment and numerical analysis. Since no spectrum partitioning is required, an indoor multi-cell VLC system using the proposed ADMER enabled ICI mitigation technique can achieve a much higher spectral efficiency than that utilizing the conventional frequency division based techniques. In the analysis, totally four ADMER structures have been studied and further optimized by maximizing the achievable average SINR with the consideration of receiver random rotation. It has been shown by the analytical results that an indoor four-cell VLC system employing an ADMER with six detectors (each detector has a half-angle FOV of 40° and all side detectors have an inclination angle of 55°) achieves an SINR fluctuation no more than 1 dB for different receiver rotation angles at the central position of the receiving plane and reduces the average SINR fluctuation from 30.9 to 10.9 dB around the receiving plane, compared with the system utilizing an SER. In conclusion, the proposed ICI mitigation technique with the use of ADMER has high potential for future high data rate indoor multi-cell VLC systems.

Chapter 6 Integration of VLC and OFDM-PON Based on Adaptive Envelope Modulation

6.1 Introduction

Several modulation and detection techniques have already been proposed for performance improvement of VLC systems in the previous chapters. However, as a high-speed indoor wireless communication technology, VLC becomes an important part in future indoor access networks. Next generation access networks are expected to provide high-speed hybrid wired and wireless services for end users [19, 167]. Due to its cost-effectiveness, high capacity and easy upgradability, passive optical network (PON) has been considered as a promising candidate for high-speed wired access [20, 168, 169]. In recent years, OFDM based PON (OFDM-PON) has attracted tremendous attention, since OFDM has high spectral efficiency, excellent robustness to chromatic dispersion and flexibility of dynamic bandwidth allocation [47, 170, 171]. Moreover, RF based technologies have been widely investigated for wireless access, including WiFi [172], WiMax [173] and radio-over-fiber (RoF) [174–176]. However, the capacity of widely used WiFi and WiMax is very limited and the RoF systems only have a license-free bandwidth of about 7 GHz in the 60 GHz frequency region. Furthermore, RF radiation inevitably produces severe EMI which is strictly prohibited in many indoor areas such as hospitals and aircraft cabins [7].

As a promising alternative and complementary technology to RF based indoor wireless communication, white LEDs enabled VLC has revealed great potential for providing high-speed and EMI-free wireless access in indoor environments [21, 27]. Therefore, it is of great significance to integrate VLC with PON systems to achieve high-speed hybrid wired and wireless indoor optical access for end users. So far, only several integration schemes have been reported in literature. In [41, 42], an integrated PON and VLC system was demonstrated based on a multiband single-carrier frequency domain equalization (SC-FDE) modulation technique. The signals for wired and wireless access are carried by different subbands and an electrical low-pass filter (LPF) is used to separate the wired signal and wireless signal in each optical network unit (ONU). In [43], a high-speed VLC based local area network (LAN) was demonstrated where multiband OFDM and electrical filtering are used for supporting multiple VLC access points. Moreover, a bidirectional network combining VLC and the time-wavelength-division-multiplexed PON (TWDM-PON) was proposed in [44] where VLC encoding and decoding are digitally performed in the gateway based on multiband OFDM. Moreover, a service-integrated OFDM-PON system was proposed based on an on-off keying (OOK) overlaid OFDM modulation [45], where the low-speed OOK signal for wireless access is overlaid on the envelope of the high-speed OFDM signal for wired access and no electrical filtering is required. Nevertheless, the envelope of the OFDM signal fluctuates significantly due to the high peak-to-average power ratio (PAPR) which introduces inherent amplitude distortion to the overlaid OOK signal. In addition, since each OOK symbol is encoded to the envelope of one OFDM symbol, the OOK signal has the same symbol rate as the OFDM signal which might not be compatible with practical indoor VLC links.

In this chapter, an adaptive envelope modulation technique is proposed for the integration of variable-rate VLC and OFDM-PON for hybrid wired and wireless indoor optical access [179]. The data for wired access is carried by a conventional OFDM signal and the data for VLC wireless access is carried by an *M*-ary pulse amplitude modulation (*M*-PAM) signal which is modulated onto the envelope of the OFDM signal. In order to achieve a constant envelope and eliminate the inherent amplitude distortions of the conventional OFDM signal [45], a constant envelope OFDM (CE-OFDM) signal is generated by performing discrete phase modulation after conventional OFDM encoding [48, 177, 178]. By adaptively modulating the wireless *M*-PAM signal onto the flat envelope of the wired CE-OFDM signal, signals for hybrid wired and wireless indoor optical access can be seamlessly integrated. Furthermore, variable-rate VLC wireless access can be successfully achieved by employing the adaptive envelope modulation technique in the optical line terminal (OLT).

The rest of the chapter is organized as follows. In Section 6.2, the principle of the proposed integrated VLC and OFDM-PON system is first introduced. Performance analysis of wired access and VLC wireless access are presented in Sections 6.3 and 6.4, respectively. Finally, Section 6.5 concludes this chapter. The content of this chapter is related to the author’s work shown in [179, 180].

6.2 System integration

In this Section, the principle of the integrated VLC and OFDM-PON system is introduced. The system architecture is first presented and then two key techniques, i.e., CE-OFDM and adaptive envelope modulation, are discussed.

6.2.1 System architecture

Fig. 6.1 illustrates the conceptual diagram of the integrated VLC and OFDM-PON system for hybrid wired and wireless indoor optical access. The signal coming from the OLT passes through an optical fiber and a residential gateway is used to distribute the signal to the ONUs.

In each ONU, wired services can be accessed by connecting optical fibers, and wireless services can be accessed through indoor VLC by using white illumination LEDs in the ceiling.

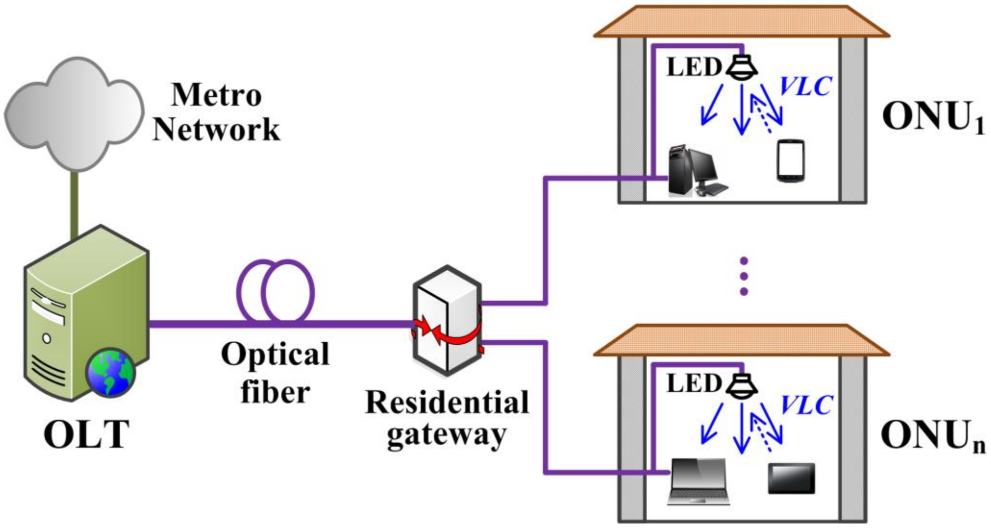

Figure 6.1. Conceptual diagram of the integrated VLC and OFDM-PON system.

The architecture of the integrated VLC and OFDM-PON system is shown in Fig. 6.2. In the OLT, the wired input data are encoded into a CE-OFDM signal. After adding a DC bias, a unipolar CE-OFDM signal is obtained. The wireless input data are modulated onto the envelope of the unipolar CE-OFDM signal through adaptive envelope modulation, where the wireless input data are first encoded into an M-PAM signal before envelope modulation. As a result, the wired input data and the wireless input data are simultaneously carried by the envelope-modulated CE-OFDM signal. The digital signal is further converted to an analog signal via digital-to-analog conversion (D/A) and the resultant signal is used to drive a laser diode (LD).

After being transmitted over a single mode fiber (SMF), the optical signal is broadcasted to all the ONUs through an optical splitter (OS). As shown in ONU$_1$, the optical signal for wired access is received by a fast/high-bandwidth photodiode (PD) in which the envelope-modulated CE-OFDM signal is fully detected. After analog-to-digital conversion (A/D), the digital signal is fed into a CE-OFDM demodulator to generate the wired output data. As shown in ONU$_2$, the optical signal for indoor VLC wireless access is received by a slow/low-bandwidth PD in which envelope detection is performed and only the overlaid M-PAM signal is detected. A DC bias is added to the M-PAM signal and the obtained unipolar M-PAM signal is used to drive an LED lamp. After indoor free-space transmission, the light is concentrated by a lens and then detected by a PD. The wireless output data are generated via A/D conversion and PAM demodulation. It should be noted that no optical or electrical filters are used in the ONUs and the signals for wired access and wireless access are separated by using two PDs with different bandwidths. Moreover, the detailed characteristics of the LD, fast PD, slow PD, etc., are not specified, because our focus here is to verify the feasibility of the proposed integrated VLC and OFDM-PON based on adaptive envelope modulation.

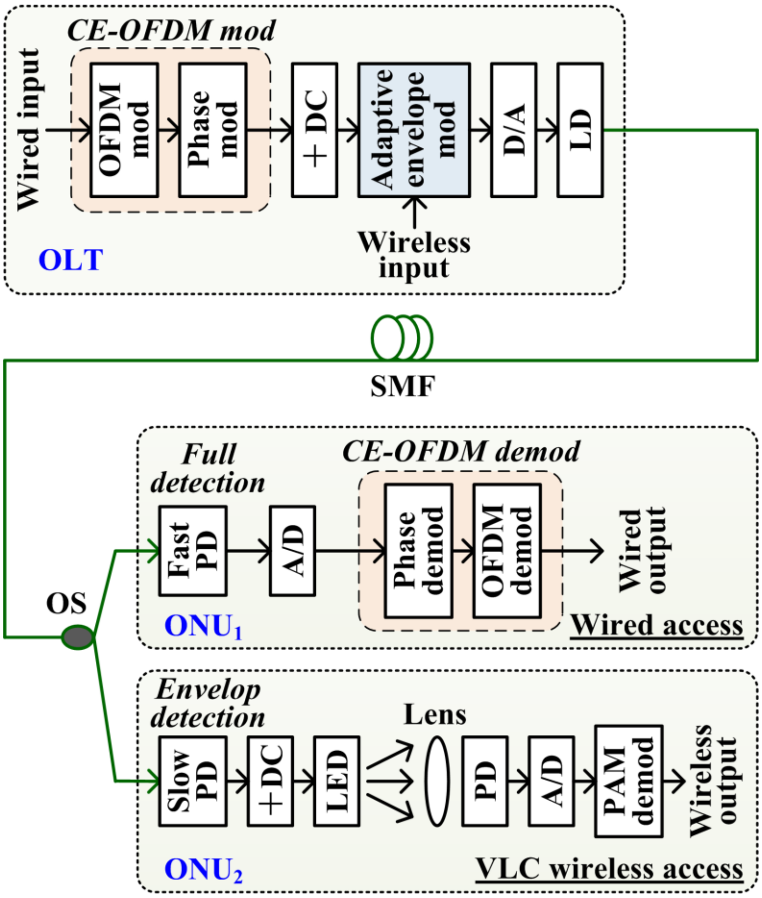

Figure 6.2. Architecture of the integrated VLC and OFDM-PON system.

6.2.2 Constant envelope OFDM

Instead of conventional OFDM which usually has a relatively large PAPR, the CE-OFDM scheme is adopted in the integrated VLC and OFDM-PON system thanks to its constant envelope characteristic.

In the CE-OFDM modulator, as shown in Fig. 6.2, the wired input data are first fed into a conventional OFDM modulator and thus a real-valued bipolar OFDM signal is generated. Then, the resultant OFDM signal is used to modulate the phase of a local oscillator (LO) in a phase modulator, resulting in a bipolar CE-OFDM signal which can be represented by [48]

$$S_{\mathrm{bi}}(t)=\mathrm{R}\left\{Ae^{j\varphi(t)}e^{j2\pi f_{\mathrm{c}}t}\right\}=A\cos\left[2\pi f_{\mathrm{c}}t+\varphi(t)\right], \tag{6.1}$$

where A is the signal amplitude, f_c is the carrier frequency of the LO and $\varphi(t)$ is the phase signal. During the i-th symbol, $\varphi(t)$ is given by

$$\varphi(t) = \mu_e C_N m_i(t) + \theta_i, \tag{6.2}$$

where $\mu_e = 2\pi h$ is the electrical modulation index, C_N is a normalizing constant, $m_i(t)$ is the OFDM signal in the i-th symbol and θ_i is a memory term which is set to make the modulation phase-continuous [48, 177, 178].

In the CE-OFDM demodulator, as shown in Fig. 6.2, the received CE-OFDM signal is first phase-demodulated to recover the conventional OFDM signal which is then demodulated in a conventional OFDM modulator to obtain the wired output data.

6.2.3 Adaptive envelope modulation

The principle of adaptive envelope modulation is shown in the inset in Fig. 6.3. In order to perform adaptive envelope modulation, a non-negative or unipolar CE-OFDM signal is first generated by adding a DC bias to the bipolar CE-OFDM signal which is given by

$$S_{\mathrm{uni}}(t) = S_{\mathrm{bi}}(t) + \mathrm{DC} = A\cos\left[2\pi f_c t + \varphi(t)\right] + \mathrm{DC}. \tag{6.3}$$

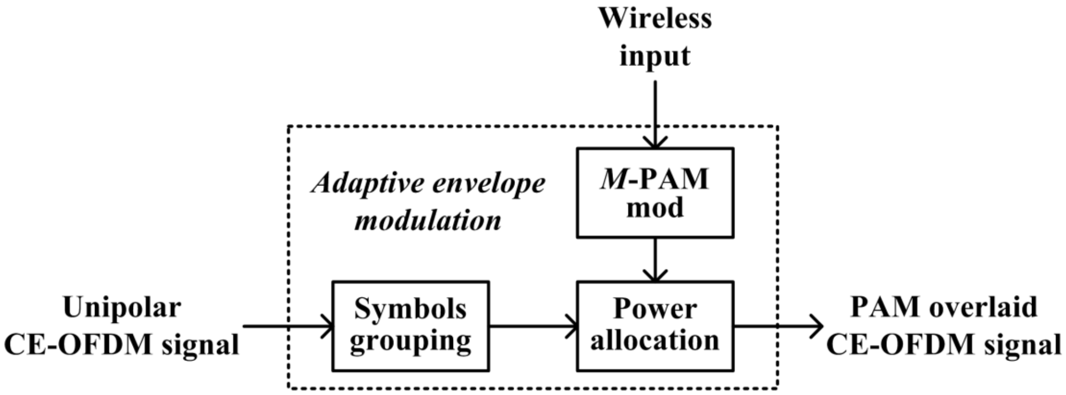

Figure 6.3. Principle of adaptive envelope modulation.

In the adaptive envelope modulation, as shown in Fig. 6.3, multiple consecutive unipolar CE-OFDM symbols are grouped together via symbols grouping and the power of each CE-OFDM symbol group is determined by the M-PAM encoded wireless input data via power allocation.

After performing adaptive envelope modulation, an M-PAM overlaid CE-OFDM signal is obtained which simultaneously carries the OFDM signal for wired access and the M-PAM signal for VLC wireless access.

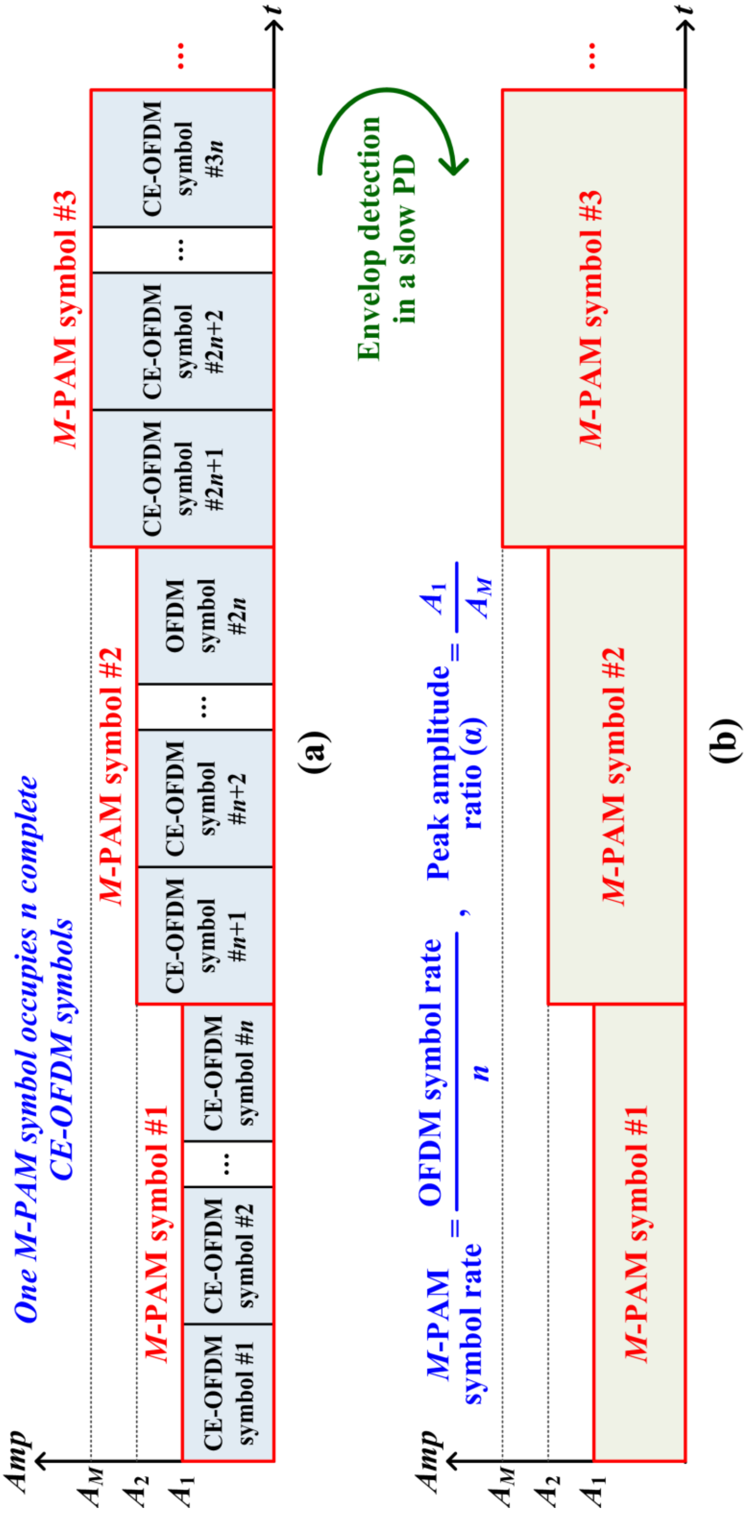

Figure 6.4. Time traces of (a) *M*-PAM overlaid CE-OFDM signal after adaptive envelope modulation and (b) the obtained *M*-PAM signal after envelope detection in a slow PD.

Fig. 6.4(a) illustrates the time trace of the M-PAM overlaid CE-OFDM signal. As can be seen, n consecutive CE-OFDM symbols form one CE-OFDM symbol group and each CE-OFDM symbol group represents one M-PAM symbol, i.e., one M-PAM symbol occupies n complete CE-OFDM symbols. For the M-ary PAM modulation, the peak amplitude A_i of each CE-OFDM symbol group takes values from the discrete set $\{A_1, A_2, \cdots, A_M\}$ with $M \geq 2$, which can be represented by

$$A_i = A_1 + \frac{i-1}{M-1}(A_M - A_1), \tag{6.4}$$

where A_1 and A_M are the lowest and highest peak amplitudes of all the CE-OFDM symbol groups, respectively. Assuming that $DC = A$, as can be seen from Eq. (6.3), the highest peak amplitude is given by $A_M = 2A$. Here, the peak amplitude ratio between the lowest peak A_1 and the highest peak A_M is defined as

$$\alpha = \frac{A_1}{A_M}. \tag{6.5}$$

Since $0 \leq A_1 \leq A_M$, the peak amplitude ratio is then $0 \leq \alpha \leq 1$. Based on Eq. (6.4) and Eq. (6.5), A_i can be rewritten by

$$A_i = \frac{K_i}{M-1} A_M, \tag{6.6}$$

Where $K_i = \alpha M - 1 + (1 - \alpha)i$. The time trace of the obtained M-PAM signal after envelope detection in a slow/low-bandwidth PD is shown in Fig. 6.4(b). Since one M-PAM symbol occupies n consecutive CE-OFDM symbols, the relationship between the symbol rate of the M-PAM signal, $R^{\mathrm{s}}_{M\text{-PAM}}$, and the symbol rate of the CE-OFDM signal, $R^{\mathrm{s}}_{\text{CE-OFDM}}$, is given by

$$R^{\mathrm{s}}_{M\text{-PAM}} = \frac{R^{\mathrm{s}}_{\text{CE-OFDM}}}{n}. \tag{6.7}$$

For a fixed $R^{\mathrm{s}}_{\text{CE-OFDM}}$, $R^{\mathrm{s}}_{M\text{-PAM}}$ can be adjusted by varying the value of n.

6.3 Performance analysis of wired access

In this section, the performance of wired access in the integrated VLC and OFDM-PON system is analyzed and evaluated. Generalized BER expressions of both the CE-OFDM signal with M-PAM overlay and the overlaid unipolar M-PAM signal are first derived.

In the integrated system, the received CE-OFDM signal is directly demodulated to obtain the wired output data, while the received M-PAM signal is further processed before VLC wireless transmission.

Generally, there are two ways to process the received M-PAM signal: one is to amplify the signal [42] and the other is to decode and regenerate the signal [44]. Although the former is simpler than the later, much better performance can be achieved by the latter since the errors caused by optical fiber transmission can be corrected by utilizing forward error correction (FEC) coding and hence error propagation from optical fiber transmission to VLC wireless transmission can be eliminated [44]. Due to its enhanced error performance, the latter is adopted in the following analysis.

The BER of the CE-OFDM signal with M-PAM overlay for wired access is first analyzed in subsection 6.3.1. To optimize the overall performance of the integrated system, the BER of the overlaid M-PAM signal without VLC wireless transmission is then analyzed in subsection 6.3.2. Performance trade-off between the CE-OFDM signal with M-PAM overlay and the overlaid M-PAM signal without VLC wireless transmission is further investigated in subsection 6.3.3.

6.3.1 BER of CE-OFDM signal with *M*-PAM overlay

Making use of a high carrier-to-noise ratio (CNR) approximation, i.e., CNR $\geq$ 10 dB as discussed in [48], the BER of M_0-ary QAM based bipolar CE-OFDM signal over an AWGN channel can be approximated by

$$BER_{\text{CE-OFDM}}^{\text{bi}} \approx \frac{2\left(\sqrt{M_0}-1\right)}{\sqrt{M_0}\log_2\sqrt{M_0}} \mathrm{Q}\left(\mu_{\mathrm{e}}\sqrt{\frac{6SNR_{\mathrm{bi}}}{M_0-1}}\right), \tag{6.8}$$

where Q(·) is the Q-function and SNR_{bi} is the electrical SNR per symbol of the bipolar CE-OFDM signal. Since real-valued and oversampled OFDM signals are generally transmitted in IM/DD based optical systems, the input to the IFFT is a conjugate-symmetric and zero-padded data vector. The power of the bipolar carrier is calculated by $\frac{1}{\mathrm{T}}\int_0^{\mathrm{T}} S_{\mathrm{bi}}^2(t)dt = \frac{A^2}{2}$ and the CNR of a bipolar CE-OFDM signal without M-PAM overlay is given by [48]

$$CNR_{\mathrm{bi}} = \frac{A^2/2}{B_{\mathrm{n}}N_0}, \tag{6.9}$$

where B_n is the noise bandwidth and N_0 is the noise power spectrum density. Given an oversampling factor J, the electrical SNR of the bipolar CE-OFDM signal can be calculated by [178, p. 67]

$$SNR_\mathrm{bi} = JCNR_\mathrm{bi} = \frac{JA^2}{2B_\mathrm{n}N_0}. \tag{6.10}$$

After adding a DC bias A, a unipolar CE-OFDM signal $S_\mathrm{uni}(t)$ is obtained with $A_M = 2A$ and the power of the unipolar carrier is calculated by $\frac{1}{\mathrm{T}}\int_0^\mathrm{T} S_\mathrm{uni}^2(t)dt = \frac{3A^2}{2}$. Hence, the SNR of the unipolar CE-OFDM signal $SNR_\mathrm{uni}(t)$ can be similarly calculated by

$$SNR_\mathrm{uni} = JCNR_\mathrm{uni} = J\frac{3A^2}{2B_\mathrm{n}N_0} = \frac{3JA_M^2}{8B_\mathrm{n}N_0} = 3SNR_\mathrm{bi}. \tag{6.11}$$

As can be seen from Eq. (6.11), the electrical SNR of the unipolar CE-OFDM signal is thrice as high as that of the bipolar CE-OFDM signal, which is proportional to the square of A_M for a given oversampling factor J and a fixed noise power $B_\mathrm{n}N_0$.

In the following analysis, the electrical SNR of the unipolar CE-OFDM signal SNR_uni is adopted as a common metric to evaluate and compare the BER performance of the received CE-OFDM signal and the overlaid M-PAM signal.

Replacing SNR_bi in Eq. (6.8) with SNR_uni, the BER of the M_0-QAM based unipolar CE-OFDM signal is approximately given by

$$BER_\text{CE-OFDM}^\mathrm{uni} \approx \frac{2\left(\sqrt{M_0}-1\right)}{\sqrt{M_0}\log_2\sqrt{M_0}} \mathrm{Q}\left(\mu_\mathrm{e}\sqrt{\frac{2SNR_\mathrm{uni}}{M_0-1}}\right). \tag{6.12}$$

After adaptive envelope modulation, the unipolar CE-OFDM signal is overlaid with a low-speed M-PAM signal and the peak amplitude of each CE-OFDM symbol group is given by Eq. (6.6). Hence, the electrical SNR of CE-OFDM symbols with the peak amplitude of A_i can be expressed by

$$SNR_\text{CE-OFDM}^i = \frac{3JA_i^2}{8B_\mathrm{n}N_0} = \left(\frac{K_i}{M-1}\right)^2 \frac{3JA_M^2}{8B_\mathrm{n}N_0}. \tag{6.13}$$

Based on Eq. (6.11), $SNR_\text{CE-OFDM}^i$ can be rewritten as

$$SNR_\text{CE-OFDM}^i = \left(\frac{K_i}{M-1}\right)^2 SNR_\mathrm{uni}. \tag{6.14}$$

Substituting Eq. (6.14) into Eq. (6.12) yields the corresponding BER

$$BER^{i}_{\text{CE-OFDM}} \approx \frac{2\left(\sqrt{M_0}-1\right)}{\sqrt{M_0}\log_2\sqrt{M_0}} \mathrm{Q}\left(\frac{\mu_e K_i}{M-1}\sqrt{\frac{2SNR_{\text{uni}}}{M_0-1}}\right). \tag{6.15}$$

Assuming that all the constellation points of M-PAM encoding are equiprobable, the overall BER of the M_0-QAM based CE-OFDM signal with M-PAM overlay can be expressed by

$$BER_{\text{CE-OFDM}} = \frac{1}{M}\sum_{i=1}^{M} BER^{i}_{\text{CE-OFDM}} . \tag{6.16}$$

Monte Carlo simulations are performed to verify the validity of the theoretical derivations over an AWGN channel. In the simulations, it is assumed that a 4PAM signal is overlaid on the envelope of a 64QAM based CE-OFDM signal. The FFT size is 256 and the oversampling factor is 2. The symbol rate of the CE-OFDM signal is assumed to be 10 GS/s and the electrical modulation index of the CE-OFDM signal is set to 0.8. Totally, 4000 symbols are transmitted over the AWGN channel and collected for BER calculation.

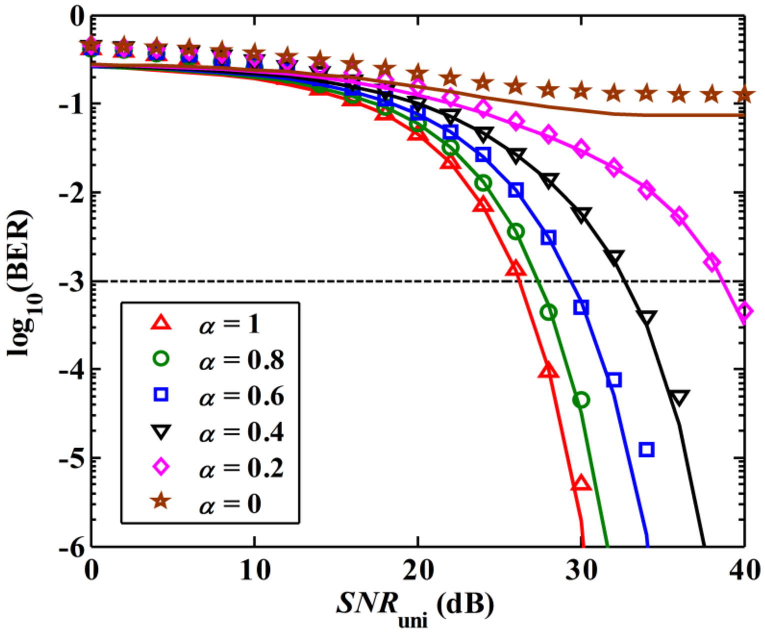

Figure 6.5. BER versus electrical SNR of the unipolar CE-OFDM signal for 64QAM based CE-OFDM signal with 4PAM overlay. Markers and lines show the simulation and theoretical results, respectively.

Fig. 6.5 shows the BER performance of the 64QAM based CE-OFDM signal with 4PAM overlay for different peak amplitude ratios. The solid lines show the theoretical results based on Eq. (6.16), while the markers give the simulation results. It is observed that the simulation results agree well with the theoretical ones when the electrical SNR is relatively large. However, for a small electrical SNR which also indicates a smaller CNR, the theoretical expression becomes less accurate due to its precondition of high CNR.

It is also found out that the best BER performance is attained when the peak amplitude ratio is 1 (i.e., no *M*-PAM overlay). With the decrease of the peak amplitude ratio, the BER performance gets worse and an error floor around BER = 10^{-1} exhibits when the peak amplitude ratio is 0. Hence, in order to achieve a good performance of the *M*-PAM overlaid CE-OFDM signal, a high peak amplitude ratio should be considered.

6.3.2 BER of overlaid *M*-PAM signal without VLC wireless transmission

Following the steps given in [181, p. 163-164], the BER expression of the overlaid *M*-PAM signal without VLC wireless transmission is further derived.

The amplitude of the unipolar *M*-PAM signal is obtained in Eq. (6.6) and therefore the constellation of the overlaid unipolar *M*-PAM signal can be designed as

$$C_i = (i-1)l, \ \ i = 1, 2, \cdots, M, \tag{6.17}$$

where *l* is the distance between two nearest constellation points and it is given by

$$l = \frac{A_M - A_1}{M-1} = \frac{1-\alpha}{M-1} A_M. \tag{6.18}$$

Then, the BER of the *M*-PAM signal over an AWGN channel is computed by [181, p. 163]

$$BER_{M\text{-PAM}} = \frac{2(M-1)}{M\log_2 M} \mathrm{Q}\left(\sqrt{\frac{l^2}{2N_0}}\right). \tag{6.19}$$

Since all *M*-PAM constellation points have an identical probability, the average symbol energy for the *M*-PAM signal is given by

$$E_\mathrm{S} = \frac{1}{M}\sum_{i=1}^{M} \mathrm{C}_\mathrm{i}^2 = \frac{l^2}{M}\sum_{i=1}^{M} (i-1)^2 . \tag{6.20}$$

Thus, replacing *l* in Eq. (6.19) with E_S, the BER can be written as

$$BER_{M\text{-PAM}} = \frac{2(M-1)}{M\log_2 M} \mathrm{Q}\left(\sqrt{\frac{MSNR_\mathrm{av}}{2\sum_{i=1}^{M}(i-1)^2}}\right)$$

$$=\frac{2(M-1)}{M\log_2 M}\mathrm{Q}\left(\sqrt{\frac{3SNR_{\mathrm{av}}}{(M-1)(2M-1)}}\right), \tag{6.21}$$

where $SNR_{\mathrm{av}} = E_{\mathrm{S}}/N_0$ is the average electrical SNR of the overlaid M-PAM signal. Note that Eq. (6.21) is equivalent to the BER expression of the unipolar M-PAM signal obtained in [182].

Following Eq. (6.13), the electrical SNR of the overlaid M-PAM signal for the constellation point C_i can be defined by

$$SNR^{i}_{M\text{-PAM}}=\frac{JC_i^2}{B_{\mathrm{n}}N_0}=\left(\frac{1-\alpha}{M-1}\right)^2(i-1)^2\frac{JA_M^2}{B_{\mathrm{n}}N_0}. \tag{6.22}$$

According to Eq. (6.11), $SNR^{i}_{M\text{-PAM}}$ can be rewritten as

$$SNR^{i}_{M\text{-PAM}}=\frac{8}{3}\left(\frac{1-\alpha}{M-1}\right)^2(i-1)^2 SNR_{\mathrm{uni}}. \tag{6.23}$$

Thus, the average electrical SNR of the overlaid unipolar M-PAM signal is obtained as

$$\begin{aligned}SNR^{\mathrm{av}}_{M\text{-PAM}}&=\frac{1}{M}\sum_{i=1}^{M}SNR^{i}_{M\text{-PAM}}\\&=\frac{4(1-\alpha)^2(2M-1)}{9(M-1)}SNR_{\mathrm{uni}}.\end{aligned} \tag{6.24}$$

Substituting Eq. (6.24) into Eq. (6.21) yields the overall BER of the overlaid unipolar M-PAM signal

$$BER_{M\text{-PAM}}=\frac{2(M-1)}{M\log_2 M}\mathrm{Q}\left(\frac{1-\alpha}{M-1}\sqrt{\frac{4}{3}SNR_{\mathrm{uni}}}\right). \tag{6.25}$$

The BER performance of the overlaid 4PAM signal is shown in Fig. 6.6. Based on Eq. (6.25), it can be seen that the theoretical results (shown as solid lines) closely match the simulation results (shown as the markers).

In contrast to the 4PAM overlaid CE-OFDM signal, the lowest BER is achieved for a given electrical SNR when the peak amplitude ratio is 0. The BER gets higher when the peak amplitude ratio is increased and the BER will reach 0.5 when the peak amplitude ratio is 1.

Therefore, a relatively low peak amplitude ratio should be used to guarantee a good performance of the overlaid *M*-PAM signal.

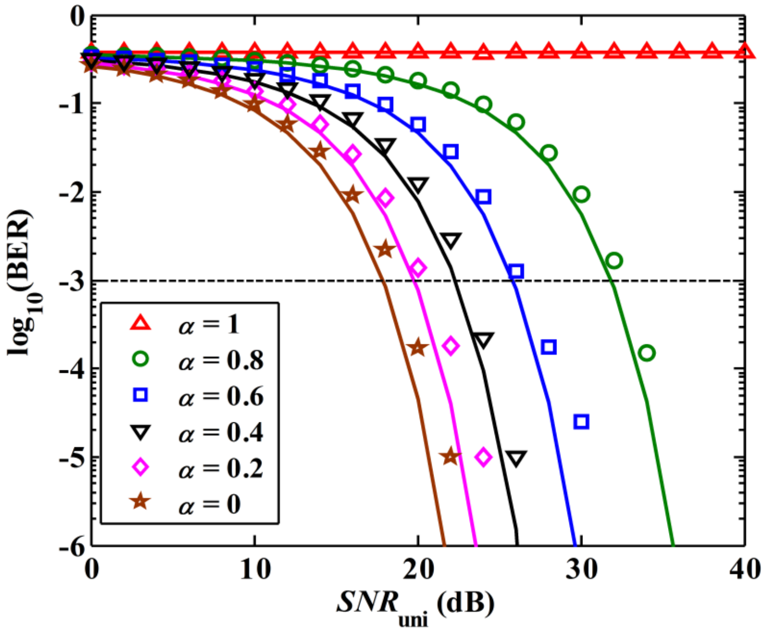

Figure 6.6. BER versus electrical SNR of the unipolar CE-OFDM signal for the overlaid 4PAM signal without VLC wireless transmission. Markers and lines show the simulation and theoretical results, respectively.

6.3.3 Performance trade-off

Based on the analysis above, it can be concluded that there is a BER performance trade-off between the *M*-PAM overlaid CE-OFDM signal and the overlaid *M*-PAM signal without VLC wireless transmission.

In order to optimize the overall performance of the integrated VLC and OFDM-PON system, the peak amplitude ratio should be optimized and a reasonable optimization condition is to achieve equal BER for both the M_0-QAM based CE-OFDM signal with *M*-PAM overlay and the overlaid *M*-PAM signal without VLC wireless transmission.

Based on Eq. (6.16) and Eq. (6.25), it can be seen that the BER of the M_0-QAM based CE-OFDM signal with *M*-PAM overlay is a function of multiple variables including M_0, M, μ_e, SNR_{uni} and α, while the BER of the overlaid *M*-PAM signal is determined by the variables including M, SNR_{uni} and α.

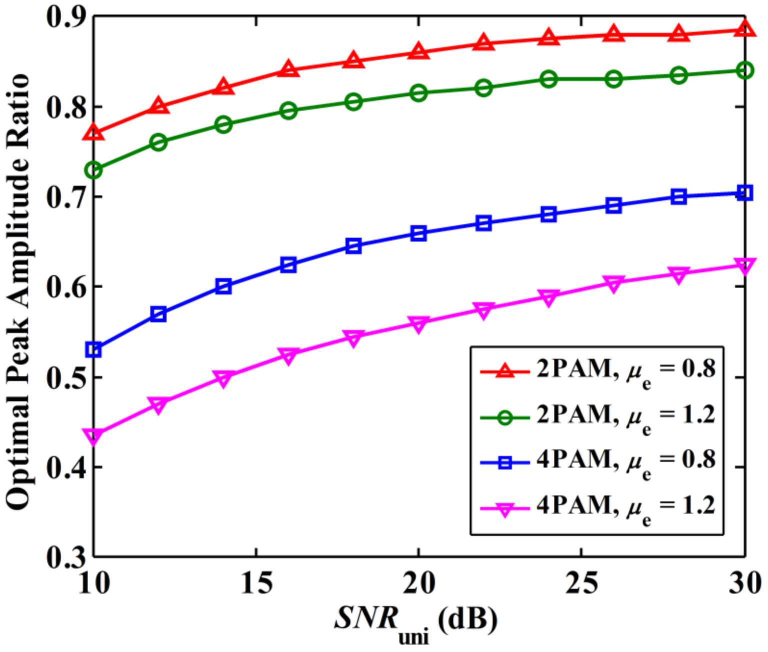

Figure 6.7. Optimal peak amplitude ratio versus electrical SNR of the unipolar CE-OFDM signal for 64QAM based CE-OFDM signal with *M*-PAM overlay.

The optimized peak amplitude ratio, α_{opt}, is next examined by using the following parameters: $M_0 = 64$, $M = 2$ or 4, and $\mu_e = 0.8$ or 1.2. Fig. 6.7 shows the relationship between the optimal peak amplitude ratio and the electrical SNR. As can be seen in Fig. 6.7, the optimal peak amplitude ratio increases with the electrical SNR, and the optimal peak amplitude ratio for the case of 4PAM overlay is relatively lower than that for the case of 2PAM overlay. Furthermore, a smaller μ_e results in a higher optimal peak amplitude ratio.

Based on the results shown in Fig. 6.7, the optimal peak amplitude ratio to reach the BER benchmark for the integrated OWC and OFDM-PON system can be obtained. Assuming that a BER of 10^{-3} is set as the benchmark, the required SNR for the 64QAM based CE-OFDM signal with 4PAM overlay and $\mu_e = 0.8$ is about 27.4 dB, and thus the corresponding optimal peak amplitude ratio is found to be 0.69.

Therefore, the performance of the integrated system can be optimized by selecting an optimal peak amplitude ratio. In addition, the peak amplitude ratio can be set to the optimal value when VLC wireless transmission is activated (awake). However, when VLC wireless transmission is deactivated (sleep), the peak amplitude ratio can be set to 1 so as to reduce the required electrical SNR for wired access. By adaptively switching the value of peak amplitude ratio between its optimal value and 1, the energy efficiency of the integrated system can be substantially improved.

6.4 Performance analysis of VLC wireless access

Since the errors caused by optical fiber transmission are corrected before VLC wireless transmission, an error-free *M*-PAM signal is superimposed onto a DC bias, as shown in ONU_2 in Fig. 6.2, and the combined signal is used to drive a white LED. After propagating through an indoor optical wireless channel, the light is concentrated by an optical lens which is further detected by a PD. The resultant electrical *M*-PAM signal is demodulated to obtain the wireless output data.

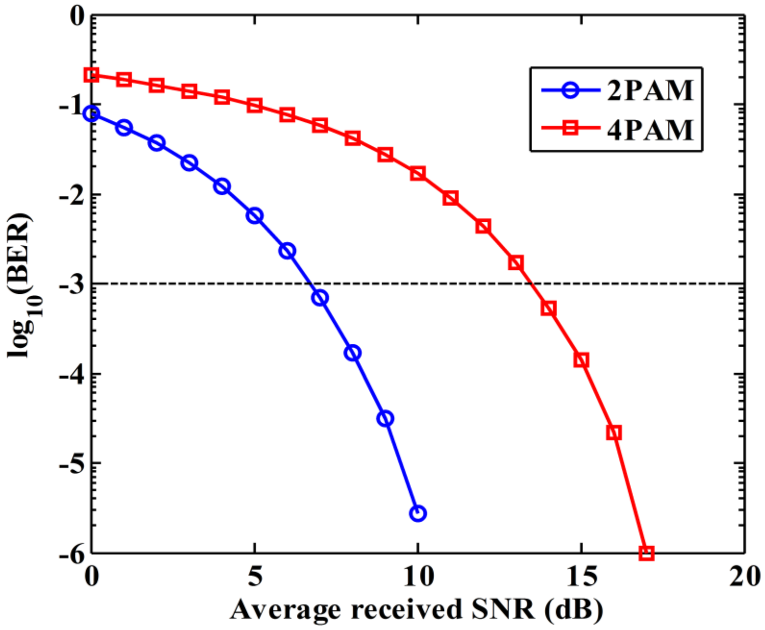

Figure 6.8. BER versus average received SNR for *M*-PAM based indoor VLC wireless access.

The BER performance of *M*-PAM based indoor VLC wireless access is evaluated via Monte Carlo simulations with $M = 2$ and 4. The distance is set to be 3 m. The LED and the PD are located at the center of the ceiling and the floor, respectively. The other simulation parameters can be found in Table I of [145]. Fig. 6.8 shows the BER versus received SNR for *M*-PAM based VLC wireless access. As can be seen, 2PAM requires a received SNR of about 6.7 dB to reach the BER benchmark of 10^{-3}, while a received SNR of about 13.5 dB is required for 4PAM.

In practical indoor environments, the data rate of VLC wireless access might not be constant all the time. For example, the data rate of VLC wireless access is affected by many factors such as user mobility and dimming control [21]. Since the achievable data rate of VLC wireless access is variable in real implementation of VLC systems, the proposed adaptive envelope modulation technique which can support variable-rate VLC wireless access is highly desirable to fully exploit the capacity of indoor VLC systems.

As shown in Fig. 6.4(b), the symbol rate of the overlaid M-PAM signal after adaptive envelope modulation is determined by Eq. (6.7) and the achievable bit rate of the overlaid M-PAM signal, $R^{\mathrm{b}}_{M\text{-PAM}}$, is expressed by

$$R^{\mathrm{b}}_{M\text{-PAM}} = R^{\mathrm{s}}_{M\text{-PAM}} \log_2 M = \frac{R^{\mathrm{s}}_{\text{CE-OFDM}} \log_2 M}{n}. \tag{6.26}$$

It can be seen that the achievable bit rate of the overlaid M-PAM signal is linearly proportional to $R^{\mathrm{s}}_{\text{CE-OFDM}}$ and $\log_2 M$, which is also inversely proportional to the value of n. In practical scenarios, $R^{\mathrm{s}}_{\text{CE-OFDM}}$ can be assumed as a fixed value, thus M and n are the two parameters that can be adaptively adjusted to achieve variable-rate VLC wireless access. Since $R^{\mathrm{s}}_{\text{CE-OFDM}}$ is assumed to be 10 GS/s, according to Eq. (6.26), the achievable bit rate in the unit of Mb/s is then given by $10^4 \log_2 M / n$.

Fig. 6.9 depicts the relationship between the achievable bit rate and the value of n for different PAM orders. Taking 8PAM for example, the achievable bit rate varies from 200 to 1000 Mb/s when the value of n is changed from 150 to 30. Therefore, by changing M or n, variable bit rate indoor VLC wireless access can be achieved.

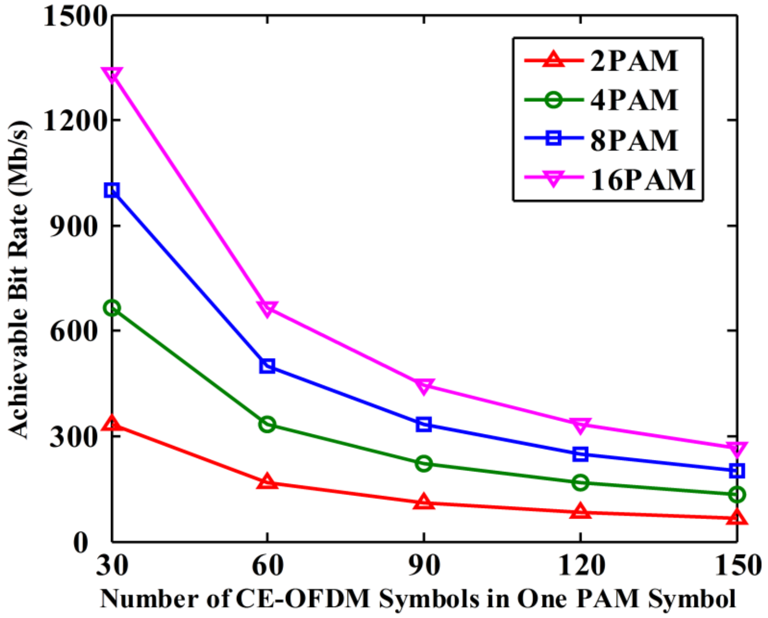

Figure 6.9. Achievable bit rate of indoor VLC wireless access versus the number of CE-OFDM symbols in one PAM symbol.

6.5 Conclusion

In this chapter, an integrated variable-rate VLC and OFDM-PON system has been proposed and investigated where signals for both wired and wireless access are converged in the OLT and simultaneously delivered to each ONU over an optical fiber, by employing an adaptive envelope modulation technique. Electrical or optical filtering is not required in the ONUs and two PDs with different bandwidths are employed to separate the different signals. The data for wired access is carried by a conventional OFDM signal and discrete phase modulation is performed to convert the conventional OFDM signal into a CE-OFDM signal, while the *M*-PAM encoded data for wireless VLC access is modulated onto the envelope of the CE-OFDM signal. Generalized BER expressions of the CE-OFDM signal with *M*-PAM overlay and the overlaid *M*-PAM signal have been derived and further verified by Monte Carlo simulations. Analytical and simulation results have shown that there is a performance trade-off between the *M*-PAM overlaid CE-OFDM signal for wired access and the overlaid *M*-PAM signal for wireless VLC access. By selecting an optimal peak amplitude ratio, the overall performance of the integrated VLC and OFDM-PON system can be optimized. Moreover, by employing the adaptive envelope modulation technique, variable-rate VLC wireless access has also been achieved in the integrated VLC and OFDM-PON system. Therefore, the proposed integrated variable-rate VLC and OFDM-PON system can be a potential candidate for future high-speed indoor optical access networks

Chapter 7 Conclusions and Future Work

7.1 Conclusions

This thesis includes the investigations of four aspects of advanced modulation and detection techniques for indoor VLC systems, which are very promising to provide high-speed wireless access to indoor users.

In chapter 3, a NHS-OFDM modulation scheme is proposed for indoor MIMO-VLC systems. By transmitting the real and imaginary parts of a complex-valued OFDM signal via a pair of LEDs, the Hermitian symmetry constraint is circumvented in the proposed NHS-OFDM. The performance of an indoor MIMO-VLC system employing NHS-OFDM is evaluated by both numerical analysis and proof-of-concept experiments. The performance of conventional HS-OFDM is also investigated for the purpose of comparison. The analytical results have shown that a 2×2 MIMO-VLC system using NHS-OFDM exhibits lower or comparable computational complexity as the 2×2 MIMO-VLC system using conventional HS-OFDM, but achieves superior BER performance. The experimental results have further verified that, for a target BER of 3.8×10^{-3}, NHS-OFDM improves the communication coverage area of a 400 Mb/s imaging 2×2 MIMO-VLC system by about 30% compared with HS-OFDM.

In chapter 4, a wide-FOV and high-gain ImADR is proposed and investigated for indoor MIMO-VLC systems. Either a common convex lens or an advanced imaging lens such as a fisheye lens can be adopted in the ImADR. Analytical and simulation results have revealed that for a target BER of 10^{-3}, a four-channel MIMO-VLC system using the proposed ImADR achieved 44% reduction in the average transmitted optical power and 130% improvement in the communication coverage than the system using a conventional ImR.

In chapter 5, an ADMER is proposed and evaluated for efficient ICI mitigation and SINR fluctuation reduction in indoor multi-cell VLC systems. The performance of indoor multi-cell VLC systems using the proposed ADMER has been evaluated by both experiment and numerical analysis. Since no spectrum partitioning is required, an indoor multi-cell VLC system using the proposed ADMER enabled ICI mitigation technique can achieve a much higher spectral efficiency than the multi-cell VLC system using conventional frequency division based techniques. Both experimental and analytical results have shown that the proposed ADMER can efficiently mitigate ICI and significantly reduce SINR fluctuation reduction in either an indoor two-cell or four-cell VLC system.

In chapter 6, an integrated variable-rate VLC and OFDM-PON system is proposed and investigated by using adaptive envelope modulation. Electrical or optical filtering is not required in the ONUs and two PDs with different bandwidths can be employed to separate the different signals. Generalized BER expressions of the CE-OFDM signal with M-PAM overlay and the overlaid M-PAM signal have been derived, which have been further verified by Monte Carlo simulations. The BER performances of wired access and indoor VLC wireless access have been analyzed, and variable-rate indoor VLC wireless access has also been successfully achieved to support different QoS requirements of indoor users.

7.2 Future work

In this thesis, four aspects of advanced modulation and detection techniques for performance improvement of indoor VLC systems have been proposed and investigated. In the analytical and simulation investigations in this thesis, the systems are configured with idea conditions. For example, only the LOS components are considered and the LEDs are assumed to have linear power-current (P-I) curves. In the future work, practical considerations in the directions where the research lead to will be the main focus. Besides the techniques introduced in this thesis, the following topics are worth to be studied and explored in the future work.

In Chapter 4, an ImADR was proposed for communication coverage improvement of indoor MIMO-VLC systems, and the system performance was evaluated by numerical analysis and Monte Carlo simulations. In Chapter 5, an ADMER was proposed for ICI mitigation in multi-cell VLC systems and the system performance was evaluated by proof-of-concept experiment and numerical analysis. For both ImADR and ADMER, the receiver performance is largely dependent on the corresponding detector array. As a result, it is of great importance to design and develop integrated detector arrays for the implementation of the proposed ImADR and ADMER in practical VLC systems.

In Chapter 6, an integrated VLC and OFDM-PON system was proposed based on adaptive envelope modulation and its performance was evaluated by numerical analysis and Monte Carlo simulations. However, the practical feasibility of such an integrated system has not been verified experimentally. Hence, it is necessary to conduct a verification experiment to demonstrate the feasibility of the integrated VLC and OFDM-PON system. Moreover, novel schemes using advanced modulation and detection techniques need to be further developed and demonstrated for seamless integration of VLC with last-mile optical access networks.

A practical VLC system should be able to simultaneously support multiple users at the same time in typical indoor environments. Therefore, it is necessary to develop efficient multiple access techniques for indoor multi-user VLC systems. Recently, several advanced multiple access techniques such as non-orthogonal multiple access (NOMA) in power domain or code domain have attracted great attention. However, the application of NOMA is VLC systems has not been adequately studied in the literature. Potential topics such as power application methods for NOMA based MIMO-VLC systems or NOMA based multi-cell VLC systems will be considered and investigated. It would be a very interesting topic to mitigate inter-user-interference (IUI) and inter-cell-interference (ICI) in a joint manner for indoor multi-user multi-cell VLC systems.

Besides illumination and high-speed wireless data communication, LEDs also have many other emerging applications in both indoor and outdoor environments such as positioning, networking, sensing, ranging and detecting. Specifically, indoor visible light positioning (VLP) using existing illuminating LEDs in the ceiling has attracted great attention in recent years. So far, many algorithms have been introduced for VLP systems such as received signal strength (RSS), time of arrival (ToA), time difference of arrival (TDoA), phase difference of arrival (PDoA), angle of arrival (AoA), etc. To further improve the positioning accuracy and the system coverage, more advanced algorithms will be proposed for indoor VLP systems and proof-of-concept experiments will also be carried out. Moreover, the integration of VLC and VLP systems will be further considered and an integrated visible light communication and positioning (VLCP) system will be developed in the future.

Author's Publications

Journal

[1] **Chen Chen**, Wen-De Zhong, and Dehao Wu, "On the coverage of multiple-input multiple-output visible light communications [invited]," *IEEE/OSA Journal of Optical Communications and Networking*, vol. 9, no. 9, pp. D31–D41, Sep. 2017. (related to Chapter 3)

[2] **Chen Chen**, Wen-De Zhong, and Dehao Wu, "Non-Hermitian symmetry orthogonal frequency division multiplexing for multiple-input multiple-output visible light communications," *IEEE/OSA Journal of Optical Communications and Networking*, vol. 9, no. 1, pp. 36–44, Jan. 2017. (related to Chapter 3)

[3] **Chen Chen**, Wen-De Zhong, and Dehao Wu, "Integration of OWC with OFDM-PON for hybrid optical access based on adaptive envelope modulation," *Optics Communications*, vol. 381, pp. 10–17, Dec. 2016. (related to Chapter 6)

[4] **Chen Chen**, Wen-De Zhong, Dehao Wu, and Zabih Ghassemlooy, "Wide-FOV and high-gain imaging angle diversity receiver for indoor SDM-VLC systems," *IEEE Photonics Technology Letters*, vol. 28, no. 19, pp. 2078–2081, Oct. 2016. (related to Chapter 4)

[5] **Chen Chen**, Wen-De Zhong, Helin Yang, and Pengfei Du, "ICI mitigation and SINR fluctuation reduction in indoor multi-cell VLC systems using angle diversity multi-element receiver," submitted to *IEEE/OSA Journal of Optical Communications and Networking*, 2017. (related to Chapter 5)

[6] **Chen Chen**, Wen-De Zhong, Sheng Zhang, Pengfei Du, and Helin Yang, "Demonstration of inter-cell interference mitigation in multi-cell VLC systems using angle diversity receiver," submitted to *IEEE Photonics Technology Letters*, 2017. (related to Chapter 5)

[7] **Chen Chen** and Wen-De Zhong, "Hybrid space-frequency domain pre-equalization for DC-biased optical orthogonal frequency division multiplexing based imaging multiple-input multiple-output visible light communication systems," *Optical Engineering*, vol. 56, no. 3, p. 036102, Mar. 2017.

[8] **Chen Chen**, Wen-De Zhong, Xiang Li, and Dehao Wu, “MDPSK-based nonequalization OFDM for coherent free-space optical communication,” *IEEE Photonics Technology Letters,* vol. 26, no. 16, pp. 1617–1620, Aug. 2014.

Conference

[9] **Chen Chen**, Wen-De Zhong, and Dehao Wu, “Communication coverage improvement of indoor SDM-VLC system using NHS-OFDM with a modified imaging receiver,” *2nd Workshop on Optical Wireless Communications (OWC), IEEE International Conference on Communications (ICC),* pp. 315–320, 2016. (related to Chapter 3)

[10] Wen-De Zhong, **Chen Chen**, and Dehao Wu, “Non-Hermitian symmetry OFDM for indoor space division multiplexing visible light communications (invited),” *International Conference on Transparent Optical Networks (ICTON),* paper Mo.C2.3, 2016. (related to Chapter 3)

[11] Wen-De Zhong, **Chen Chen**, Dehao Wu, and Zabih Ghassemlooy, “MIMO visible light communications system using imaging receiver with angle diversity detectors (invited),” *International Conference on Optical Communications and Networks (ICOCN),* pp. 1–3, 2016. (related to Chapter 4)

[12] Wen-De Zhong, **Chen Chen**, and Dehao Wu, “Seamless integration of indoor VLC with WDM-PON based on hierarchically modulated constant envelope OFDM (invited),” *International Conference on Transparent Optical Networks (ICTON),* paper Mo.C2.2, 2015. (related to Chapter 6)

[13] **Chen Chen**, Wen-De Zhong, and Lifan Zhao, “Sparse Bayesian RVM regression based channel estimation for IM/DD OFDM-VLC systems with reduced training overhead,” *3rd Workshop on Optical Wireless Communications (OWC), IEEE International Conference on Communications (ICC),* pp. 369–374, 2017.

[14] **Chen Chen**, Wen-De Zhong, and Dehao Wu, “Indoor OFDM visible light communications employing adaptive digital pre-frequency domain equalization,” *Conference on Lasers and Electro-Optics (CLEO),* paper JTh2A.118, 2016.

[15] **Chen Chen**, Wen-De Zhong, and Dehao Wu, “Color multiplexing based unipolar OFDM for indoor RGB LED visible light communication,” *Procedia Engineering – 4th Photonics Global Conference (PGC)*, vol. 140, pp. 159–165, 2016. (Best Paper Award)

References

[1] L. Hanzo, H. Haas, S. Imre, D. O’Brien, M. Rupp, and L. Gyongyosi, “Wireless myths, realities, futures: From 3G/4G to optical and quantum wireless,” *Proc. IEEE*, vol. 100, pp. 1853–1888, 2012.

[2] P. Pathak, X. Feng, P. Hu, and P. Mohapatra, “Visible light communication, networking, and sensing: a survey, potential and challenges,” *IEEE Commun. Surveys Tuts.*, vol. 17, no. 4, pp. 2047–2077, 2015.

[3] R. D. Dupuis and M. R. Krames, “History, development, and applications of high-brightness visible light-emitting diodes,” *J. Lightw. Technol.*, vol. 26, no. 7, pp. 1154–1171, 2008.

[4] United States Department of Energy. Energy Savings Forecast of Solid-State Lighting in General Illumination Applications. [Online]. Available: http://apps1.eere.energy.gov/buildings/publications/pdfs/ssl/energysavingsforecast14.pdf.

[5] S. Pimputkar, J. Speck, S. P. DenBaars, and S. Nakamura, “Prospects for LED lighting,” *Nat. Photon.*, vol. 3, no. 4, pp. 180–182, 2009.

[6] H. Yang, J. Bergmans, T. Schenk, J. Linnartz, and R. Rietman, “Uniform illumination rendering using an array of LEDs: a signal processing perspective,” *IEEE Trans. Signal Process.*, vol. 57, no. 3, pp. 1044–1057, 2009.

[7] Z. Ghassemlooy, W. Popoola, and S. Rajbhandari, *Optical Wireless Communications, System and Channel Modelling with Matlab*. London, U.K.: CRC Press, 2012.

[8] A. Jovicic, J. Li, and T. Richardson, “Visible light communication: opportunities, challenges and the path to market,” *IEEE Commun. Mag.*, vol. 51, no. 12, pp. 26–32, 2013.

[9] S. Arnon, Ed., *Visible Light Communication*. Cambridge, U.K.: Cambridge Univ. Press, 2015.

[10] H. Haas, “Visible light communication,” in *Opt. Fiber Commun. Conf. (OFC)*, paper Tu2G.5, 2015.

[11] Y. Tanaka, S. Haruyama, and M. Nakagawa, “Wireless optical transmissions with white colored LED for wireless home links,” in *IEEE Int. Symp. PIMRC*, vol. 2, pp. 1325–1329, 2000.

[12] T. Komine and M. Nakagawa, “Fundamental analysis for visible-light communication system using LED lights,” *IEEE Trans. Consum. Electron.*, vol. 50, no. 1, pp. 100–107, 2004.

[13] Visible Light Communications Consortium (VLCC). [Online]. Available: http://www. vlcc. net/

[14] *IEEE Standard for Local and Metropolitan Area Networks-Part 15.7: Short-Range Wireless Optical Communication Using Visible Light*, IEEE Std. 802.15.7, 2011.

[15] [Online]. Available: http://www.ieee802.org/15/pub/TG7.html.

[16] L. Grobe, A. Paraskevopoulos, J. Hilt, D. Schulz, F. Lassak, F. Hartlieb, C. Kottke, V. Jungnickel, and K. D. Langer, “High-speed visible light communication systems,” *IEEE Commun. Mag.*, vol. 51, no. 12, pp. 60-66, 2013.

[17] A. Vavoulas, H. Sandalidis, T. Tsiftsis, and N. Vaiopoulos, “Coverage aspects of indoor VLC networks,” *J. Lightw. Technol.*, vol. 33, no. 23, pp. 4915–4921, 2015.

[18] C. Chen, D. Basnayaka, and H. Haas, “Downlink performance of optical attocell networks,” *J. Lightw. Technol.*, vol. 34, no. 1, pp. 137–156, 2016.

[19] S. Sarkar, S. Dixit, and B. Mukherjee, “Hybrid wireless-optical broadband-access network (WOBAN): a review of relevant challenges,” *J. Lightw. Technol.*, vol. 25, no. 11, pp. 3329–3340, 2007.

[20] F. Effenberger, H. Ichibangase, and H. Yamashita, “Advances in Broadband Passive Optical Networking Technologies,” *IEEE Commun. Mag.*, vol. 39, no. 12, pp. 118–124, 2001.

[21] H. Elgala, R. Mesleh, and H. Haas, “Indoor optical wireless communication: potential and state-of-the-art,” *IEEE Commun. Mag.*, vol. 49, no. 9, pp. 56-62, 2011.

[22] J. McKendry, R. Green, A. Kelly, Z. Gong, B. Guilhabert, D. Massoubre, E. Gu, and M. Dawson, “High-speed visible light communications using individual pixels in a micro light-emitting diode array,” *IEEE Photon. Technol. Lett.*, vol. 22, no. 18, pp. 1346–1348, 2010.

[23] C. Tsai and Z.-Fan Xu, "Line-of-sight visible light communications with InGaN-based resonant cavity LEDs," *IEEE Photon. Technol. Lett.*, vol. 25, no. 18, pp. 1793–1796, 2013.

[24] D. Tsonev, H. Chun, S. Rajbhandari, J. McKendry, S. Videv, E. Gu, M. Haji, S. Watson, A. Kelly, G. Faulkner, M. Dawson, H. Haas, and D. O'Brien, "A 3-Gb/s single-LED OFDM-based wireless VLC link using a Gallium Nitride μLED," *IEEE Photon. Technol. Lett.*, vol. 26, no. 7, pp. 637–640, 2014.

[25] S. Rajbhandari, H. Chun, G. Faulkner, K. Cameron, A. Jalajakumari, R. Henderson, D. Tsonev, M. Ijaz, Z. Chen, H. Haas, E. Xie, J. J. D. McKendry, J. Herrnsdorf, E. Gu, M. D. Dawson, and D. O'Brien, "High-speed integrated visible light communication system: Device constraints and design considerations," *IEEE J. Sel. Areas Commun.*, vol. 33, no. 9, pp. 1750–1757, 2015.

[26] H. Minh, D. O'Brien, G. Faulkner, L. Zeng, K. Lee, D. Jung, and Y. Oh, "High-speed visible light communications using multiple-resonant equalization," *IEEE Photon. Technol. Lett.*, vol. 20, no. 14, pp. 1243–1245, 2008.

[27] H. Minh, D. O'Brien, G. Faulkner, L. Zeng, K. Lee, D. Jung, Y. Oh, and E. Won, "100-Mbit/s NRZ visible light communications using a postequalized white LED," *IEEE Photon. Technol. Lett.*, vol. 21, no. 15, pp. 1063–1065, 2009.

[28] Y. Liu, Y. Chang, C. Chow, and C. Yeh, "Equalization and pre-distorted schemes for increasing data rate in in-door visible light communication system," in *Opt. Fiber Commun. Conf. (OFC)*, paper JWA83, 2011.

[29] X. Huang, J. Shi, J. Li, Y. Wang, Y. Wang, and N. Chi, "750Mbit/s visible light communications employing 64QAM-OFDM based on amplitude equalization circuit," in *Opt. Fiber Commun. Conf. (OFC)*, paper Tu2G.1, 2015.

[30] M. Afgani, H. Haas, H. Elgala, and D. Knipp, "Visible light communication using OFDM," in *Int. Conf. Testbeds Research Infrastructures Development Networks Communities (TRIDENTCOM)*, pp. 129–134, 2006.

[31] Y. Wang, R. Li, Y. Wang, and Z. Zhang, "3.25-Gbps visible light communication system based on single carrier frequency domain equalization utilizing an RGB LED," in *Opt. Fiber Commun. Conf. (OFC)*, paper Th1F.1, 2014.

[32] L. Zeng, D. O'Brien, H. L. Minh, G. E. Faulkner, K. Lee, D. Jung, Y. Oh, and E. Won, "High data rate multiple input multiple output (MIMO) optical wireless communications using white LED lighting," *IEEE J. Sel. Areas Commun.*, vol. 27, no. 9, pp. 1654–1662, 2009.

[33] M. Di Renzo, H. Haas, A. Ghrayeb, S. Sugiura, and L. Hanzo, "Spatial modulation for generalized MIMO: Challenges, opportunities and implementation," *Proc. IEEE*, vol. 102, no. 1, pp. 56–103, 2014.

[34] I. Stefan and H. Haas, "Analysis of optimal placement of LED arrays for visible light communication," in *IEEE Veh. Technol. Conf. (VTC)*, pp. 1–5, 2013.

[35] Z. Wang, C. Yu, W.-D Zhong, J. Chen, and W. Chen, "Performance of a novel LED lamp arrangement to reduce SNR fluctuation for multi-user visible light communication systems," *Opt. Exp.*, vol. 20, no. 4, pp. 4564–4573, 2012.

[36] H. Kim, D. Kim, S. Yang, Y. Son, and S.-K. Han, "Mitigation of inter-cell interference utilizing carrier allocation in visible light communication system," *IEEE Commun. Lett.*, vol. 16, no. 4, pp. 526–529, 2012.

[37] S. Jung, D. Kwon, S. Yang, and S.-K. Han, "Inter-cell interference mitigation in multi-cellular visible light communications," *Opt. Exp.*, vol. 24, no. 8, pp. 8512–8526, 2016.

[38] D. Bykhovsky and S. Arnon, "Multiple access resource allocation in visible light communication systems," *J. Lightw. Technol.*, vol. 32, no. 8, pp. 1594–1600, 2014.

[39] H. Ryoo, D. Kwon, S. Yang, and S.-K Han, "Differential optical detection in VLC for inter-cell interference reduced flexible cell planning," *IEEE Photon. Technol. Lett.*, vol. 28, no. 23, pp. 2728–2731, 2016.

[40] R. Zhang, J. Wang, Z. Wang, Z. Xu, C. Zhao, and L. Hanzo, "Visible light communications in heterogeneous networks: Pave the way for user-centric design," *IEEE Wireless Commun.*, vol. 22, no. 2, pp. 8–16, 2015.

[41] Y. Wang, J. Shi, C. Yang, Y. Wang, and N. Chi, "Integrated 10 Gb/s multilevel multiband passive optical network and 500 Mb/s indoor visible light communication system based on Nyquist single carrier frequency domain equalization modulation," *Opt. Lett.*, vol. 39, no. 9, pp. 2576–2579, 2014.

[42] Y. Wang, J. Yu, and N. Chi, “Symmetric full-duplex integrated passive optical network and optical wireless communication transmission system,” *J. Opt. Commun. Netw.*, vol. 7, no. 7, pp. 628–633, 2015.

[43] Y. Wang, N. Chi, Y. Wang, L. Tao, and J. Shi, “Network architecture of a high-speed visible light communication local area network,” *IEEE Photon. Technol. Lett.*, vol. 27, no. 2 pp. 197–200, 2015.

[44] C. W. Chow, C. H. Yeh, Y. Liu, C. W. Hsu, and J. Y. Sung, “Network architecture of bidirectional visible light communication and passive optical network,” *IEEE Photon. J.*, vol. 8, no. 3, p. 7904506, 2016.

[45] J. Y. Sung, C. W. Chow, C. H. Yeh, and Y. C. Wang, “Service integrated access network using highly spectral-efficient MASK-MQAM-OFDM coding,” *Opt. Exp.*, vol. 21, no. 5, pp. 6555–6560, 2013.

[46] P. Butala, H. Elgala, and T. Little, “Performance of optical spatial modulation and spatial multiplexing with imaging receiver,” in *IEEE Wireless Commun. Netw. Conf. (WCNC)*, pp. 394–399, 2014.

[47] C. Chow, C. Yeh, C. Wang, C. Wu, S. Chi, and C. Lin, “Studies of OFDM signal for broadband optical access networks,” *IEEE J. Sel. Areas Commun.*, vol. 28, no. 6, pp. 800–807, 2010.

[48] S. C. Thompson, A. U. Ahmed, J. G. Proakis, J. R. Zeidler, and M. Geile, “Constant envelope OFDM,” *IEEE Trans. Commun.*, vol. 56, no. 8, pp. 1300–1312, 2008.

[49] F. R. Gfeller and U. Bapst, “Wireless in-house data communication via diffuse infrared radiation,” *Proc. IEEE*, vol. 67, no. 11, pp. 1474-1486, 1979.

[50] Z. Wang, W.-D Zhong, C. Yu, J. Chen, C. Francois, and W. Chen, “Performance of dimming control scheme in visible light communication system,” *Opt. Exp.*, vol. 20, no. 17, pp. 18861–18868, 2012.

[51] I. Neokosmidis, T. Kamalakis, J. Walewski, B. Inan, and T. Sphicopoulos, “Impact of nonlinear LED transfer function on discrete multitone modulation: analytical approach,” *J. Lightwave Technol.*, vol. 27, no. 22, pp. 4970–4978, 2009.

[52] H. Burchardt, N. Serafimovski, D. Tsonev, S. Videv, and H. Haas, “VLC: Beyond point-to-point communication,” *IEEE Commun. Mag.*, vol. 52, no. 7, pp. 98-105, 2014.

[53] S. Rajagopal, R. Roberts, and S.-K. Lim, “IEEE 802.15.7 visible light communication: Modulation schemes and dimming support,” *IEEE Commun. Mag.*, vol. 50, no. 3, pp. 72–82, 2012.

[54] D. Karunatilaka, F. Zafar, V. Kalavally, and R. Parthiban, “LED based indoor visible light communications: State of the art,” *IEEE Commun. Surveys Tuts.*, vol. 17, no. 3, pp. 1649–1678, 2015.

[55] S. Park, D. Jung, H. Shin, D. Shin, Y. Hyun, K. Lee, Y. Oh, “Information broadcasting system based on visible light signboard,” in *Proc. Wireless Opt. Commun.*, pp. 311–313, 2007.

[56] J. Grubor, S. C. J. Lee, K.-D. Langer, T. Koonen, and J. W. Walewski, “Wireless high-speed data transmission with phosphorescent white-light LEDs,” in *Proc. 33rd Eur. Conf. Exhib. Opt. Commun.—Post-Deadline Papers (published 2008)*, pp. 1–2, 2007.

[57] N. Fujimoto and H. Mochizuki, “614 Mbit/s OOK-based transmission by the duobinary technique using a single commercially available visible LED for high-speed visible light communications,” in *Proc. ECEOC*, pp. 1–3, 2012.

[58] IEEE 802.15 WPAN Taskgroup 7 (TG7) Visible Light Communication, 2014. [Online]. Available: http://www.ieee802.org/15/pub/TG7.html

[59] CIE, Commission Internationale de lEclairage Proc. Cambridge, U.K.: Cambridge Univ. Press, 1931.

[60] R. Drost and B. Sadler, “Constellation design for color-shift keying using billiards algorithms,” in *Proc. IEEE GLOBECOM Workshops*, pp. 980–984, 2010.

[61] E. Monteiro and S. Hranilovic, “Constellation design for color-shift keying using interior point methods,” in *Proc. IEEE Globecom Workshops*, pp. 1224–1228, 2012.

[62] E. Monteiro and S. Hranilovic, “Design and implementation of color-shift keying for visible light communications,” *J. Lightw. Technol.*, vol. 32, no. 10, pp. 2053–2060, 2014.

[63] J. Armstrong, “OFDM for optical communications,” *J. Lightw. Technol.*, vol. 27, no. 3, pp. 189–204, 2009.

[64] S. Hashemi, Z. Ghassemlooy, L. Chao, and D. Benhaddou, “Orthogonal frequency division multiplexing for indoor optical wireless communications using visible light LEDs,” in *Proc. CNSDSP*, pp. 174–178, 2008.

[65] J. Vucic, C. Kottke, K. Habel, and K. Langer, “803 Mbit/s visible light WDM link based on DMT modulation of a single RGB LED luminary,” in *Opt. Fiber Commun. Conf. (OFC),* paper OWB6, 2011.

[66] J. Vucic, C. Kottke, S. Nerreter, K. Langer, and J. Walewski, “513 Mbit/s visible light communications link based on DMT-modulation of a white LED,” *J. Lightw. Technol.*, vol. 28, no. 24, pp. 3512–3518, 2010.

[67] A. Khalid, G. Cossu, R. Corsini, P. Choudhury, and E. Ciaramella, “1-Gb/s transmission over a phosphorescent white LED by using rate-adaptive discrete multitone modulation,” *IEEE Photon. J.*, vol. 4, no. 5, pp. 1465–1473, 2012.

[68] J. Sung, C. Yeh, C. Chow, W. Lin, and Y. Liu, “Orthogonal frequency-division multiplexing access (OFDMA) based wireless visible light communication (VLC) system,” *Opt. Commun.*, vol. 355, pp. 261–268, 2015.

[69] H. Zhang, Y. Yuan, and W. Xu, “PAPR reduction for DCO-OFDM visible light communications via semidefinite relaxation,” *IEEE Photon. Technol. Lett.*, vol. 26, no. 17, pp. 1718–1135, 2014.

[70] F. Ogunkoya, W. Popoola, A. Shahrabi, and S. Sinanovic, “Performance evaluation of pilot-assisted PAPR reduction technique in optical OFDM systems,” *IEEE Photon. Technol. Lett.*, vol. 27, no. 10, pp. 1088–1091, 2015.

[71] F. Pancaldi, G. Vitetta, R. Kalbasi, N. Al-Dhahir, M. Uysal, and H. Mheidat, “Single-carrier frequency domain equalization,” *IEEE Signal Process. Mag.*, vol. 25, no. 5, pp. 37–56, 2008.

[72] A. Nuwanpriya, J. A. Zhang, A. Grant, S. Ho, and L. Luo, “Single carrier frequency domain equalization based on on-off-keying for optical wireless communications,” in *Proc. IEEE WCNC,* pp. 3922–3927, 2013.

[73] A. Nuwanpriya, S. Ho, J. Zhang, A. Grant, and L. Luo, “PAM-SCFDE for optical wireless communications,” *J. Lightw. Technol.*, vol. 33, no. 14, pp. 2938–2949, 2015.

[74] Y. Wang, X. Huang, J. Zhang, Y. Wang, and N. Chi, “Enhanced performance of visible light communication employing 512-QAM N-SC-FDE and DD-LMS,” *Opt. Exp.*, vol. 22, no. 13, pp. 15328–15334, 2014.

[75] G. Cossu, A. M. Khalid, P. Choudhury, R. Corsini, and E. Ciaramella, “3.4 Gbit/s visible optical wireless transmission based on RGB LED,” *Opt. Exp.*, vol. 20, no. 26, pp. B501–B506, 2012.

[76] E. Fisher, I. Underwood, and R. Henderson, “A reconfigurable 14-bit 60G photon/s single-photon receiver for visible light communications,” in *Proc. ESSCIRC*, pp. 85–88, 2012.

[77] D. Chitnis, L. Zhang, H. Chun, S. Rajbhandari, G. Faulkner, D. O’Brien, and S. Collins, “A 200 Mb/s VLC demonstration with a SPAD based receiver,” in *IEEE Summer Top. Meet. Ser. (SUM)*, pp. 226–227, 2015.

[78] T. Mao, Z. Wang, and Q. Wang, “Receiver design for SPAD-based VLC systems under Poisson–Gaussian mixed noise model,” *Opt. Exp.*, vol. 25, no. 2, pp. 799–809, 2017.

[79] Y. Li, M. Safari, R. Henderson, and H. Haas, “Optical OFDM with single-photon avalanche diode,” *IEEE Photon. Technol. Lett.*, vol. 27, no. 9, pp. 943–946, 2015.

[80] L. Fraas and L. Partain, *Solar Cells and Their Applications*, 2nd ed., Wiley, New Jersey, 2010.

[81] S. Kim, J. Won, and S. Nahm, “Simultaneous reception of solar power and visible light communication using a solar cell,” *Opt. Eng.*, vol. 53, no.4, p. 046103, 2014.

[82] Z. Wang, D. Tsonev, S. Videv, and H. Haas, “On the design of a solar-panel receiver for optical wireless communications with simultaneous energy harvesting,” *IEEE J. Sel. Areas Commun.*, vol. 33, no. 8, pp. 1612–1623, 2015.

[83] W. Shin, S. Yang, D. Kwon, and S. Han, “Self-reverse-biased solar panel optical receiver for simultaneous visible light communication and energy harvesting,” *Opt. Exp.*, vol. 24, no. 22, pp. A1300-A1305, 2016.

[84] E. Ghahremanirad, S. Olyaee, and A. Chizari, “Nano-plasmonic thin-film solar cell receiver in visible light communication,” in *Proc. CNSDSP*, pp. 1–5, 2016.

[85] T. Yamazato and S. Haruyama, “Image sensor based visible light communication and its application to pose, position, and range estimations,” *IEICE Trans. on Commun.*, vol. E97-B, no. 9, pp. 1759–1765, 2014.

[86] T. Yamazato, I. Takai, H. Okada, T. Fujii, T. Yendo, S. Arai, M. Andoh, T. Harada, K. Yasutomi, K. Kagawa, and S. Kawahito, “Image-sensor-based visible light

communication for automotive applications," *IEEE Commun. Mag.*, vol. 52, no. 7, pp. 88–97, 2014.

[87] I. Takai, S. Ito, K. Yasutomi, K. Kagawa, M. Andoh, and S. Kawahito, "LED and CMOS image sensor based optical wireless communication system for automotive applications," *IEEE Photon. J.*, vol. 5, no. 5, Art. ID. 6801418, 2013.

[88] T. Yamazato, M. Kinoshita, S. Arai, E. Souke, T. Yendo, T. Fujii, K. Kamakura, and H. Okada, "Vehicle motion and pixel illumination modeling for image sensor based visible light communication," *IEEE J. Sel. Areas Commun.*, vol. 33, no. 9, pp. 1793–1805, 2015.

[89] N. Saha, M. Ifthekhar, N. Le, and Y. Jang, "Survey on optical camera communications: challenges and opportunities," *IET Optoelectron.*, vol. 9, no. 5, pp. 172–183, 2015.

[90] C. Danakis, M. Afgani, G. Povey, I. Underwood, and H. Haas, "Using a CMOS camera sensor for visible light communication," in *Proc. IEEE Globecom Workshops*, pp. 1244–1248, 2012.

[91] P. Luo, Z. Ghassemlooy, H. Le Minh, X. Tang, and H.-S. Tsai, "Undersampled phase shift ON-OFF keying for camera communication," in *Proc. Int. Conf. Wireless Commun. Signal Process. (WCSP)*, pp. 1–6, 2014.

[92] T. Fath and H. Haas, "Performance comparison of MIMO techniques for optical wireless communication in indoor environments," *IEEE Trans. Commun.*, vol. 61, no. 2, pp. 733–742, 2013.

[93] S. Navidpour, M. Uysal, and M. Kavehrad, "BER performance of free-space optical transmission with spatial diversity," *IEEE Trans. Wireless Commun.*, vol. 23, no. 9, pp. 1901–1910, 2005.

[94] A. Burton, H. Minh, Z. Ghassemlooy, E. Bentley and C. Botella, "Experimental demonstration of 50-Mb/s visible light communications using 4×4 MIMO," *IEEE Photon. Technol. Lett.*, vol. 26, no. 9, pp. 945–948, 2014.

[95] P. Butala, H. Elgala, and T. D. C. Little, "SVD-VLC: A novel capacity maximizing VLC MIMO system architecture under illumination constraints," in *Proc. IEEE Globecom Workshop OWC*, pp. 1087–1092, 2013.

[96] H. Yang, and L. Chen, "On the performance of adaptive MIMO-OFDM indoor visible light communications," *IEEE Photon. Technol. Lett.*, vol. 28, no. 8, pp. 907–910, 2015.

[97] K. Ying, H. Qian, R. Baxley, and S. Yao, “Joint optimization of precoder and equalizer in MIMO VLC systems,” *IEEE J. Sel. Area Commun.*, vol. 33, no. 9, pp. 1949–1958, 2015.

[98] K. Park, H. Oubei, W. Alheadary, B. Ooi, and M. Alouini, “Design and experimental demonstration of mirror-aided non-imaging receiver for indoor MIMO-VLC systems,” in *Proc. Workshop on Hot Topics in Wireless*, pp. 66-70, 2016.

[99] L. Wei, H. Zhang, and J. Song, “Experimental demonstration of a cubic receiver based MIMO visible light communication system,” *IEEE Photon. J.*, vol. 9, no. 1, Art. ID. 7900107, 2017.

[100] Y. Chau and S.-H. Yu, “Space modulation on wireless fading channels,” in *Proc. IEEE VTC*, vol. 3, pp. 1668–1671, 2001.

[101] R. Mesleh, H. Haas, S. Sinanovic, C. Ahn, and S. Yun, “Spatial modulation,” *IEEE Trans. Veh. Technol.*, vol. 57, no. 4, pp. 2228–2241, 2008.

[102] R. Mesleh, H. Haas, C. W. Ahn, and S. Yun, “Spatial modulation–a new low complexity spectral efficiency enhancing technique,” in *Proc. IEEE Int. Conf. Commun. Netw.*, pp. 1–5, 2006.

[103] Y. Wang and N. Chi, “Demonstration of high-speed 2 × 2 non-imaging MIMO Nyquist single carrier visible light communication with frequency domain equalization,” *J. Lightw. Technol.*, vol. 32, no. 11, pp. 2087–2093, 2014.

[104] A. Burton, Z. Ghassemlooy, S. Rajbhandari, and S.-K. Liaw, “Design and analysis of an angular-segmented full-mobility visible light communications receiver,” *Trans. on Emerging Telecommun. Tech.*, vol. 25, no. 6, pp. 591–599, 2014.

[105] P. Fahamuel, J. Thompson and H. Haas, “Improved indoor VLC MIMO channel capacity using mobile receiver with angular diversity detectors,” in *Proc. IEEE Global Commun. Conf. (GLOBECOM)*, pp. 2060–2065, 2014.

[106] A. Nuwanpriya, S.-W. Ho, and C. S. Chen, “Indoor MIMO visible light communications: novel angle diversity receivers for mobile users,” *IEEE J. Sel. Areas Commun.*, vol. 33, no. 9, pp. 1780–1792, 2015.

[107] A. H. Azhar, T.-A. Tran, and D. O'Brien, "A gigabit/s indoor wireless transmission using MIMO-OFDM visible-light communications," *IEEE Photon. Technol. Lett.*, vol. 25, no. 2, pp. 171–174, 2013.

[108] Y. Wang and N. Chi, "Indoor gigabit 2 × 2 imaging multiple-input-multiple-output visible light communication," *Chin. Opt. Lett.*, vol. 12, no. 10, Art. no. 100603, 2014

[109] T. Chen, Z. Zheng, L. Liu, and W. Hu, "High-diversity space division multiplexing visible light communication utilizing a fisheye-lens-based imaging receiver," in *Opt. Fiber Commun. Conf. (OFC)*, paper Tu2G.3, 2015

[110] T. Baumgartner, F. Wunderlich, A. Jaunich, T. Sato, and G. Bundy, "Lighting the way: Perspectives on the global lighting market," McKinsey Co., Nashua, NH, USA, Tech. Rep., 2012.

[111] M. Wada, T. Yendo, T. Fujii, and M. Tanimoto, "Road-to-vehicle communication using LED traffic light," in *Proc. IEEE IV Symp.*, pp. 601–606, 2005.

[112] K. Cui, G. Chen, Z. Xu and R. Roberts, "Experimental characterization of traffic light to vehicle VLC link performance," in *Proc. IEEE Workshop OWC*, pp.808–812, 2011.

[113] Y. Kim, and Y. Chung, "Experimental demonstration of highway I2V using visible light communications," *Appl. Opt.*, vol. 55, no. 22, pp. 5840–5845, 2016.

[114] P. Luo, Z. Ghassemlooy, H. Minh, E. Bentley, A. Burton, and X. Tang, "Performance analysis of a car-to-car visible light communication system," *Appl. Opt.*, vol. 54, no. 7, pp. 1696–1706, 2015.

[115] Y. Kim, W. Cahyadi, and Y. Chung, "Experimental demonstration of VLC-based vehicle-to-vehicle communications under fog conditions," *IEEE Photon. J.*, vol. 7, no. 6, Art. ID. 7905309, 2015.

[116] S. Arnon, "Underwater optical wireless communication network," *Opt. Eng.*, vol. 49, no. 1, Art ID. 015001, 2010.

[117] H. Uema, T. Matsumura, S. Saito, and Y. Murata, "Research and development on underwater visible light communication systems," *Electron. Commun. Japan*, vol. 98, no. 3, pp. 9–13, 2015.

[118] J. Giles and I. Bankman, "Underwater optical communications systems—Part 2: Basic design considerations," in *Proc. IEEE MILCOM Conf.*, pp. 1700–1705, 2005.

[119] F. Schill, U. R. Zimmer, and J. Trumpf, “Visible spectrum optical communication and distance sensing for underwater applications,” in *Proc. ACRA*, pp. 1–8, 2004.

[120] I. Rust and H. Asada, “A dual-use visible light approach to integrated communication and localization of underwater robots with application to non-destructive nuclear reactor inspection,” in *Proc. IEEE ICRA*, pp. 2445–2450, 2012.

[121] C. Quintana, V. Guerra, J. Rufo, J. Rabadan, and R. Perez-Jimenez, “Reading lamp-based visible light communication system for in-flight entertainment,” *IEEE Trans. Consum. Electron.*, vol. 59, no. 1, pp. 31–37, Feb. 2013.

[122] J. Armstrong, Y. Sekercioglu, and A. Neild, “Visible light positioning: A roadmap for international standardization,” *IEEE Commun. Mag.*, vol. 51, no. 12, pp. 68–73, Dec. 2013.

[123] Z. Zhou, M. Kavehrad, and P. Deng, “Indoor positioning algorithm using light-emitting diode visible light communications,” *Opt. Eng.*, vol. 51, no. 8, Art. ID. 085009, Aug. 2012.

[124] H. Kim, D. Kim, S. Yang, Y. Son, and S. Han, “An indoor visible light communication positioning system using a RF carrier allocation technique,” *J. Lightw. Technol.*, vol. 31, no. 1, pp. 134–144, Jan. 2013.

[125] P. Connolly and D. Bonte, “Indoor Location in Retail: Where Is the Money?” ABI Research Report, Mar. 2013. http://www.abiresearch.com/research/product/1013925-indoor-location-in-retail-where-is-the-mon/.

[126] T. Yamazato, A. Ohmura, H. Okada, T. Fujii, T. Yendo, S. Arai, and K. Kamakura, “Range estimation scheme for integrated I2V-VLC using a high-speed image sensor,” in *Proc. IEEE Int. Conf. Commun. (ICC) Workshops*, pp. 326–3302016, May 2016.

[127] D. Wu, W.-D. Zhong, Z. Ghassemlooy, and C. Chen, “Short-range visible light ranging and detecting system using illumination light emitting diodes,” *IET Optoelectron.*, vol. 10, no. 3, pp. 94–99, Jun. 2016.

[128] W. Cahyadi, Y. Kim, Y. Chung, and Z. Ghassemlooy, “Efficient road surface detection using visible light communication,” in *Proc. ICUFN*, pp. 61-63, Jul. 2015.

[129] A. Sewaiwar, S. Tiwari, and Y. Chung, “Visible light communication based motion detection,” *Opt. Exp.*, vol. 23, no. 14, pp. 18769–18776, Jul. 2015.

[130] T. Li, C. An, Z. Tian, A. T. Campbell, and X. Zhou, “Human sensing using visible light communication,” in *Proc. Int. Conf. MobiCom*, pp. 331–344, 2015.

[131] Y. Yang J. Hao, J. Luo, S. Pan, “CeilingSee: device-free occupancy inference through lighting infrastructure based LED sensing,” to be published, 2017.

[132] J. Armstrong and B. J. C. Schmidt, “Comparison of asymmetrically clipped optical OFDM and DC-biased optical OFDM in AWGN,” *IEEE Commun. Lett.*, vol. 12, pp. 343–345, May 2008.

[133] S. Dissanayake and J. Armstrong, “Comparison of ACO-OFDM, DCO-OFDM, and ADO-OFDM in IM/DD systems,” *J. Lightw. Technol.*, vol. 31, no. 7, pp. 1063–1072, 2013.

[134] D. Tsonev, S. Sinanovic, and H. Haas, “Novel unipolar orthogonal frequency division multiplexing (U-OFDM) for optical wireless,” in *IEEE Veh. Technol. Conf. (VTC)*, pp. 1–5, 2012.

[135] D. Tsonev and H. Haas, “Avoiding spectral efficiency loss in unipolar OFDM for optical wireless communication,” in *IEEE Int. Conf. Commun. (ICC)*, pp. 3336–3341, 2014.

[136] H. Elgala and T. D. C. Little, “SEE-OFDM: Spectral and energy efficient OFDM for optical IM/DD systems,” in *IEEE Int. Symp. Pers. Indoor Mobile Radio Commun. (PIMRC)*, pp. 486–490, 2013.

[137] N. Wu and Y. Bar-Ness, “A novel power-efficient scheme asymmetrically and symmetrically clipping optical (ASCO)-OFDM for IM/DD optical systems,” *EURASIP J. Advances Sig. Proc.*, vol. 3, 2015.

[138] M. Moreolo, R. Muñoz, and G. Junyent, “Novel power efficient optical OFDM based on Hartley transform for intensity-modulated direct-detection systems,” *J. Lightw. Technol.*, vol. 28, no. 5, pp. 798–805, 2010.

[139] H. Elgala and T. Little, “P-OFDM: Spectrally efficient unipolar OFDM,” in *Opt. Fiber Commun. Conf. (OFC)*, paper Th3G.7, 2014.

[140] F. Barrami, Y. Guennec, E. Novakov, J.-M. Duchamp, and P. Busson, “A novel FFT/IFFT size efficient technique to generate real time optical OFDM signals compatible with IM/DD systems,” in *Eur. Microw. Conf. (EuMC)*, pp. 1247–1250, 2013.

[141] A. Nuwanpriya, A. Grant, S. Ho, and L. Luo, “Position modulating OFDM for optical wireless communications,” in *IEEE Global Commun. Conf. (GLOBECOM)*, pp. 1219–1223, 2012.

[142] C. Chen, W.-D. Zhong, and D. Wu, “Non-Hermitian symmetry orthogonal frequency division multiplexing for multiple-input multiple-output visible light communications,” *IEEE/OSA J. Opt. Commun. Netw.*, vol. 9, no. 1, pp. 36–44, 2017.

[143] W.-D. Zhong, C. Chen, and D. Wu, “Non-Hermitian symmetry OFDM for indoor space division multiplexing visible light communications (Invited Paper),” in *Int. Conf. Transparent Opt. Netw. (ICTON),* paper Mo.C2.3, 2016.

[144] C. Chen, W.-D. Zhong, and D. Wu, “Communication coverage improvement of indoor SDM-VLC system using NHS-OFDM with a modified imaging receiver”, in *IEEE Int. Conf. Commun. (ICC) Workshops*, pp. 315–320, 2016.

[145] C. Chen, W.-D. Zhong, and D. Wu, “On the coverage of multiple-input multiple-output visible light communications [invited],” *J. Opt. Commun. Netw.*, vol. 9, no. 9, pp. D31–D41, 2017.

[146] Z. Wang, C. Yu, W.-D. Zhong, and J. Chen, “Performance improvement by tilting receiver plane in M-QAM OFDM visible light communications,” *Opt. Exp.*, vol. 19, no. 14, pp. 13418–13427, 2011.

[147] K. Cho and D. Yoon, “On the general BER expression of one- and two-dimensional amplitude modulations,” *IEEE Trans. Commun.*, vol. 50, no. 7, pp. 1074–1080, 2002.

[148] H. Sorensen, D. Jones, M. Heideman, and C. Burrus, “Real-valued fast Fourier transform algorithms”, *IEEE Trans. Acoust., Speech, Signal Process.*, vol. 35, no. 6, pp. 849–863, 1987.

[149] H. Chi and Z. Lai, “A cost-effective memory-based real-valued FFT and Hermitian symmetric IFFT processor for DMT- based wire-line transmission systems,” in *IEEE Int. Symp. Circuits and Systems (ISCAS),* pp. 6006–6009, 2005.

[150] X. Li, W.-D. Zhong, A. Alphones, C. Yu, and Q. Yang, “Channel equalization based on QR decomposition in indoor visible light communication,” in *IEEE Conf. Industrial Electron. Applicat. (ICIEA),* pp. 1491–1495, 2015.

[151] J. Li, Z. Huang, X. Liu, and Y. Ji, "Hybrid time-frequency domain equalization for LED nonlinearity mitigation in OFDM-based VLC systems," *Opt. Exp.*, vol. 23, no. 1, pp. 611–619, 2015.

[152] N. Ishikawa and S. Sugiura, "Maximizing constrained capacity of power-imbalanced optical wireless MIMO communications using spatial modulation," *J. Lightw. Technol.*, vol. 33, no. 2, pp. 519–527, 2015.

[153] T. Q. Wang, R. J. Green, and J. Armstrong, "MIMO optical wireless communications using ACO-OFDM and a prism-array receiver," *IEEE J. Sel. Areas Commun.*, vol. 33, no. 9, pp. 1959–1971, 2015.

[154] S. Sugiura and H. Iizuka, "Element-by-element full-rank optical wireless MIMO systems using narrow-window angular filter designed based on one-dimensional photonic crystal," *J. Lightw. Technol.*, vol. 34, no. 24, pp. 5601–5609, 2016.

[155] T. Wang, Y. Sekercioglu, and J. Armstrong, "Hemispherical lens based imaging receiver for MIMO optical wireless communications," in *IEEE Global Commun. Conf. (GLOBECOM) Workshops*, pp. 1239–1243, 2012.

[156] T. Wang, Y. Sekercioglu, and J. Armstrong, "Analysis of an optical wireless receiver using a hemispherical lens with application in MIMO visible light communications," *J. Lightw. Technol.*, vol. 31, no. 11, pp. 1744–1754, 2013.

[157] C. Chen, W.-D. Zhong, D. Wu, and Z. Ghassemlooy, "Wide-FOV and high-gain imaging angle diversity receiver for indoor SDM-VLC systems," *IEEE Photon. Technol. Lett.*, vol. 28, no. 19, pp. 2078–2081, 2016.

[158] C. Chen and W.-D. Zhong, "Performance comparison of different types of receivers in indoor MIMO-VLC systems," in *Int. Conf. Computer Netw. Commun. Technol. (CNCT)*, pp. 341–346, 2016.

[159] P. Djahani and J. Kahn, "Analysis of infrared wireless links employing multibeam transmitters and imaging diversity receivers," *IEEE Trans. Commun.*, vol. 48, no. 12, pp. 2077–2088, 2000.

[160] C. Chen, W.-D. Zhong, S. Zhang, P. Du, and H. Yang, "Demonstration of inter-cell interference mitigation in multi-cell VLC systems using angle diversity receiver," submitted to *IEEE Photon. Technol. Lett.*, 2017.

[161] C. Chen, W.-D. Zhong, H. Yang, and P. Du, "Angle diversity multi-element receiver for ICI mitigation and SINR fluctuation reduction in indoor multi-cell VLC systems," submitted to *J. Opt. Commun. Netw.*, 2017.

[162] Z. Chen, D. Tsonev, and H. Haas, "Improving SINR in indoor cellular visible light communication networks," in *Proc. IEEE Int. Conf. Commun. (ICC)*, pp. 3383–3388, 2014.

[163] C. Chen, W.-D. Zhong, and D. Wu, "Indoor OFDM visible light communications employing adaptive digital pre-frequency domain equalization," in *Conf. on Lasers and Electro-Optics (CLEO)*, paper JTh2A.118, 2016.

[164] P. Mmbaga, J. Thompson, and H. Haas, "Performance analysis of indoor diffuse VLC MIMO channels using angular diversity detectors," *J. Lightw. Technol.*, vol. 34, no. 4, pp. 1254–1266, 2016.

[165] C. Edwards and D. Penney, Calculus. New Jersey: Prentice Hall, 2002.

[166] European Standard EN 12464-1, "Lighting of Indoor Work Places," Jan. 2009.

[167] L. Kazovsky, S.-W. Wong, T. Ayhan, K. Albeyoglu, M. Ribeiro, and A. Shastri, "Hybrid optical-wireless access networks," *Proc. IEEE*, vol. 100, no. 5, pp. 1197–1225, 2012.

[168] Y.-L. Hsueh, M. Rogge, S. Yamamoto, and L. Kazovsky, "A highly flexible and efficient passive optical network employing dynamic wavelength allocation," *J. Lightwave Technol.*, vol. 23, no. 1, pp. 277–286, 2005.

[169] C. Chen, C. Zhang, W. Zhang, W. Jin, and K. Qiu, "Scalable and reconfigurable generation of flat optical comb for WDM-based next-generation broadband optical access networks," *Opt. Commun.*, vol. 321, pp. 16–22, 2014.

[170] L. Zhang, X. Xin, B. Liu, and Y. Wang, "Secure OFDM-PON based on chaos scrambling," *IEEE Photon. Technol. Lett.*, vol. 23, no. 14, pp. 998-1000, 2011.

[171] C. Chen, C. Zhang, D. Liu, K. Qiu, and S. Liu, "Tunable optical frequency comb enabled scalable and cost-effective multiuser orthogonal frequency-division multiple access passive optical network with source-free optical network units," *Opt. Lett.*, vol. 37, no. 19, pp. 3954–3956, 2012.

[172] N. Ghazisaidi, M. Maier, and C. M. Assi, “Fiber-wireless (FiWi) access networks: a survey,” *IEEE Commun. Mag.*, vol. 47, no. 2, pp. 160–167, 2009.

[173] K. Yang, S. Ou, K. Guild, and H.-H. Chen, “Convergence of Ethernet PON and IEEE 802.16 broadband access networks and its QoS-aware dynamic bandwidth allocation scheme,” *IEEE J. Sel. Areas Commun.*, vol. 27, no. 2, pp. 101–116, 2009.

[174] G.-K. Chang, A. Chowdhury, Z. Jia, H.-C. Chien, M.-F. Huang, J. Yu, and G. Ellinas, “Key technologies of WDM-PON for future converged optical broadband access networks [Invited],” *J. Opt. Commun. Netw.*, vol. 1, no. 4, pp. C35–C50, 2009.

[175] C. Chen, C. Zhang, W. Zhang, W. Jin, and K. Qiu, “Hybrid WDM-OFDMA-PON utilising tunable generation of flat optical comb,” *Electron. Lett.*, vol. 49, no. 4, pp. 276–277, 2013.

[176] Y. Xiang, C. Chen, C. Zhang, and K. Qiu, “Wired/wireless access integrated RoF-PON with scalable generation of multi-frequency MMWs enabled by polarization multiplexed FWM in SOA,” *Opt. Exp.*, vol. 21, no. 1, pp. 1218–1225, 2013.

[177] R. B. Nunes, H. R. de O. Rocha, D. A. A. Mello, F. D. Simoes, M. E. V. Segatto, and J. A. L. Silva, “Transmission of CE-OFDM signals over MMF links using directly modulated 850-nm VCSELs,” *IEEE Photon. Technol. Lett.*, vol. 27, no. 3, pp. 315–318, 2015.

[178] S. C. Thompson, “Constant envelope OFDM phase modulation,” Ph.D. dissertation, University of California, San Diego, 2005.

[179] C. Chen, W.-D. Zhong, and D. Wu, “Integration of OWC with OFDM-PON for hybrid optical access based on adaptive envelope modulation,” *Opt. Commun.*, vol. 381, pp. 10–17, 2016.

[180] W.-D. Zhong, C. Chen, and D. Wu, “Seamless integration of indoor VLC with WDM-PON based on hierarchically modulated constant envelope OFDM,” in *Int. Conf. Transparent Opt. Netw. (ICTON)*, paper Mo.C2.2, 2015.

[181] A. Goldsmith, *Wireless Communications*. Cambridge, U.K.: Cambridge Univ. Press, 2005.

[182] I. Djordjevic and G. T. Djordjevic, “On the communication over strong atmospheric turbulence channels by adaptive modulation and coding,” *Opt. Exp.*, vol. 17, no. 20, pp. 18250–18262, 2009.